UNIVERSITÄT PADERBORN

Die Universität der Informationsgesellschaft

Microscopic analysis of the nonlinear optical response of semiconductors: Carrier dynamics in extremely intense Terahertz fields and many-body correlations in type-II heterostructures

Dissertation

zur
Erlangung des Doktorgrades
der Naturwissenschaften
(Dr. rer. nat.)

der

Fakultät für Naturwissenschaften
der Universität Paderborn
vorgelegt von

ALEXANDER TRAUTMANN

Paderborn, 2023

Erklärung der Selbstständigkeit

Hiermit versichere ich, die vorliegende Arbeit selbstständig verfasst und keine anderen als die angegebenen Quellen und Hilfsmittel benutzt sowie die Zitate deutlich kenntlich gemacht zu haben.

_____
Ort, Datum

_____
Unterschrift

Vorsitzender der Prüfungskommission: Prof. Dr. Thomas Zentgraf

Erstgutachter: Prof. Dr. Torsten Meier

Zweitgutachter: Prof. Dr. Stefan Schumacher

Mitglied der Promotionskomission: Dr. Falco Meier

Zusammenfassung

In dieser Arbeit wird die nichtlineare Wechselwirkung von Licht und Materie in Halbleitern und Halbleiter-Nanostrukturen anhand der Halbleiter-Bloch Gleichungen beschrieben. Im Rahmen eines Zwei-Band-Modells wird gezeigt, dass Intrabandströme beim Vier-Wellen-Mischen mit nicht-resonanten Lichtpulsen maßgeblich zum nichtlinearen Signal beitragen. Diese Ströme werden durch eine feld-induzierte Beschleunigung von Elektronen und Löchern in den jeweiligen Bändern erzeugt. Am Beispiel von MgO wird die Bewegung der Ladungsträger und deren Einfluss auf die Erzeugung hoher Harmonischen untersucht. Die Kollisionsdynamik im Material beeinflusst den Rekombinationsprozess zwischen Elektronen und Löchern und ist für die Anisotropie, d.h. die Abhängigkeit der Erzeugung hoher Harmonischer von der Polarisationsrichtung verantwortlich. Des Weiteren wird der Einfluss von exzitonischen Effekten auf die Erzeugung hoher Harmonischer demonstriert. Sofern ein ungerades Vielfaches der Pulsfrequenz mit der Energie des 1s-Exzitons übereinstimmt, tritt eine verstärkte Erzeugung von hohen Harmonischen auf. Zum Abschluss wird der Einfluss von Vielteilchen Coulomb-Korrelationen bei optischen Anregungen in der Nähe der Bandlücke in räumlich-direkten Typ-I und indirekten Typ-II Halbleiter-Nanostrukturen untersucht. Die räumliche Inhomogenität in Typ-II Systemen äußert sich insbesondere in einer unterschiedlich starken Coulomb-Wechselwirkung. Dies führt in der zeitabhängigen Hartree-Fock Näherung zu zusätzlichen Beiträgen zur optischen Antwort. Unsere Ergebnisse unter Berücksichtigung von biexzitonischen Vielteilchen-Korrelationen ermöglichen eine physikalische Interpretation der Messdaten von Anrege-Abfrage Experimenten, in denen Typ-II Halbleiter-Nanostrukturen untersucht wurden.

Summary

In this work we describe the nonlinear interaction between light and matter in semiconductors and semiconductor nanostructures using the semiconductor Bloch equations. Within a two-band model it is shown that intraband currents contribute significantly to the nonlinear four-wave-mixing signal excited by nonresonant light pulses. These currents are generated by the field-induced acceleration of electrons and holes in their respective bands. The motion of charge carriers and their influence on the generation of higher harmonics in solids is investigated for the case of MgO. The collision dynamics in the material influences the recombination process between electrons and holes and is responsible for the anisotropy, i.e., the polarization-direction dependence of high harmonic generation in solids. Additionally, the influence of excitonic effects on the generation of higher harmonics is analyzed. When an odd multiple of the pulse frequency coincides with the energy of the 1s exciton, an enhanced generation of higher harmonics is obtained. Finally, the influence of many-body Coulomb correlations for optical excitations near the band gap is investigated in spatially-direct type-I and spatially-indirect type-II semiconductor nanostructures. The spatial inhomogeneity of type-II systems manifests itself, in particular, in a modified strength of the Coulomb interaction. This leads to additional contributions to the optical response in the time-dependent Hartree-Fock approximation. Our findings which include biexcitonic many-body correlations allow a physical interpretation of measured data from pump-probe experiments performed on type-II semiconductor quantum wells.

List of Scientific Contributions

Doctorate-Related Publications and Presentations

Peer-Reviewed Publications

- W.-R. Hannes, **A. Trautmann**, M. Stein, F. Schäfer, M. Koch, and T. Meier, Strongly nonresonant four-wave mixing in semiconductors, Phys. Rev. B **101**, 075203 (2020).

- R. Zuo, **A. Trautmann**, G. Wang, W.-R. Hannes, S. Yang, X. Song, T. Meier, M. Ciappina, H.T. Duc, and W. Yang, Mapping band structures with neighboring-atom-collisions in solid high harmonic generation. Ultrafast Science **2021**, 9861923 (2021).

Conference Proceedings

- **A. Trautmann**, R. Zuo, G. Wang, W.-R. Hannes, S. Yang, L.H. Thong, C. Ngo, J.T. Steiner, M. Ciappina, M. Reichelt, H.T. Duc, X. Song, W. Yang, and T. Meier, Microscopic simulations of high harmonic generation from semiconductors, Proc. SPIE **11999**, 1199909 (2022).

- **A. Trautmann**, M. Stein, F. Schäfer, D. Anders, C. Ngo, J.T. Steiner, S. Chatterjee, and T. Meier, Analysis of the nonlinear optical response of excitons in type-I and type-II quantum wells inluding many-body correlations, Proc. SPIE **12419**, 124190A (2023).

- M. Stein, F. Schäfer, D. Anders, J. Littman, M. Fey, **A. Trautmann**, C. Ngo, J.T. Steiner, M. Reichelt, C. Fuchs, K. Volz, T. Meier, and S. Chatterjee, Experimental studies of the excitonic nonlinear response of GaAs-based type-I and type-II quantum well structures interacting with optical and terahertz fields, Proc. SPIE **12419**, 1241909 (2023).

Work in Progress

- F. Schäfer, **A. Trautmann**, C. Ngo, J.T. Steiner, M. Stein, C. Fuchs, K. Volz, F. Dobener, T. Meier, and S. Chatterjee, Optical Stark effect in type-II heterostructures, in preparation.

- H. Zhang, R. Zuo, S. Yang, **A. Trautmann**, X. Song, T. Meier, and W. Yang, Analyzing high harmonic generation in solids based on semi-classical recollision models, under consideration as a chapter in the book "High-order Harmonic Generation in Solids" (World Scientific), edited by Marcelo Ciappina.

Non-Doctorate-Related Publications

- J. Vondran, F. Spitzer, M. Bayer, I.A. Akimov, **A. Trautmann**, M. Reichelt, C. Meier, N. Weber, T. Meier, R. Andre, and H. Mariette, Spatially asymmetric transients of propagating exciton-polariton modes in a planar CdZnTe/CdMgTe guiding structure, Phys. Rev. B **100**, 155308 (2019).

My contributions

The numerical solutions of the two-band semiconductor Bloch equations shown in chapter 3 were performed by Dr. Wolf-Rüdiger Hannes. Here, I provided additional simulations that supported the physical interpretation, i.e., numerical solutions of the Maxwell-Bloch equations with the finite-difference time domain method (see Fig. 3.1.). In chapter 4 I present theoretical findings from a collaboration with the group of Prof. Dr. Xiaohong Song (Hainan University). Here, I participated in the acquisition and analysis of the full quantum results, i.e., I provided the solutions of the semiconductor Bloch equations and discussed and approved the results concerning the semiclassical trajectory analysis.

All theoretical results on the influence of the many-body Coulomb interaction on the nonlinear optical response, i.e., chapters 5 and 6 have been obtained by myself. The experiments were performed in the group of Prof. Dr. Sangam Chatterjee (University of Giessen). Presently, we prepare a joint experiment-theory manuscript where I provide the theoretical results and contribute to the text.

Contents

Introduction

1

In the past decades, advancements in the understanding of the electronic properties of semiconductors have enabled the production of increasingly powerful semiconductor chips. Today, the focus remains on the development of downsizing electronic devices, driving current research towards developing microscopic models for the study of these materials and systems [1]. Semiconductors exhibit a remarkable sensitivity to the addition of carriers. These carriers can be introduced into the semiconductor crystal through various methods, such as doping, electronic injection, or optical excitation. The electronic properties of semiconductors primarily arise from excitation within a single energy band, known as intraband acceleration. These excitations describe the motion of carriers in real space, i.e. their transport characteristics [2]. The quantum mechanical description of electrons in a periodic lattice under the influence of an electric field was already introduced by Bloch and Zener in 1929 and 1934, respectively [3, 4]. In contrast, the optical properties of semiconductors are associated with transitions between the valence bands and the conduction bands, which are known as interband transitions. These transitions occur when an electron is excited from the valence band, which represents the energy levels that in the ground state are occupied by electrons, to the conduction band. Interband transitions are responsible for phenomena such as absorption, emission, and scattering of light in semiconductors [2]. Although a clear distinction is often made between intraband and interband transitions due to their distinct roles, it is important to note that a strict separation between these two types of transitions is not always possible. The electronic and optical properties of semiconductors arise from a complex interplay between these transitions, making the study and understanding of their behavior a fascinating and multifaceted field of research.

In 1961, with the development of intense lasers, Franken et al. were able to measure the emission of a second harmonic which represents a nonlinear optical process [5, 6]. The use of laser pulses has enabled the study of ultrafast processes, occurring within the pico- (10^{-12} s) and femtosecond (10^{-15} s) range [7, 8]. To investigate the electron dynamics in solids, ultrafast spectroscopy has become a powerful method, utilizing, e.g., pump-probe (PP) experiments or four-wave-mixing (FWM) spectroscopy [9–12]. Both setups are still popular methods to study the ultrafast quantum mechanical processes in photoexcited semiconductors including both intraband and interband transitions [13–30]. In FWM spectroscopy the so-called self-diffraction geometry is a widely used approach. Here, two pulses which are delayed temporally excite the sample and lead to a nonlinear signal of at least third order. This nonlinear signal is emitted into a background-free direction [31]. It is possible to study dephasing times in semiconductor nanostructures even if they are inhomogeneously broadened [14, 21, 22, 24, 32]. In PP measurements an optical pump pulse firstly excites or perturbs the system, while a temporally delayed probe pulse measures the

resulting changes in the material. Thereby, the dynamics of charge carriers, i.e., electron and occupations, in semiconductors can be investigated [33]. For instance, by varying the time delay between the pump and probe pulse, it is possible to study relaxation dynamics (population lifetime of excited states) [8]. Overall, these ultrafast spectroscopy techniques are able to reveal the dynamical processes in semiconductors with a very high temporal resolution.

When investigations into even shorter time scales, on the order of attoseconds (10^{-18} s), become necessary, the demand for alternative approaches becomes apparent. High harmonic generation (HHG) can be used to generate intense attosecond pulses of electromagnetic radiation. These can, in turn, be used to measure ultrafast electronic processes [34, 35]. The emitted radiation from a system excited by very intense radiation may exhibit many integer multiples of the excitation frequencies. Higher harmonics with a large number of orders can be generated in atomic systems [36–46]. The observation of HHG in solids started only in the last decade [47–51]. Along with this, the properties of solid-state systems and the control, especially the enhancement of the higher harmonics, have been investigated in more detail [52, 53]. Only recently the influence of excitonic effects on HHG was investigated [54, 55].

Typically, the interaction of electrons in photoexcited semiconductors significantly modifier the nonlinear response [56]. For instance, in the case of low-dimensional semiconductor structures, such as quantum wells (QW) or quantum dots (QD), due to the confinement of electrons many-body interactions are enhanced. Consequently, it is necessary to include such interactions within a microscopic description. The influence of the Coulomb interaction has been studied by microscopic theories [57–63] and was observed by ultrafast spectroscopy [64–75].

In this thesis, we investigate various aspects of extreme nonlinear processes appearing in wave-mixing experiments and HHG. Chapter 2 covers the fundamental concepts required to describe the interaction between classical light and semiconductor nanostructures. We introduce the multi-band semiconductor Bloch equations (SBE) in the length gauge, which includes both inter- and intraband excitations and the many-body Coulomb interaction within the time-dependent Hartree-Fock approximation (TDHF). The first part of our work focuses on high-field effects associated with strong, often Terahertz (THz), laser pulses. In addition to interband transitions, we investigate intraband excitations that arise from the acceleration of charge carriers. In Chapter 3, we investigate a strongly nonresonant FWM experiment using the SBE within a two-band model, highlighting the importance of the intraband motion. In Chapter 4 we analyze the anisotropic behavior of the interband HHG in MgO using the SBE, along with a semiclassical trajectory theory that directly links the electron/hole motion to harmonic emission in both real and momentum space. We clarify that certain scattering processes are responsible for the anisotropic interband HHG observed in MgO.

The second part of the thesis extends our theoretical treatment by considering the many-

body Coulomb interaction. In chapter 5 a theoretical analysis of the influence of excitonic effects on HHG is shown. Here, the Coulomb interaction is treated in the TDHF approximation. By a proper choice of laser frequencies depending on the excitonic resonances it is possible that selective harmonics can be enhanced significantly. In Chapter 6 we go beyond the TDHF approximation by considering high-order correlation effects, including the excitation of biexcitons. Within the coherent $\chi^{(3)}$-limit a decoupling scheme can be applied to truncate the many-body hierarchy, which results in a closed set of equations describing both single- and two-exciton coherences. We compare the nonlinear response of spatially-direct type-I QW structures and the spatially-indirect type-II QW structures. In properly designed type-II QW structures so-called charge transfer excitons represent the energetically-lowest interband transitions. The theoretical treatment of such material systems reveals that additional contributions to the nonlinear optical response appear due to the spatial inhomogeneity, which is confirmed by comparing with optical-pump optical-probe (OPOP) experiments. In the end we give a summary of the results obtained in this thesis.

Fundamentals

<div style="text-align: right; font-size: 3em;">2</div>

In this chapter, we present the fundamental concepts to understand the background underlying the numerical simulations discussed in chapters 3-5 of this thesis. We introduce a microscopic description of the light-matter interaction in semiconductors. The described methodologies and models are based on the concepts of Refs. [2, 76, 77]. Here, we restrict the treatment of the Coulomb interaction to the TDHF approximation. Overall, we follow a semiclassical approach, where electronic excitations are treated quantum mechanically and the light field is a classical electromagnetic wave. We start by introducing the Hamiltonian of the system. Subsequently, we derive the dynamical equations of motion and introduce physical quantities that describe the response to the light-matter interaction. In the end of this chapter we introduce the concept of investigating nonlinear optical experiments considering FWM and PP setups theoretically. In the second part of this thesis, i.e., chapter 6, we introduce a theoretical model to analyze the nonlinear response including additionally higher-order biexcitonic Coulomb correlation effects.

2.1 Semiclassical description of the light-matter interaction in semiconductors

The microscopic treatment of the material system is provided in second quantization by the Hamiltonian in the Bloch basis [2, 76]. Therefore, we introduce creation and annihilation operators $\hat{a}_{\lambda,\mathbf{k}}^{\dagger}$ and $\hat{a}_{\lambda,\mathbf{k}}$ for the electronic system, respectively. They create or destroy an electron in the corresponding band λ with crystal momentum $\hbar\mathbf{k}$. The multi-band Hamiltonian describing optical and intraband excitations reads

$$\hat{H} = \hat{H}_0 + \hat{H}_{L-M} + \hat{H}_C. \tag{2.1}$$

The first term $\hat{H}_0 = \sum_{\lambda\mathbf{k}} \varepsilon_{\mathbf{k}}^{\lambda} \hat{a}_{\lambda,\mathbf{k}}^{\dagger} \hat{a}_{\lambda,\mathbf{k}}$ of the Hamiltonian in eq. (2.1) describes the energy of electrons within the material system. The light-matter interaction $\hat{H}_{L-M}$ includes two different processes in length gauge ($\mathbf{x}\cdot\mathbf{E}$ picture [78, 79]). Neglecting the so called non-Abelian Berry connections [80] it is given by:

$$\hat{H}_{L-M} = -\mathbf{E}(t) \cdot \sum_{\substack{\lambda,\lambda',\mathbf{k} \\ \lambda \neq \lambda'}} \boldsymbol{\mu}_{\mathbf{k}}^{\lambda\lambda'} \hat{a}_{\lambda,\mathbf{k}}^{\dagger} \hat{a}_{\lambda,\mathbf{k}} + ie\mathbf{E}(t) \cdot \sum_{\lambda,\mathbf{k}} \hat{a}_{\lambda,\mathbf{k}}^{\dagger} \nabla_{\mathbf{k}} \hat{a}_{\lambda,\mathbf{k}}. \tag{2.2}$$

The transition dipole matrix element $\boldsymbol{\mu}_{\mathbf{k}}^{\lambda\lambda'} = e\langle\lambda,\mathbf{k}|\,\hat{\mathbf{r}}\,|\lambda',\mathbf{k}\rangle$ defines the strength of an interband excitation of an electron from band λ to λ' due to an electric field. The $\nabla_{\mathbf{k}}$ term in eq. (2.2) leads to intraband currents [79, 81] which are induced by the acceleration of electrons in their respective bands λ according to the classical acceleration theorem [82]. So, within the length gauge it is possible to distinguish between inter- and intraband currents [83, 84]. We can associate them with the corresponding intraband acceleration and the interband transition processes. Here, we neglect any kind of scattering mechanisms on the carrier motion. The intraband currents play an important role when exciting semiconductors far below the bandgap energy, e.g., in THz spectroscopy or HHG [78, 79, 83, 85–92]. The Coulomb interaction $\hat{H}_C$ describes the interaction between the electrons in bands λ and λ' exchanging the momentum $\hbar\mathbf{q}$, and is given by

$$\hat{H}_C = \frac{1}{2}\sum_{\substack{\lambda,\lambda'\\ \mathbf{k},\mathbf{k'}\mathbf{q}\neq 0}} V_{\mathbf{q}}^{\lambda\lambda'}\,\hat{a}_{\lambda,\mathbf{k}+\mathbf{q}}^{\dagger}\hat{a}_{\lambda',\mathbf{k'}-\mathbf{q}}^{\dagger}\hat{a}_{\lambda',\mathbf{k'}}\hat{a}_{\lambda,\mathbf{k}}. \tag{2.3}$$

The Coulomb matrix element $V_{\mathbf{q}}^{\lambda\lambda'}$ depends on the considered material system. Further many-body interactions as electron-phonon interactions which may lead to the formation of quasi-particles and dephasing and relaxation are not considered here. These kind of interactions are only treated on a phenomenological approach by introducing effective parameters.

2.2 The SBE in TDHF approximation

By considering the system Hamiltonian from the previous chapter and the Heisenberg equation it is possible to describe the dynamics of any arbitrary physical observable $\hat{O}$ [2, 93]

$$\langle\frac{d}{dt}\hat{O}\rangle = \frac{i}{\hbar}\langle\big[\hat{O},\hat{H}\big]\rangle. \tag{2.4}$$

Here, we indicate that the relevant physical quantities to describe a photoexcited semiconductor are the microscopic polarizations $p_{\mathbf{k}}^{\lambda\lambda'} = \langle\hat{a}_{\lambda,\mathbf{k}}^{\dagger}\hat{a}_{\lambda',\mathbf{k}}\rangle$ ($\lambda\neq\lambda'$) and the populations $n_{\mathbf{k}}^{\lambda} = \langle\hat{a}_{\lambda,\mathbf{k}}^{\dagger}\hat{a}_{\lambda,\mathbf{k}}\rangle$. By inserting these quantities into the Heisenberg equation (2.4) it is possible to obtain their time evolution. However, the commutation with the specified Coulomb Hamiltonian (2.3) leads to an hierarchy problem. The relevant quantities $p_{\mathbf{k}}^{\lambda\lambda'}$ and $n_{\mathbf{k}}^{\lambda}$ couple to higher order products of the electronic operators $\hat{a}_{\mathbf{k}}^{\dagger\lambda}$ and $\hat{a}_{\mathbf{k}}^{\lambda}$ including two creation and two annihilation operators. Subsequently, it is necessary to derive the equation of motion governing these quantities, which exhibit coupling with six operators. This coupling gives

rise to an infinite set of equations, which can be represented symbolically as follows: [56]

$$\frac{\partial}{\partial t}\langle N \rangle = T\left[\langle N \rangle\right] + V\left[\langle N+1 \rangle\right]$$

(2.5)

Here, the product of N creation and N annihilation operators is defined by $\langle N \rangle$. The free particle evolution is given by the functional T and the interacting many-body part by V, respectively. To determine the dynamics of the considered system it is necessary to truncate the infinite hierarchy to obtain a closed set of equations of motion. A widely used approach to truncate the hierarchy problem is the cluster expansion [76, 94–96]. It provides a closed set of equations for analyzing many-body Coulomb correlation effects [97–103]. The singlet level of the cluster expansion is equal to the case of the TDHF approximation. Latter treats the Coulomb interaction in first order and neglects many-body correlations. In principle, every N-particle quantity $\langle N \rangle$ includes both single-particle contributions as well as many-body correlations. Applying the so-called Hartree-Fock (HF) factorization according to [2], a two-particle cluster is factorized into products of singlets

$$\langle \hat{a}_1^\dagger \hat{a}_2^\dagger \hat{a}_3 \hat{a}_4 \rangle \overset{HF}{\approx} \langle \hat{a}_1^\dagger \hat{a}_4 \rangle \langle \hat{a}_2^\dagger \hat{a}_3 \rangle - \langle \hat{a}_1^\dagger \hat{a}_3 \rangle \langle \hat{a}_2^\dagger \hat{a}_4 \rangle.$$

(2.6)

Within the TDHF approximation the dynamics of the expectation value of a four-point operator is determined by the dynamics of two-point operator expectation values. After utilizing the HF factorization the difference between the full and the HF terms describes the scattering part (truly correlated pairs of charge carriers) which can be written as

$$\partial_t \langle \hat{O} \rangle = \partial_t \langle \hat{O} \rangle_{HF} + \partial_t \langle \hat{O} \rangle|_{scatt}.$$

(2.7)

Due to the typically relatively small number of electrons excited from the valence band v to the conduction band c compared to the total number of electrons occupying the filled valence band, it is advantageous to transform to the electron-hole picture. This approach involves focusing only on the few missing electrons in the valence band, known as holes h. Here, we introduce the creation operators for electrons $c_{\mathbf{k}}^\dagger$ and holes $d_{\mathbf{k}}^\dagger$, respectively by defining:

$$\hat{c}_{\mathbf{k}}^\dagger \equiv \hat{a}_{c,\mathbf{k}}^\dagger \text{ and } \hat{d}_{-\mathbf{k}}^\dagger \equiv \hat{a}_{v,\mathbf{k}}$$

(2.8)

For simplicity, we consider one valence band and one conduction band. It should be noted, that in the following we take only Coulomb interaction processes into account that conserve the particle number within each band. Specifically, we do not consider interband Coulomb processes that involve the annihilation of one electron and one hole, resulting in the creation of two electrons or holes, respectively. We neglect terms that

characterize interband Auger transitions because they are not important for the material systems and excitation conditions considered here. This approximation can be justified by the substantial energy gap, that exists between the two bands which exceeds typical Coulomb energy scales, e.g., the exciton binding energy. Furthermore, by inserting the definitions (2.8) into the Hamiltonian (2.1) and restoring normal ordering, one obtains constant terms which we omit because they do not affect the dynamics of the system [2]. The Hamiltonian in the electron-hole picture in two-band approximation reads

$$
\begin{aligned}
\hat{H} = &\sum_{\mathbf{k}} \left(\varepsilon_{\mathbf{k}}^{e} \hat{c}_{\mathbf{k}}^{\dagger} \hat{c}_{\mathbf{k}} + \varepsilon_{\mathbf{k}}^{h} \hat{d}_{-\mathbf{k}}^{\dagger} \hat{d}_{-\mathbf{k}} \right) \\
&- \sum_{\mathbf{k}} \mathbf{E}(t) \cdot \left(\mu_{\mathbf{k}}^{eh} \hat{c}_{\mathbf{k}}^{\dagger} \hat{d}_{-\mathbf{k}}^{\dagger} + \text{h.c} \right) + ie \sum_{\mathbf{k}} \mathbf{E}(t) \cdot \left(\hat{c}_{\mathbf{k}}^{\dagger} \nabla_{\mathbf{k}} c_{\mathbf{k}} - \hat{d}_{-\mathbf{k}}^{\dagger} \nabla_{\mathbf{k}} \hat{d}_{-\mathbf{k}} \right) \\
&+ \frac{1}{2} \sum_{\mathbf{k},\mathbf{k}',\mathbf{q}\neq 0} V_{q} \left(\hat{c}_{\mathbf{k}+\mathbf{q}}^{\dagger} \hat{c}_{\mathbf{k}'-\mathbf{q}}^{\dagger} \hat{c}_{\mathbf{k}'} \hat{c}_{\mathbf{k}} + \hat{d}_{\mathbf{k}+\mathbf{q}}^{\dagger} \hat{d}_{\mathbf{k}'-\mathbf{q}}^{\dagger} \hat{d}_{\mathbf{k}'} \hat{d}_{\mathbf{k}} - 2\hat{c}_{\mathbf{k}+\mathbf{q}}^{\dagger} \hat{d}_{\mathbf{k}'-\mathbf{q}}^{\dagger} \hat{d}_{\mathbf{k}'} \hat{c}_{\mathbf{k}} \right).
\end{aligned}
\tag{2.9}
$$

The Hamiltonian (2.9) contains the single particle energies

$$
\varepsilon_{\mathbf{k}}^{e} = \varepsilon_{\mathbf{k}}^{c}
\tag{2.10}
$$

and

$$
\varepsilon_{\mathbf{k}}^{h} = -\varepsilon_{\mathbf{k}}^{v} + \sum_{\mathbf{q}\neq 0} V_{q},
\tag{2.11}
$$

where the kinetic energy of the holes includes the Coulomb exchange energy of $-\sum V_{q}$. Inserting the microscopic polarization $p_{\mathbf{k}}^{he} = \langle \hat{d}_{-\mathbf{k}}^{h} \hat{c}_{\mathbf{k}}^{e} \rangle$ and the carrier density of electrons (holes) $n^{e} = \langle \hat{c}_{\mathbf{k}}^{\dagger} \hat{c}_{\mathbf{k}} \rangle$ ($n^{h} = \langle \hat{d}_{-\mathbf{k}}^{\dagger} \hat{d}_{-\mathbf{k}} \rangle$) into the Heisenberg eq. (2.4) with the electron-hole Hamiltonian (2.9) their dynamics can be determined. Within the TDHF approximation (singlet-level), a closed set of equations of motion including only two-point quantities can be derived. The SBE for a two-band model read [2]

$$
\begin{aligned}
i\hbar \frac{\partial}{\partial t} p_{\mathbf{k}}^{he} &= \left(\tilde{\varepsilon}_{\mathbf{k}}^{e} + \tilde{\varepsilon}_{\mathbf{k}}^{h} + ie\mathbf{E}(t) \cdot \nabla_{\mathbf{k}} \right) p_{\mathbf{k}}^{he} - \hbar\Omega_{\mathbf{k}}^{he} \left(1 - n_{\mathbf{k}}^{e} - n_{\mathbf{k}}^{h} \right) + \Gamma_{\mathbf{k}}^{he}, \\
\hbar \frac{\partial}{\partial t} n_{\mathbf{k}}^{\lambda} &= -2\text{Im} \left[\hbar\Omega_{\mathbf{k}}^{he} \left(p_{\mathbf{k}}^{he} \right)^{*} \right] + e\mathbf{E}(t) \cdot \nabla_{\mathbf{k}} n_{\mathbf{k}}^{\lambda} + \Gamma_{\mathbf{k}}^{\lambda} \quad \text{with} \quad \lambda \in e, h.
\end{aligned}
\tag{2.12}
$$

The scattering processes are approximated using effective dephasing constants denoted as $\Gamma_{\mathbf{k}}^{he} = -i\frac{\hbar}{T_{2}} p_{\mathbf{k}}^{he}$ for the polarizations. The relaxation of occupations is given by $\Gamma_{\mathbf{k}}^{\lambda} = -\frac{1}{T_{1}} n_{\mathbf{k}}^{\lambda}$.[1]

---

[1] Usually, we use infinite lifetimes for the populations.

The Coulomb interaction leads to a renormalization of the band energies according to

$$\tilde{\varepsilon}_{\mathbf{k}}^{\lambda} = \varepsilon_{\mathbf{k}}^{\lambda} - \sum_{\mathbf{q} \neq \mathbf{k}} V_{\mathbf{k}\text{-}\mathbf{q}} n_{\mathbf{q}}^{\lambda} \ \text{ with } \ \lambda \in e, h. \tag{2.13}$$

The generalized Rabi energy which contain the product between the electric field $\mathbf{E}(t)$ and the dipole matrix element $\mu_{\mathbf{k}}^{eh}$ is included via

$$\hbar \Omega_{\mathbf{k}}^{he} = \left(\mu_{\mathbf{k}}^{eh} \right)^{*} \cdot \mathbf{E}(t) + \sum_{\mathbf{q} \neq \mathbf{k}} V_{\mathbf{k}\text{-}\mathbf{q}}^{he} p_{\mathbf{q}}^{he}. \tag{2.14}$$

By considering several valence bands $\lambda = h_i$ and/or conduction bands $\lambda' = e_j$ provides a more realistic representation of the electronic structure and enables a more precise description of absorption, emission, and other optical processes of photoexcited semiconductors. The coherences between these bands also contribute to the optical response [104]. Here, the polarization $p_{\mathbf{k}}^{h_i e_j}$ describes the interband transition between a valence band h_i and a conduction band e_j. Furthermore, coherences $p_{\mathbf{k}}^{h_i h_j}$ and $p_{\mathbf{k}}^{e_i e_j}$ between two different valence bands $h_i \neq h_j$ and conduction bands $e_i \neq e_j$ appear. On the singlet level which treats the Coulomb interaction in the TDHF approximation the equations of motion provided for a

multi-band system read [2, 104]

$$
\begin{aligned}
i\hbar\frac{\partial}{\partial t}p_{\mathbf{k}}^{h_i e_j} &= \left(\tilde{\varepsilon}_{\mathbf{k}}^{e_j} + \tilde{\varepsilon}_{\mathbf{k}}^{h_i} + ie\mathbf{E}(t)\cdot\nabla_{\mathbf{k}}\right)p_{\mathbf{k}}^{h_i e_j} - \hbar\Omega_{\mathbf{k}}^{h_i e_j}\left(1 - n_{\mathbf{k}}^{e_j} - n_{\mathbf{k}}^{h_i}\right) + \Gamma_{\mathbf{k}}^{h_i e_j} \\
&\quad + \sum_{e_\lambda \neq e_j}\left[\hbar\Omega_{\mathbf{k}}^{h_i e_\lambda}p_{\mathbf{k}}^{e_\lambda e_j} - \hbar\Omega_{\mathbf{k}}^{e_\lambda e_j}p_{\mathbf{k}}^{e_\lambda e_j}\right] \\
&\quad + \sum_{h_\lambda \neq h_i}\left[\hbar\Omega_{\mathbf{k}}^{h_i h_\lambda}p_{\mathbf{k}}^{h_\lambda e_j} - \hbar\Omega_{\mathbf{k}}^{h_\lambda e_j}p_{\mathbf{k}}^{h_i h_\lambda}\right], \\
i\hbar\frac{\partial}{\partial t}p_{\mathbf{k}}^{e_i e_j} &= \left(\tilde{\varepsilon}_{\mathbf{k}}^{e_j} - \tilde{\varepsilon}_{\mathbf{k}}^{e_i} + ie\mathbf{E}(t)\cdot\nabla_{\mathbf{k}}\right)p_{\mathbf{k}}^{e_i e_j} - \hbar\Omega_{\mathbf{k}}^{e_i e_j}\left(n_{\mathbf{k}}^{e_j} - n_{\mathbf{k}}^{e_i}\right) + \Gamma_{\mathbf{k}}^{e_i e_j} \\
&\quad + \sum_{e_\lambda \neq e_i, e_j}\left[\hbar\Omega_{\mathbf{k}}^{e_i e_\lambda}p_{\mathbf{k}}^{e_\lambda e_j} - \hbar\Omega_{\mathbf{k}}^{e_\lambda e_j}p_{\mathbf{k}}^{e_i e_\lambda}\right] \\
&\quad + \sum_{h_\lambda}\left[\hbar\left(\Omega_{\mathbf{k}}^{h_\lambda e_i}\right)^*p_{\mathbf{k}}^{h_\lambda e_j} - \hbar\Omega_{\mathbf{k}}^{h_\lambda e_j}\left(p_{\mathbf{k}}^{h_\lambda e_i}\right)^*\right] \text{ with } e_i \neq e_j, \\
i\hbar\frac{\partial}{\partial t}p_{\mathbf{k}}^{h_i h_j} &= \left(\tilde{\varepsilon}_{\mathbf{k}}^{h_j} - \tilde{\varepsilon}_{\mathbf{k}}^{h_i} + ie\mathbf{E}(t)\cdot\nabla_{\mathbf{k}}\right)p_{\mathbf{k}}^{h_i h_j} - \hbar\Omega_{\mathbf{k}}^{h_i h_j}\left(n_{\mathbf{k}}^{h_j} - n_{\mathbf{k}}^{h_i}\right) + \Gamma_{\mathbf{k}}^{h_i h_j} \\
&\quad + \sum_{h_\lambda \neq h_i, h_j}\left[\hbar\Omega_{\mathbf{k}}^{h_i h_\lambda}p_{\mathbf{k}}^{h_\lambda h_j} - \hbar\Omega_{\mathbf{k}}^{h_\lambda h_j}p_{\mathbf{k}}^{h_i h_\lambda}\right] \\
&\quad + \sum_{e_\lambda}\left[\hbar\left(\Omega_{\mathbf{k}}^{e_\lambda h_i}\right)^*p_{\mathbf{k}}^{e_\lambda h_j} - \hbar\Omega_{\mathbf{k}}^{e_\lambda h_j}\left(p_{\mathbf{k}}^{e_\lambda h_i}\right)^*\right] \text{ with } h_i \neq h_j.
\end{aligned}
\tag{2.15}
$$

Here, additional couplings between all microscopic polarizations due to the generalized Rabi energy exist and is given by [2, 104].

$$
\hbar\Omega_{\mathbf{k}}^{\lambda\lambda'} = \left(\mu_{\mathbf{k}}^{\lambda\lambda'}\right)^* \cdot \mathbf{E}(t) + \sum_{\mathbf{q}\neq\mathbf{k}}V_{\mathbf{k}\text{-}\mathbf{q}}^{\lambda\lambda'}p_{\mathbf{q}}^{\lambda\lambda'}.
\tag{2.16}
$$

The occupation dynamics in the valence (h_i) and the conduction (e_j) bands in a multi-band system read [2, 104]

$$\frac{\partial}{\partial t} n_{\mathbf{k}}^{e_i} = -2\mathrm{Im} \left[\sum_{e_\lambda \neq e_i} \Omega_{\mathbf{k}}^{e_\lambda e_i} \left(p_{\mathbf{k}}^{e_\lambda e_i} \right)^* + \sum_{h_\lambda} \Omega_{\mathbf{k}}^{h_\lambda e_i} \left(p_{\mathbf{k}}^{h_\lambda e_i} \right)^* \right] + \frac{e}{\hbar} \mathbf{E}(t) \cdot \nabla_{\mathbf{k}} n_{\mathbf{k}}^{e_i} + \Gamma_{\mathbf{k}}^{e_i},$$

$$\frac{\partial}{\partial t} n_{\mathbf{k}}^{h_i} = -2\mathrm{Im} \left[\sum_{h_\lambda \neq vi} \Omega_{\mathbf{k}}^{h_i h_\lambda} \left(p_{\mathbf{k}}^{h_i e_\lambda} \right)^* + \sum_{e_\lambda} \Omega_{\mathbf{k}}^{h_i e_\lambda} \left(p_{\mathbf{k}}^{h_i e_\lambda} \right)^* \right] + \frac{e}{\hbar} \mathbf{E}(t) \cdot \nabla_{\mathbf{k}} n_{\mathbf{k}}^{h_i} + \Gamma_{\mathbf{k}}^{h_i}.$$

$$(2.17)$$

The closed set of equations in (2.15) and (2.17) is known as the multi-band SBE [2, 104]. The interband polarization $\mathbf{P}(t)$ is fully determined by the eqs. (2.15) and (2.17). Only the microscopic polarizations $p_{\mathbf{k}}^{\lambda \lambda'}$ between dipole-coupled bands λ and λ' contribute to the total interband polarization $\mathbf{P}(t)$ which is given by

$$\mathbf{P}(t) = \sum_{\lambda, \lambda', \mathbf{k}} \boldsymbol{\mu}_{\mathbf{k}}^{\lambda \lambda'} p_{\mathbf{k}}^{\lambda \lambda'}. \tag{2.18}$$

The intraband current is given by

$$\mathbf{J}(t) = \sum_{\lambda, \mathbf{k}} \mathbf{v}_{\mathbf{k}}^{\lambda} n_{\mathbf{k}}^{\lambda} = \sum_{\lambda, \mathbf{k}} \frac{e}{\hbar} \nabla_{\mathbf{k}} \varepsilon_{\mathbf{k}}^{\lambda} n_{\mathbf{k}}^{\lambda}. \tag{2.19}$$

The derivative of band dispersion defines the current matrix element $v_{\mathbf{k}}^{\lambda} = \frac{e}{\hbar} \nabla_{\mathbf{k}} \varepsilon_{\mathbf{k}}^{\lambda}$. When considering symmetric band structures in $\mathbf{k}$-space, the intraband current only exists for non-symmetric carrier distributions.

2.3 Nonlinear optical signals
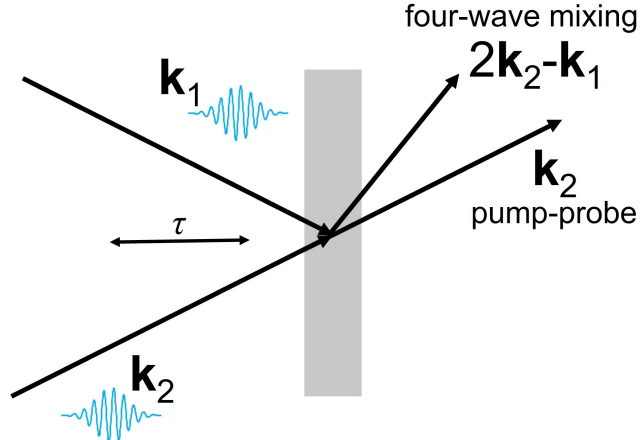
Figure 2.1: Schematical illustration of a PP setup and a FWM experiment in the self-diffraction geometry induced by two laser pulses which are delayed by τ.

In the following we describe nonlinear optical experiments considering FWM and PP setups for near-gap excitations, i.e., near resonant excitations. Here, the nonlinear response is determined by the macroscopic polarization **P**. In chapter 3, we additionally show how to include intraband contributions to the nonlinear optical response. The nonlinear optical experiments like PP and FWM considered in this thesis are always performed with two excitation pulses that propagate into the directions $\mathbf{k}_1$ and $\mathbf{k}_2$, respectively. The total electric field within the rotating wave approximation (RWA) is given by [105, 106]

$$
\mathbf{E}(t) = \mathbf{e}_1 E_1(t) e^{i(\mathbf{k}_1 \cdot \mathbf{r} - \omega_1 t)} + \mathbf{e}_2 E_2(t) e^{i(\mathbf{k}_2 \cdot \mathbf{r} - \omega_2 t)}
$$
$$
\text{with } E_1(t) \propto e^{-\left(\frac{t+\tau}{\Delta t_1}\right)^2} \text{ and } E_2(t) \propto e^{-\left(\frac{t}{\Delta t_2}\right)^2} \tag{2.20}
$$

The electric field polarization vectors are given by $\mathbf{e}_1$ and $\mathbf{e}_2$, whereas the pulse frequencies are given by ω_1 and ω_2, respectively. The temporal envelopes $E_{1,2}(t)$ are described by Gaussian functions. The delay between them is given by the time τ, see Fig. 2.1. The second pulse $E_2(t)$ is centered at the time $t = 0$ and the first pulse $E_1(t)$ excites the system either before pulse $E_2(t)$ corresponding to a positive delay time or afterwards with a negative delay time. In the scope of this work the theoretical analysis of the nonlinear signals concerning FWM or PP is restricted up to the third-order of the considered electric fields. In addition, a Fourier decomposition with respect to the propagation directions $\mathbf{k}_1$ and $\mathbf{k}_2$

of the relevant physical quantities is necessary [31]. For instance, the first order consists of two linear interband coherences $p^{(1)(1|0)}$ and $p^{(1)(0|1)}$ induced by the corresponding laser pulses. The superscript $(l)(n|m)$ indicates the order l in the electric field and the kinematic direction $e^{i(n\mathbf{k}_1 + m\mathbf{k}_2) \cdot \mathbf{r}}$ [56]. At this point, it should be noted that the relevant quantities in second order are either carrier densities or, as we will discuss later in this work, two-exciton coherences (see. A.1.1). The time-resolved FWM (TR-FWM) signal from the self-diffraction geometry, (see Fig. 2.1), is radiated in the direction $2\mathbf{k}_2 - \mathbf{k}_1$ and is theoretically described by [56]

$$\mathbf{P}_{\text{FWM}}(t, \tau) = \sum_{\lambda, \lambda', \mathbf{k}} \boldsymbol{\mu}_{\mathbf{k}}^{\lambda \lambda'} \left(p_{\mathbf{k}}^{\lambda \lambda'} \right)^{(3)(-1|2)} (t, \tau).$$ (2.21)

The absolute value squared of the TR-FWM signal polarization provides its intensity which is proportional to what is measured in TR-FWM experiments from optically thin samples and is given by [56]

$$S_{\text{FWM}}(t, \tau) = |\mathbf{P}_{\text{FWM}}(t, \tau)|^2$$ (2.22)

and the time-integrated signal is given by [56]

$$I_{\text{FWM}}(\tau) = \int_{-\infty}^{\infty} |\mathbf{P}_{\text{FWM}}(t, \tau)|^2 dt$$ (2.23)

In PP experiments one usually excites the material system with an optical pump pulse which corresponds in our theoretical treatment to pulse $\mathbf{E}_1(t)$. Afterwards one is often interested in the pump-induced absorption changes from the radiated field into the probe pulse (pulse $\mathbf{E}_2(t)$) direction $(0|1)$, compare with Fig. 2.1. The pump-induced absorption change $\delta\alpha$ is determined by the differential polarization $\delta\mathbf{P}$. Here, the optical pump pulse $(\mathbf{E}_1(t))$ enters twice and the probe pulse $(\mathbf{E}_2(t))$ linearly to the differential polarization $\delta\mathbf{P}$. In case of an spectral broad probe spectrum the pump induced absorption spectrum is given by the Fourier transform of the time-dependent differential polarization [56]

$$\delta\alpha(\omega, \tau) \propto \text{Im} \left[\int (\mathbf{e}_2)^* \cdot \delta\mathbf{P}(t, \tau) e^{i\omega t} dt \right].$$ (2.24)

Strongly nonresonant four-wave mixing in semiconductors

3

In this chapter, we investigate a FWM experiment that utilizes strongly nonresonant laser pulses in self-diffraction geometry. Previous studies of FWM spectroscopy using excitations near the bandgap energy have successfully analyzed dephasing times [2, 14, 21, 22, 24, 31, 32, 56] as the interplay between different electronic states [18, 20, 107, 108], including excitonic [2, 16, 17, 24, 56, 109] and higher-order correlation effects such as biexcitons [2, 23, 29, 32, 56, 61, 62, 110–119]. Additionally, two-dimensional Fourier-transform spectroscopy has been employed in such studies [120, 121]. However, only a few FWM experiments have been conducted using nonresonant laser pulses [122–125]. In these cases, the FWM signals exhibit spectral broadening and shifts that have not been thoroughly analyzed using a microscopic theory.

Our approach is based on solving the SBE, which take into account inter- and intraband excitations within a two-band model. Previous studies have demonstrated that the generation of high harmonics with nonresonant excitations in the THz regime arises from both the inter- and intraband current [47, 49, 50, 81, 104]. To illustrate the impact of intraband excitations on the FWM signal, we compare our results with a simplified two-level model and a spectrally resolved FWM experiment on a bulk CdTe sample. The following results can be found in [126].

3.1 Two-level model
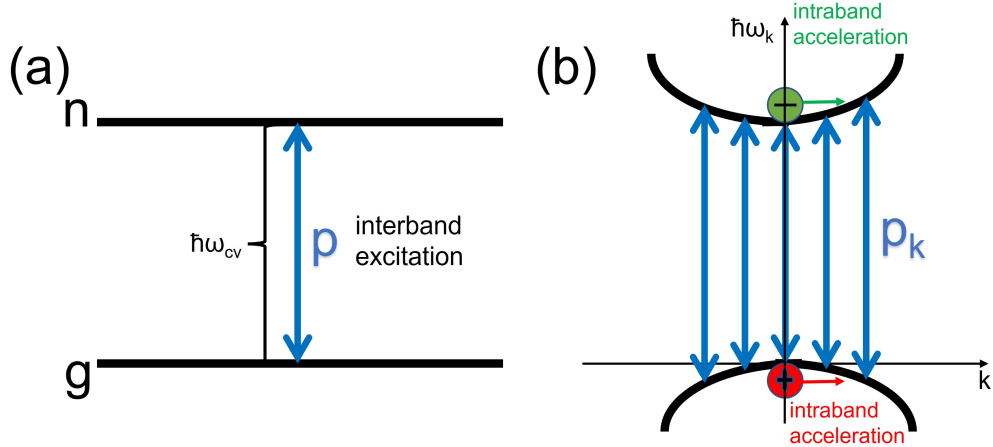
Figure 3.1: In (a) a schematic of a simple two-level system is shown providing only an interband excitation between a ground state g and an excited state n. The transition frequency is given by $\hbar\omega_{cv}$. In (b) the k-dependent dispersion $\hbar\omega_k$ is schematically shown. The total polarization is determined by the sum of all microscopic polarizations p_k. The electrons and holes move within their respective bands due to the field-induced acceleration.

For atomic systems described by a simple two-level system, see. Fig. 3.1(a), the well known optical Bloch equations (OBE) [2, 56] read

$$
\begin{aligned}
\frac{\partial}{\partial t}p &= -i\omega_{cv}p + \frac{i}{\hbar}\boldsymbol{\mu}\cdot\mathbf{E}(t)\,(1-2n) - \frac{p}{T_2}, \\
\frac{\partial}{\partial t}n &= \frac{i}{\hbar}\boldsymbol{\mu}\cdot\mathbf{E}(t)\,(p^* - p) - \frac{n}{T_1},
\end{aligned}
\tag{3.1}
$$

where p is the microscopic polarization and n the carrier density of the upper level. The occupation of the ground level is given by $(1-n)$. The transition frequency between the two states is given by ω_{cv}. The electric fields have the same pulse duration and central frequencies ω_L. Their temporal envelope corresponds to Gaussian pulses, see eq. (2.20). As mentioned in chapter 2.3 the third order interband polarization $P_{\mathrm{FWM}}^{(3)(-1|2)}$ determines the radiated signal into the direction $2\mathbf{k}_2 - \mathbf{k}_1$. Within an expansion in powers of the electric fields, the interaction between the linear polarizations $p^{(1)}$ due to E_1 and E_2 leads to the formation of a density grating $n^{(2)}$ in second order. At the same time the laser pulse E_2 interacts twice and is diffracted and leads to a third-order coherence $p^{(3)}$. Considering the Maxwell-Bloch equations to describe a region in space with multiple two-level systems, it is observed that in the self-diffraction geometry, two laser pulses generate a density grating. The second pulse is diffracted in the $2\mathbf{k}_2 - \mathbf{k}_1$ direction, see Fig. 3.2. The latter originates from Pauli blocking which is the only nonlinearity considering the OBE (3.1):
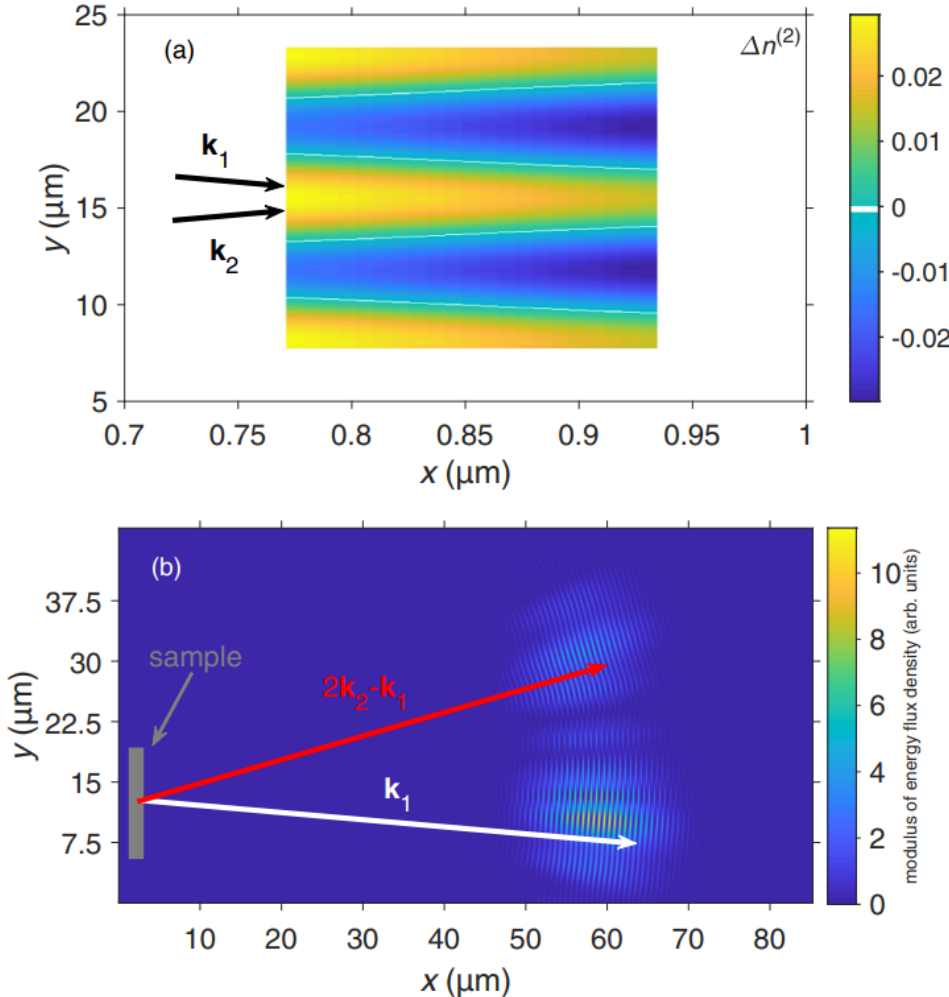
Figure 3.2: In (a) the density grating in second order $\Delta n^{(2)}$ excited by two-pulse configuration with $\mathbf{k}_{1,2}$ is shown at $t = 10$ fs. The medium in space is described by many two-level system considering the OBE (3.1) with $|d| = 0.624$ e nm. The bandgap energy is about $\omega_{cv} = 1.6$ eV and the laser frequencies correspond to $\omega_L = 0.6\omega_{cv}$ with a pulse duration of about 55 fs. Their maximum magnitude at $t = 0$ occurs at $x = 0.385$ μm. In (b) the radiated FWM signal (red arrow) which originates from the third-order polarization at $t = 200$ fs is shown. The propagation distance is about 60 μm at this time point. Taken from [126].

In principle, these steps still remain applicable for far off-resonant excitation with a detuning corresponding to $\Delta = \omega_{cv} - \omega_L$. In contrast to a resonant excitation the dynamics depends on the temporal envelope (adiabatic regime) of the considered laser pulses [2, 127]. Consequently, the coherence induced by the pulses vanished immediately if the electric fields are gone. Therefore, we only analyze the setup in which both laser pulses simultaneously impinge on the sample. The perturbative treatment to analyze the FWM

signal suggests that the amplitude scales as Δ^{-3} and the dynamics proceed faster because three excitations are leading to $P_{\text{FWM}}^{(3)}$.
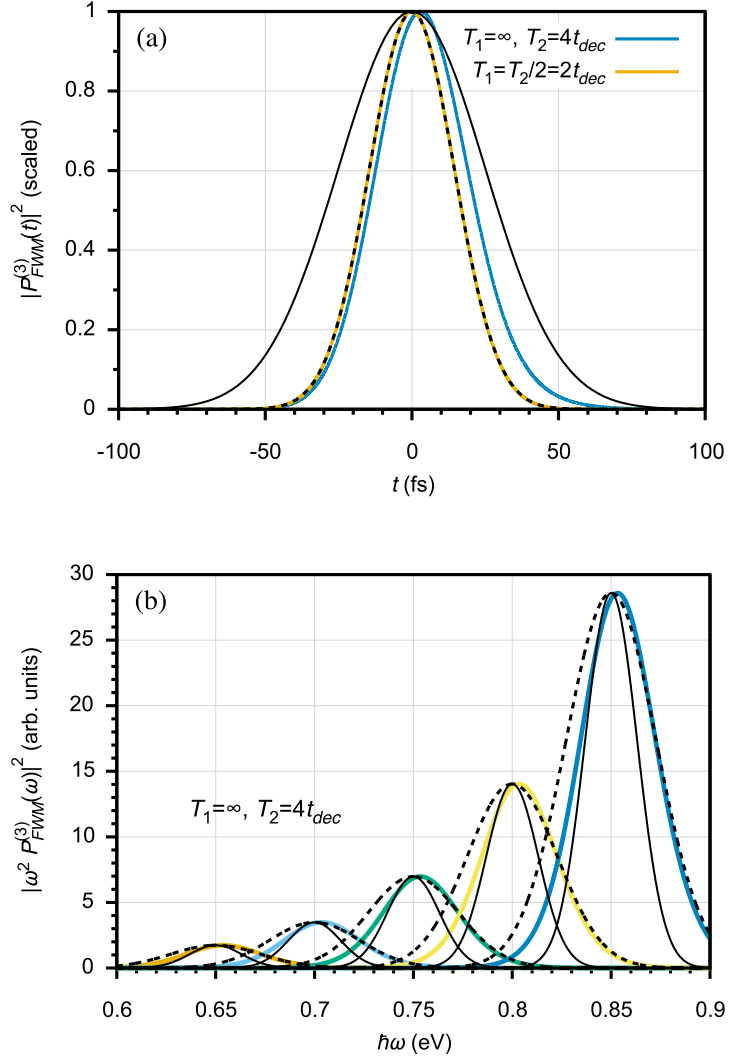
Figure 3.3: In (a) TR-FWM signal based on numerical solutions of the OBE (3.1) is shown for $\omega_L = 0.8$ eV ($\lambda_L = 1550$ nm). The black solid and dashed lines show the square of the pulse envelope, i.e., $[E(t)]^2$, and its third power $[E(t)]^6$, respectively. In (b) the FWM signal spectra depending on $\hbar\omega_L$ (thick colored lines) are shown. Like in (a) the black solid and dashed lines display the squared Fourier transforms of $E(t)$ and $[E(t)]^3$, respectively. The pulse duration corresponds to 50 fs and $\hbar\omega_{cv} = 1.5$ eV (close to the band gap of bulk GaAs) in both (a) and (b). Taken from [126].

Our theoretical results based on numerical solutions of the OBE (3.1) up to third-order show clearly in Fig. 3.3 that our predictions are valid. The TR-FWM intensity $I_{\text{FWM}}(t) \propto |P_{\text{FWM}}^{(3)}|^2$

mostly overlaps with $[E(t)]^6$ within the coherent limit ($T_2 = 2T_1$). Usually, in solid-state systems, the relaxation times T_1 are much longer than the corresponding dephasing times T_2. Assuming an infinite lifetime of the carrier densities the FWM signal exhibit a small temporal retardation when the dephasing time is shorter than the pulse duration. Here, the FWM intensity spectra $I_{\text{FWM}}^{(3)}(\omega) \propto |\omega^2 P_{\text{FWM}}^{(3)}(\omega)|^2$ are spectrally already broader than the widths of laser pulses $|E(\omega)|^2$, see Fig. 3.3(b). As predicted for an off-resonant excitation the theoretical results provide an overall scaling of the FWM intensity that is nearly $\omega_L^4 \Delta^{-6}$.

3.2 Two-band model

Besides the interband excitation ($\propto \boldsymbol{\mu} \cdot \mathbf{E}$), the acceleration of electron and holes ($\propto \mathbf{E} \cdot \nabla_{\mathbf{k}}$) induced by the electric fields is crucial to describe adequately solid-state systems when considering strong nonresonant pulses. We consider the SBE without Coulomb interactions, however including a $\mathbf{k}$-dependent energy dispersion $\hbar\omega_{\mathbf{k}}$, see Fig. 3.1(b),

$$
\begin{aligned}
\frac{\partial}{\partial t} p_{\mathbf{k}} &= -i\omega_{\mathbf{k}} p_{\mathbf{k}} + \frac{i}{\hbar} \boldsymbol{\mu} \cdot \mathbf{E}(t) \left(1 - 2n_{\mathbf{k}}\right) + \frac{e}{\hbar} \mathbf{E}(t) \cdot \nabla_{\mathbf{k}} p_{\mathbf{k}} - \frac{p_{\mathbf{k}}}{T_2}, \\
\frac{\partial}{\partial t} n_{\mathbf{k}} &= \frac{i}{\hbar} \boldsymbol{\mu} \cdot \mathbf{E}(t) \left(p_{\mathbf{k}}^* - p_{\mathbf{k}}\right) + \frac{e}{\hbar} \mathbf{E}(t) \cdot \nabla_{\mathbf{k}} - \frac{n_{\mathbf{k}}}{T_1}.
\end{aligned}
\tag{3.2}
$$

Now the nonlinear signal depends on the time derivative of the total current $\mathbf{J}(t) = \mathbf{J}_p(t) + \mathbf{J}_n(t)$:

$$
\begin{aligned}
\mathbf{J}_p(t) &= \frac{\partial}{\partial t} \mathbf{P}(t) \text{ with } \mathbf{P}(t) = \int d\mathbf{k} \boldsymbol{\mu} \left(p_{\mathbf{k}} + p_{\mathbf{k}}^*\right), \\
\mathbf{J}_n(t) &= -e \int d\mathbf{k} n_{\mathbf{k}} \nabla_{\mathbf{k}} \omega_{\mathbf{k}}.
\end{aligned}
\tag{3.3}
$$

As mentioned in chapter 2.2 the intraband current $J_n(t)$ is only finite for a symmetric band dispersion (derivative is an antisymmetric function in respect to $\mathbf{k}$) when the carrier density $n_{\mathbf{k}}$ contains contributions that are asymmetric in momentum space. Besides a small dependence on the different transition energies $\hbar\omega_{\mathbf{k}}$ the linear optical response corresponds to the case for a two-level model considering an unexcited solid-state system ($p_{\mathbf{k}}^{(0)} = n_{\mathbf{k}}^{(0)} = 0$). But due to the acceleration of carriers additional contributions which are absent within the two-level model can arise. For instance, in second order the coherence $p_{\mathbf{k}}^{(2)}$ is provided[1] by intraband excitations [128–130]. Even more pathways are needed to be considered in third order. The microscopic polarization $p_{\mathbf{k}}^{(3)}$ can be generated by an interband excitation of $n_{\mathbf{k}}^{(2)}$ like in the two-level model and additionally by an intraband

---

[1] The band dispersion $\omega_{\mathbf{k}}$ is a symmetric function which leads to an antisymmetric function of $p_{\mathbf{k}}^{(2)}$ with respect to $\mathbf{k}$. Then a macroscopic polarization in second order vanished due to the summation over $\mathbf{k}$.

excitation from $p_{\mathbf{k}}^{(2)}$. Similarly, a carrier density $n_{\mathbf{k}}^{(3)}$ arise due an interband (intraband) excitation from $p_{\mathbf{k}}^{(2)}$ ($n_{\mathbf{k}}^{(2)}$). Consequently, the total nonlinear response also depend on these new excitation pathways [128].
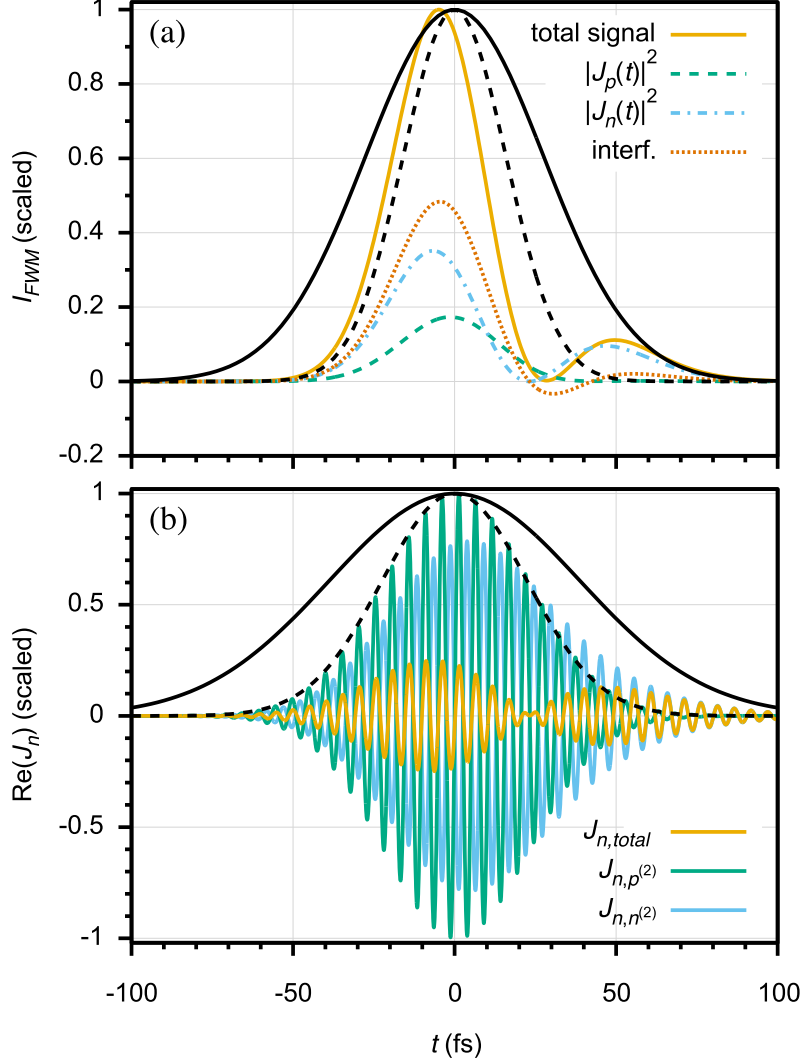
Figure 3.4: In (a) the total TR-FWM intensity signal $|J_p(t)+J_n(t)|^2$ with its separate contributions is shown. In (b) the real part of the intraband current J_n which depends on two excitation pathways $J_{n,p^{(2)}}$ and $J_{n,n^{(2)}}$ is presented. The currents $J_{n,p^{(2)}}$ and $J_{n,n^{(2)}}$ are also shown. In (b) the black solid and dashed lines correspond to $E(t)$ and $[E(t)]^3$, respectively. In (a) their squared envelopes are shown with the same line types. The laser frequency is $\omega_L = 0.8$ eV ($\lambda_L = 1550$ nm) and the pulse duration corresponds to 55 fs. The dephasing time is $T_2 = 150$ fs and $T_1 = \infty$. The material parameters are close to bulk GaAs with $\hbar\omega_{\mathbf{k}=0} = 1.58$ eV, $m_e^* = 0.1m_0$, $m_h^* = 0.5m_0$ and $|\mu| = 0.3e$ nm. Taken from [126].

The theoretical results in Fig. 3.4 based on numerical solutions of the SBE (3.2) consider-

ing an infinite lifetime T_1 and a dephasing time is 150 fs. The total FWM signal strongly depends on the contribution arising from intraband excitations. Within the present model the interband current $|J_p(t)|^2$ shows a very similar behavior with its Gaussian lineshape around $t \approx 0$ such as in the two-level model. Its notable that its magnitude is even smaller than from the density current $|J_n(t)|^2$ highlighting the importance of the intraband current. Since the total signal $|J_p + J_n(t)|^2$ depends on the summation of both currents an interference term $(J_p(t)J_n^*(t) + J_p^*(t)J_n(t))$ arises. A close look to Fig. 3.4 show some sign changes appearing around 20 fs due to the interference term. The global minimum of the total current is provided in this case near the maximum destructive interference between $J_p(t)$ and $J_n(t)$. The reason for these sign changes can be physically understood by considering the intraband current in more detail. The intraband current originates from two excitation pathways $p_{\mathbf{k}}^{(2)}$ and $n_{\mathbf{k}}^{(2)}$ providing a phase change in time domain. The dynamics of the interband excitation follows the temporal behavior of the electric fields whereas a temporal shift is observed from the contribution provided by the source term $n_{\mathbf{k}}^{(2)}$. This temporal shift vanishes by considering the coherent limit which is an unrealistic treatment for semiconductors. Both source terms leading to contributions that differ by the phase π.

Our theoretical findings can be confirmed by additional analytical considerations of $J_n(t)$. The source term $p_{\mathbf{k}}^{(2)}$ leads to $J_{n,p^{(2)}} \propto \left[i \left(\omega_{\mathbf{k}-2\omega_L} \right) + (1/T_2) \right]^{-1}$. Consequently two-photon absorption in $p_{\mathbf{k}}^{(2)}$ would appear when twice of the laser frequency ($2\hbar\omega_L$) surpasses the transition frequency. In the present model, the sign of $J_n(t)$ originating from the excitation pathway $p_{\mathbf{k}}^{(2)}$ strongly depends on the chosen laser frequency and whether it is smaller or larger than the band gap energy at certain $\mathbf{k}$ points. The transition frequencies $\omega_{\mathbf{k}}$ considered in Fig. 3.4 are all almost larger than $2\hbar\omega_L$ providing an opposite sign of $J_{n,p^{(2)}}$ and $J_{n,n^{(2)}}$ which is shown in Fig. 3.4(b). Considering slightly higher laser frequencies reduce this effect, resulting in a phase shift that does not exactly correspond to π. Consequently, the minimum of the intraband current $|J_n(t)|^2$ and the TR-FWM intensity signal does not reach zero. Overall, the double-peak structure originates from the different temporal behavior of the source terms $p_{\mathbf{k}}^{(2)}$ and $n_{\mathbf{k}}^{(2)}$. Firstly $J_{n,p^{(2)}}(t)$ dominates and at later times $J_{n,n^{(2)}}(t)$ is exceeding. This leads to to the two peaks in $J_n(t)$ and explains the occurrence of destructive and constructive interference.
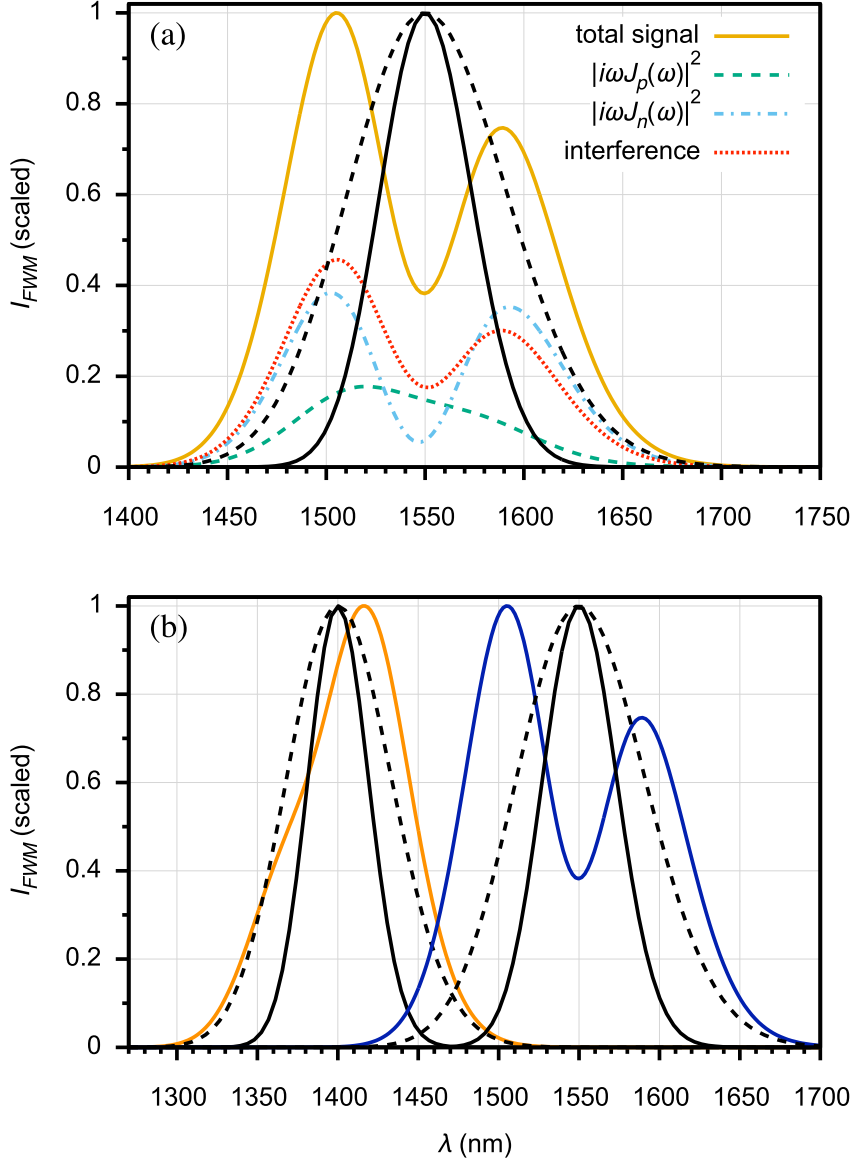
Figure 3.5: FWM intensity spectrum $|\omega J_p(\omega) + \omega J_n(\omega)|^2$. The solid and dashed black lines show the squared intensity spectra of the electric fields $|E(\omega)|^2$ and $|E(\omega)|^6$, respectively. In (a) the FWM signal with $\lambda_L = 1550$ nm and its individual contributions are shown. Other parameters are chosen as in Fig. 3.4. On the right side in (b) the same spectrum as in (a) is presented but we use an excitation wavelength $\lambda_L = 1400$ nm. Latter provides the excitation conditions from the experiment shown in Fig. 3.6. Taken from [126].

In Fig. 3.4 the phase shift in time domain corresponds to π which leads to the minimum of the FWM intensity spectrum close to the laser frequency ω_L. The double-peak structure appearing in frequency domain also arise due the TR-FWM signal which provides two peaks. Furthermore, the FWM intensity spectrum exhibits a more broadened spectrum

than of the incident pulses $|E(\omega)|^6$ since specific spectral components are diminished. Additionally in Fig. 3.5(b) theoretical results are shown considering excitation conditions (λ_L = 1400 nm) close to the FWM experiment, see. Fig. 3.6. Since the laser frequency is larger the destructive interference is reduced leading to a spectrum providing only one certain peak. Nevertheless, it is still possible to obtain some red shifted and blue shifted components. At this point, it is noteworthy that the agreement between our theoretical findings and the measurements can be further improved by considering shorter dephasing times T_2. However, in this work our goal is mainly to show the importance and influence of several excitation pathways arise from the intraband acceleration especially for strongly nonresonant excitation conditions.
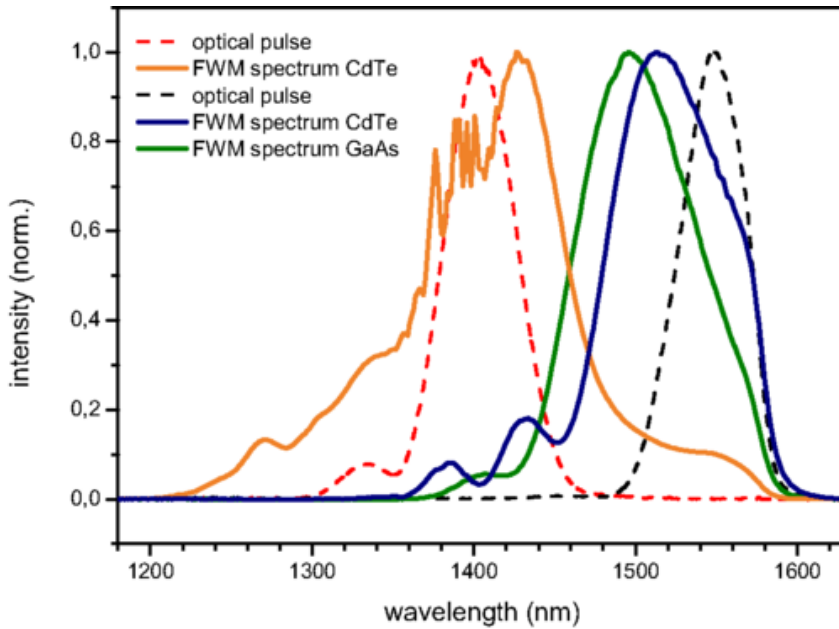
Figure 3.6: Measurements of self-diffracted FWM on CdTe and GaAs samples at a temperature of 10 K. The dotted lines show the transmitted pulses and represent the spectrum of the respective excitation pulses, whereas the FWM signals (solid lines) show a distinct spectral broadening. Taken from [126].

3.3 Conclusions

In this section, we identify intraband excitations as the primary source for the appearance of new signatures in the FWM signal for off-resonant excitation conditions. These excitations occur due to the acceleration of electrons induced by an electric field. We demonstrate that these new signatures appear when strongly nonresonant pulses with below half the interband transition frequency are applied.

A straightforward approach using a two-level model has already demonstrated the spectral

broadening of FWM signals under nonresonant excitation conditions. However, when considering the existence of different excitation pathways including an energy dispersion, constructive or destructive interference can occur. This leads to the emergence of complex signatures in the time and frequency domain of the FWM signal.

Our theoretical findings, based on numerical solutions of the SBE, are in good qualitative agreement with experimental results. This approach can be easily extended, for example, by considering a realistic band structure obtained from density functional theory or by including excitonic effects.

Overall, this approach offers many possibilities to investigate the dynamics of optical nonlinearities, even in higher orders than the present model. We can explore electronic couplings and many-body effects using strongly nonresonant excitations.

# Collision dynamics in solid-state high harmonic generation

4

Over the past few decades, the most common method for generating attosecond lasers has been atomic HHG [35, 131], as well as in molecules, e.g., O_2, N_2 [132], and CO_2 [133]. The relevant microscopic processes in such systems are well understood within a three-step collision model [134]. This model involves a field induced tunneling process, which leads to the liberation of an electron into the continuum. During the recombination process with its parent ion, high-order harmonics are emitted, which generate photons in the attosecond regime. These harmonics provide the possibility to investigate the ultrafast dynamics in such systems [135–140].

Since the first observation in ZnO in 2011 [47], HHG has been heavily investigated in many different solid-state systems [48, 81, 104, 141–149]. The theoretical treatment of the recombination process has also been applied to solid-state systems, indicating it as the main origin for interband HHG [47, 49, 51–53, 150–153]. In this case, the periodic arrangement of atoms gives rise to collision and scattering processes with neighboring atoms, leading to a much more complex behavior for the movement of the electron and its left-behind hole.

Therefore, the aim of this chapter is to establish a unified real and momentum space collision picture of HHG in solids, providing a direct mapping with the band structure of the considered material. Our theoretical findings suggest that the anisotropy in solid-state systems originates from backward/forward scattering processes between the particles with neighboring atoms and can be found in [154]. We will start by introducing and deriving the corresponding equations to describe the trajectories of electrons in solids using classical methods.

4.1 Semiclassical three-step recollision model in solids
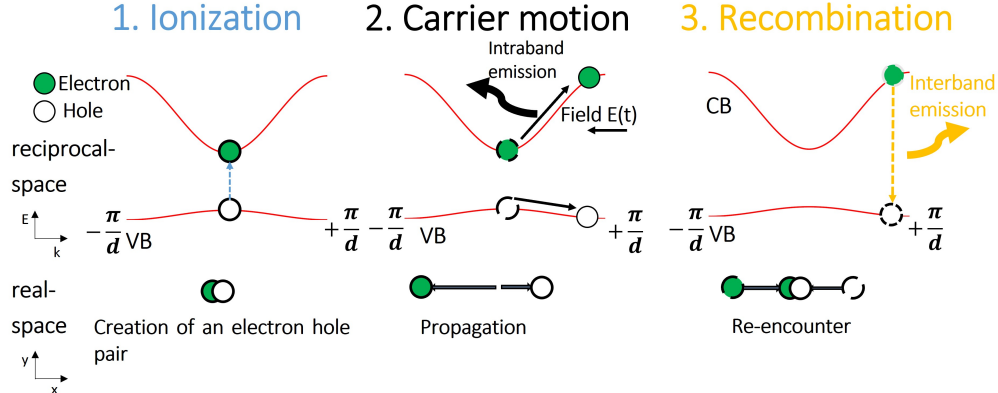
Figure 4.1: Schematic of three-step recollision model for solids.

It is possible to derive the three-step recollision model, which is illustrated in Fig. 4.1, from the general multi-band SBE. For our derivation we only consider one valence and one conduction band. The intraband acceleration of electrons and holes within their respective bands is described by the $\nabla_{\mathbf{k}}$ term. The $\nabla_{\mathbf{k}}$ term can be taken into account by defining a time-dependent crystal momentum which fulfills Bloch's acceleration theorem [3, 56]

$$
\mathbf{k}(t) = \mathbf{k}_0 - \frac{e}{\hbar} \underbrace{\int_{-\infty}^{t} \mathbf{E}(t')dt'}_{A(t)} .
$$

(4.1)

Consequently the SBE within a two-band model read

$$
\frac{\partial}{\partial t}p(\mathbf{k}(t)) = -\frac{i}{\hbar}\varepsilon_{vc}(\mathbf{k}(t))p(\mathbf{k}(t)) + \frac{i}{\hbar}\left(\boldsymbol{\mu}(\mathbf{k}(t))\right)^* \cdot \mathbf{E}(t)\left(1 - 2n(\mathbf{k}(t))\right) - \frac{p(\mathbf{k}(t))}{T_2},
$$
$$
\frac{\partial}{\partial t}n(\mathbf{k}(t)) = -\frac{i}{\hbar}\left(\boldsymbol{\mu}(\mathbf{k}(t))\right)^* \cdot \mathbf{E}(t)p(\mathbf{k}(t)) + c.c.
$$

(4.2)

Considering strongly nonresonant excitations within the low excitation regime no significant occupation in the conduction band occurs n_c ($n_v \approx 1$ and $n_c \approx 0$) justifying to use the Keldysh-Lewenstein approximation [155, 156] to decouple the eqs. (4.2). A formal integration of the polarization provide an insight of the HHG processes in solid-state

systems:

$$
p(\mathbf{k}, t) = exp\left(-\frac{i}{\hbar} \int_{-\infty}^{t} dt' \left[\varepsilon_{vc}(\mathbf{k} + \mathbf{A}(t) - \mathbf{A'}(t)) - \frac{1}{T_2} \right]\right)
$$
$$
\times \int_{-\infty}^{t} dt' \left[\frac{i}{\hbar} \boldsymbol{\mu}^*(\mathbf{k} + \mathbf{A}(t) - \mathbf{A'}(t)) \cdot \mathbf{E}(t') exp\left(\left(\frac{i}{\hbar} \int_{-\infty}^{t'} dt'' \left[\varepsilon_{vc}(\mathbf{k} + \mathbf{A}(t) - \mathbf{A'}(t)) + \frac{1}{T_2} \right] \right) \right) \right]
$$

Using $\boldsymbol{\kappa}_\tau = \mathbf{k} + A(t) - A(\tau)$ we get

$$
p(\mathbf{k}, t) = e^{-\frac{i}{\hbar} \int_{-\infty}^{t} \varepsilon_{vc}(\boldsymbol{\kappa}_\tau) d\tau} \int_{-\infty}^{t} dt' \frac{i}{\hbar} \boldsymbol{\mu}^*(\boldsymbol{\kappa}_{t'}) \cdot \mathbf{E}(t') e^{\frac{i}{\hbar} \int_{-\infty}^{t'} \varepsilon_{vc}(\boldsymbol{\kappa}_\tau) d\tau - \frac{(t-t')}{T_2}} .
$$

Introducing the classical action

$$
S(\mathbf{k}, t', t) = -\frac{i}{\hbar} \int_{-\infty}^{t} \varepsilon_{vc}(\boldsymbol{\kappa}_\tau) d\tau + \frac{i}{\hbar} \int_{-\infty}^{t'} \varepsilon_{vc}(\boldsymbol{\kappa}_\tau) d\tau = \int_{t}^{t'} \varepsilon_{vc}(\boldsymbol{\kappa}_\tau) d\tau,
$$

the polarization can be rewritten as

$$
p(\mathbf{k}, t) = \int_{-\infty}^{t} dt' \frac{i}{\hbar} \boldsymbol{\mu}^*(\boldsymbol{\kappa}_{t'}) \cdot \mathbf{E}(t') e^{\frac{i}{\hbar} S(\mathbf{k}, t', t) - \frac{(t-t')}{T_2}} .
$$

Similarly one can also derive an analytical relation for the occupation n within the Keldysh approximation:

$$
n(\mathbf{k}, t) = -\frac{1}{\hbar^2} \int_{-\infty}^{t} dt' \boldsymbol{\mu}^*(\boldsymbol{\kappa}_{t'}) \cdot \mathbf{E}(t') \int_{-\infty}^{t'} dt'' \boldsymbol{\mu}^*(\boldsymbol{\kappa}_{t''}) \cdot \mathbf{E}(t'') e^{\frac{i}{\hbar} S(\mathbf{k}, t'', t') - \frac{t'-t''}{T_2}} + c.c.
$$

The emitted signal in frequency domain during the recombination process from a photoexcited semiconductor depends on the macroscopic interband J_p and the intraband J_n

currents [157] and read within the present model

$$
\begin{aligned}
\mathbf{J}_p(\omega) &= \omega \int_{-\infty}^{\infty} dt e^{-i\omega t} \int_{\mathrm{BZ}} d^3 \mathbf{k} \boldsymbol{\mu}^*(\mathbf{k}) \\
&\times \int_{-\infty}^{t} dt' \frac{i}{\hbar} \boldsymbol{\mu}^*(\boldsymbol{\kappa}_{t'}) \cdot \mathbf{E}(t') e^{\frac{i}{\hbar} S(\mathbf{k},t',t) - \frac{(t-t')}{T_2}} + c.c., \\
\mathbf{J}_n(\omega) &= \sum_{m=v,c} -\frac{1}{\hbar} \int_{-\infty}^{\infty} dt e^{-i\omega t} \int_{\mathrm{BZ}} d^3 \mathbf{k} e \mathbf{v}_m(\mathbf{k}) \int_{-\infty}^{t} dt' \boldsymbol{\mu}(\boldsymbol{\kappa}_{t'}) \cdot \mathbf{E}(t') \\
&\times \int_{-\infty}^{t'} dt'' \boldsymbol{\mu}^*(\boldsymbol{\kappa}_{t''}) \cdot \mathbf{E}(t'') e^{\frac{i}{\hbar} S(\mathbf{k},t'',t') - \frac{(t'-t'')}{T_2}} + c.c,
\end{aligned}
\tag{4.3}
$$

whereas the group velocity is defined by $\mathbf{v}_m$. Two oscillatory terms are occurring in eq. (4.3) which depend on the electric field $\mathbf{E}(t)$ and on the band structure. Considering THz excitation conditions the laser frequencies $\omega_L \ll \omega_{cv}$ oscillate much slower. Using the so called saddle point method it is possible to derive equations approximating the integrals in (4.3) where the phase $i\Phi = \frac{i}{\hbar} S(\mathbf{k}, t', t) - i\omega t - \frac{t-t'}{T_2}$ is stationary [151, 157, 158]:

$$
\begin{aligned}
\frac{d\Phi}{dt'} &= \frac{1}{\hbar} \varepsilon_{vc}(\mathbf{k} - A(t') + A(t)) - \frac{i}{T_2} = 0, \\
\nabla_{\mathbf{k}} \Phi &= \int_{t}^{t'} \nabla_{\mathbf{k}} \varepsilon_{vc}(\mathbf{k} - A(\tau) + A(t)) d\tau = 0, \\
\frac{d\Phi}{dt} &= \frac{1}{\hbar} \varepsilon_{vc}(\mathbf{k}) - \omega + \frac{i}{T_2} = 0.
\end{aligned}
\tag{4.4}
$$

The derivative $\nabla_{\mathbf{k}} \varepsilon_{vc}(\mathbf{k}) = v_c - v_v$ defines the difference of the group velocities of the particles within their respective bands. A physical picture of electron-hole recollision can be established based on saddle-point equations (4.4).

The first condition $\varepsilon_{vc}(\mathbf{k} - A(t') + A(t)) = 0$ describes the interband excitation due to a strong electric field creating an electron-hole pair [158]. Within a two-band model the following relation is provided:

$$
\varepsilon_{vc} \geq \varepsilon_{\mathrm{gap}} + h(\mathbf{k}) \text{ with } h(\mathbf{k}) \geq 0
$$

Since $\varepsilon_{vc} \geq \varepsilon_{\mathrm{gap}} \geq 0$ the first condition can only be fulfilled for a ionization time t' which is complex. Recently, analogous to the atomic case [4, 159, 160], the influence of the dynamics of the tunneling process in solid-state HHG was revealed by considering an imaginary of ionization time [161]. It is demonstrated that the properties of electrons at the tunneling exit as a result of the motion in the classically forbidden region are crucial for predicting the subsequent dynamics, especially the emission time [161]. However, here the dynamics

of the tunneling process has been ignored by zeroing the band gap energy in the first equation of (4.4) because we use the electron-hole recollision model proposed in [154] which provides intuitive insights into the dynamics of solid-state HHG. While the saddle-point approach given in Ref. [157] is less accurate in predicting subcycle dynamics, it remains suitable for interpreting the anisotropy of high-harmonic generation (HHG) in MgO [147]. Therefore, in the following analysis, we examine the orientation dependence of HHG without resorting to complex solutions of equation (4.4), utilizing the saddle-point approach as presented in Ref. [157].

The second condition $\nabla_{\mathbf{k}}\Phi = \Delta\mathbf{x}_c - \Delta\mathbf{x}_v = 0$ in (4.4) describes the re-encounter process of an electron with its respective hole. The classical trajectory is obtained by the propagation distance $\Delta\mathbf{x}_\lambda = \int_{t'}^{t} \mathbf{v}_\lambda d\tau = \mathbf{x}_\lambda(t) - \mathbf{x}_\lambda(t')$ after creating an electron-hole pair.

The third condition in eq. (4.4) determines the photon energy during the recombination between the electron with its corresponding hole. It depends on the bandgap energy at the associated $\mathbf{k}$ position in momentum space. The maximum difference between conduction and valence band energies determines the so called cutoff energy (highest harmonic energy). In the following work we assume a creation of an electron-hole pair at the Γ point ($\mathbf{k} = 0$) to calculate the classical trajectories because they contribute strongly to the interband emission.

The nonlinear HHG spectra in the presence of a strong optical attosecond pulse that are presented and analyzed here for solid MgO are obtained by numerical solutions of the SBE including interband transitions and intraband acceleration within a two-band model in the time domain and by subsequent Fourier/wavelet transforms [81, 83, 151]. The classical trajectories of electrons and holes are calculated by solving the saddle point equations in the classical approximations [151, 152].

4.2 Orientation-dependent high harmonic generation

Our theoretical investigation starts with the crystal-orientation-dependent HHG observed in MgO to unravel the sub-cycle collision dynamics. The considered solid-state system is driven by an intense linearly-polarized optical attosecond pulse with a wavelength of 1.3 μm and a peak field amplitude of 12 V/nm. The temporal envelope of the electric field are described by a Gaussian function (2.20) with a full-width at half-maximum (FWHM) equal to half the optical cycle T_0. Consequently, we restrict our analysis of all excitations within one laser cycle (see blue dashed line in Fig. 4.3). To control electrons in solids and monitor the nonlinear response of bound electrons, similar laser pulses have been successfully employed in a range of spectral regions including THz, mid-infrared, visible, and nearby wavelengths [162–164].[1] Consequently, it becomes possible to track the complete dynamics of electron-hole collisions, thereby providing a means to test the existing collision models.

---

[1]A complete confinement of the energy to a half wave cycle is a property of an optical attosecond pulse [163].

In our theoretical treatment the angle Θ between the polarization direction of the incident pulses and the bonding of Mg and O atoms of the material is defined as in [147]. Using the density functional theory (DFT) software package from ELK [165] the energy dispersion of the highest valence band and the first conduction band is obtained. Applying the twisted parallel transport gauge on the calculated eigenfunctions smooth transition dipole matrix elements in momentum space are obtained [166–168]. In the case of bulk MgO the dipole matrix elements are purely imaginary quantities (the real parts are almost zero) which imply the non-broken symmetry of lattice structure of MgO. The relative phases are either zero or π leading to a non existing Berry phase which is also demonstrated in [168].
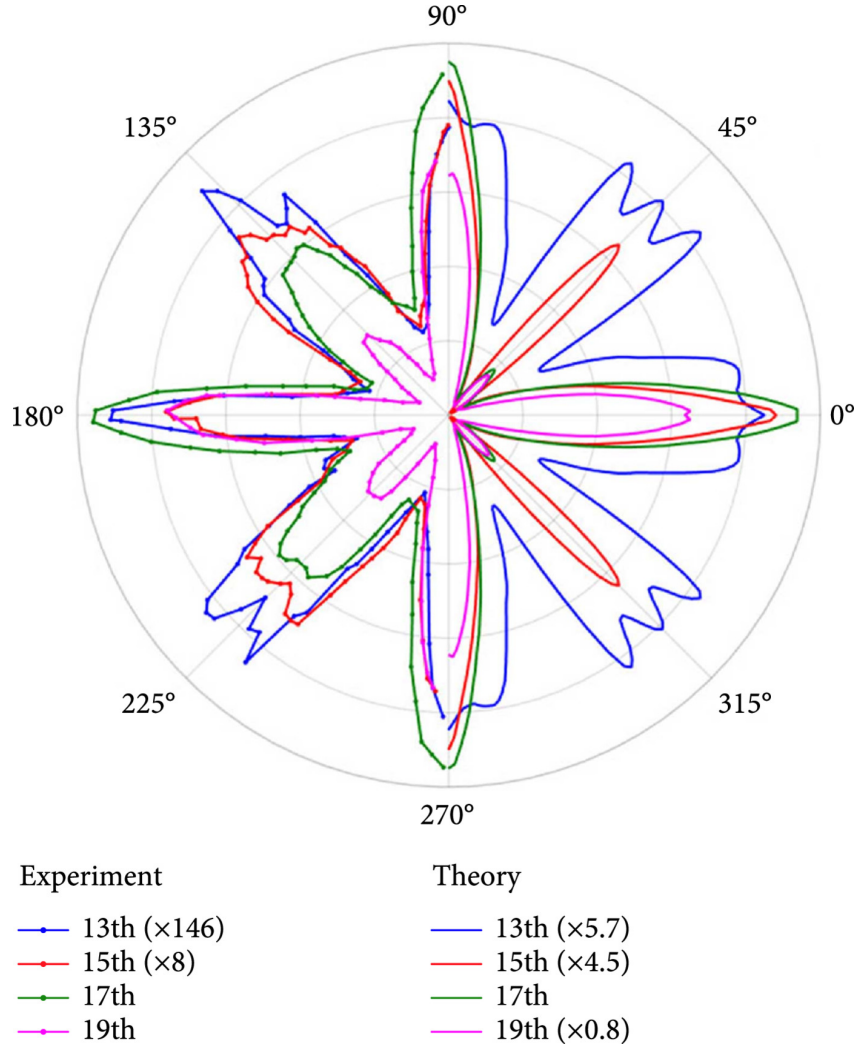
Figure 4.2: The experimental data (left half of the circle) are obtained from [147]. The calculated HHG based on the numerical solutions of the SBE are also shown for MgO (right half of the circle). Taken from [154].

In Fig. 4.2 a comparison between an experiment [147] and our theoretical findings of the HHG emission for MgO is shown. In this case the calculated interband polarization based on full quantum simulations solving the SBE, see eq. (4.2). The results show clearly a four-fold symmetry of the obtained HHG with both enhanced as well as diminished emission depending on the polarization direction of the incident pulses. This kind of anisotropy confirms the fact that the dynamics is probably connected within the subcycle time scale.

In the following, we explicitly investigate the origin of high-harmonic generation (HHG) observed in the plateau region. Firstly, we analyze the time-dependent interband current, which constitutes the dominant contribution within the spectral region of interest for HHG in MgO. We accomplish this by applying a wavelet transformation [169]. The time-frequency analysis for $\Theta = 0°$, $\Theta = 27°$, and $\Theta = 45°$ is shown in Fig. 4.3(a)-(c), respectively. Along the nearest-neighbor direction $\langle 100 \rangle$ (Mg-O) corresponding to $\Theta = 0°$ two emission bursts occur. One of them is located at the high energy part around the maximum energy gap (denoted by "1") and the other one is located at lower energy part (denoted by "2").
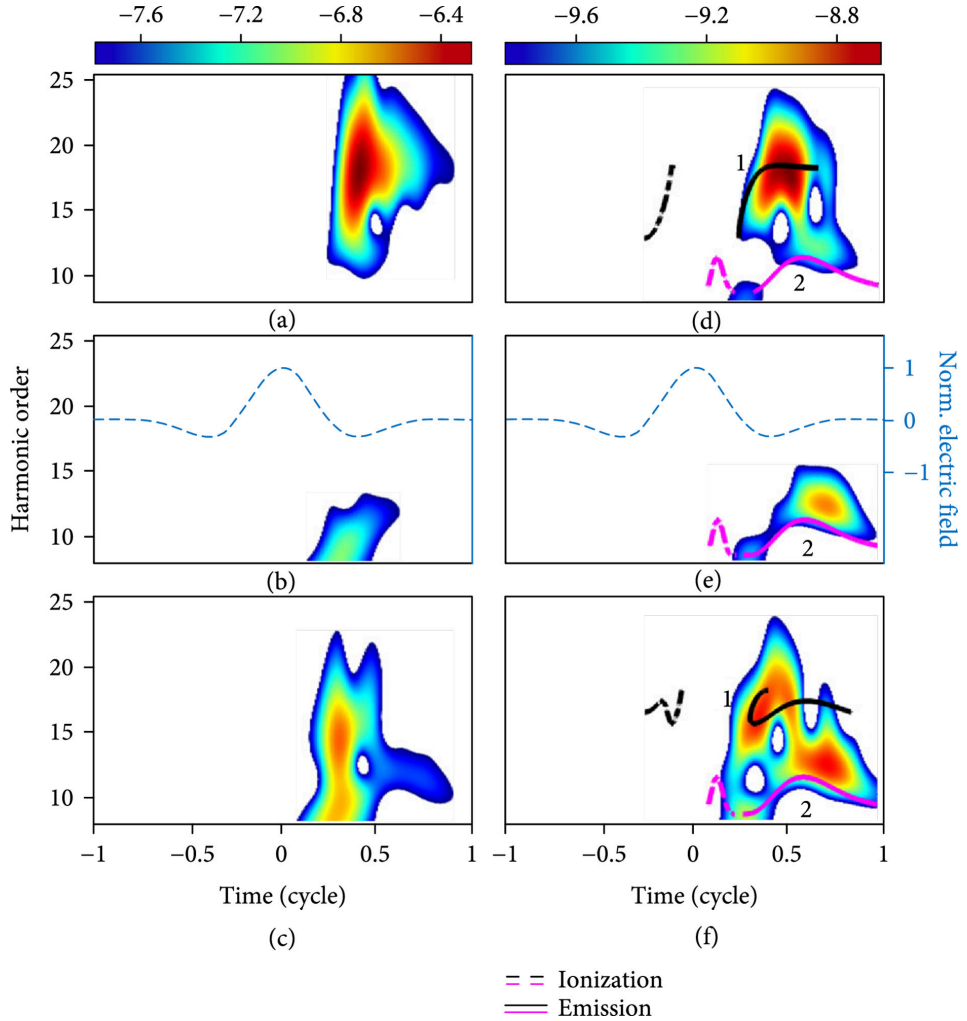
Figure 4.3: In (a)-(c) the time-frequency analysis of interband HHG based on the numerical solutions of SBE (4.2) is shown. In (d)-(f) we show the corresponding results based on the semiclassical recollision model considering only electron trajectories excited around the Γ-point. Moreover the solid lines denote the recombination of emitted harmonic energy depending when the ionization occurs (dashed lines). The magnitudes are shown on a logarithmic scale. In (b) and (e) the temporal envelope of the electric field is shown displayed by the blue dashed lines. Taken from [154].

For $\Theta = 27°$, see Fig. 4.3(b), the emission burst "1" completely disappears. Along the nearest neighbor direction $\langle 110 \rangle$ between two Mg atoms $\Theta = 45°$ (see Fig. 4.3(c)), the emission burst "1" still remains visible but is much weaker than for $\Theta = 0°$. In contrast, the strength of emission "2" does not change at all for these cases. These theoretical findings show the dependence on the polarization angle and exhibit a good qualitative agreement with the experimental data presented in Fig. 4.2 and discussed in [147, 170]. The experimental

observations reveal that the high-energy portions of the harmonics are strongest along $\Theta = 0°$, slightly weaker along $\Theta = 45°$, and significantly weaker around $\Theta = 27°$. In contrast, the lower energy harmonics exhibit comparable intensities for $\Theta = 0°$ and $\Theta = 45°$. In [147] the anisotropy of the interband HHG has been related to whether the electron trajectory connects or avoid neighboring atomic sites. However, we demonstrate that the re-encounter between the electron with its left-behind hole is crucial for an enhanced or diminished HHG emission.

Using the same excitation conditions as in the full quantum simulations we analyze the trajectories of electrons and holes obtained from the semiclassical re-collision model. In Figs. 4.3(d)-(f) the emitted photon energy (solid lines) which correspond to the energy difference of the electron-hole pair at the momentum where they re-encounter with each other is shown. The re-encounter depends when the ionization (dashed lines) has happened. Similarly, there are two possible electron-hole recombination trajectories obtained for $\Theta = 0°$, see Fig. 4.3(d). The emission "1" is originated when the ionization starts before the maximum field crest. The other emission burst corresponds to the case when the electron-hole pair is created after the maximum peak of the electric field. The short trajectory branch reproduces well the emission "2" from the full quantum calculation, see Fig. 4.3(a). Due to $T_2 = T_0/4$ longer trajectories at larger times are not possible [152]. This agreement between the quantum and classical simulations justifies the validity of the recombination model of an electron with its associated hole and not with another one which is not related [147, 171].

The Figs. 4.4-4.6 depict the propagation of the electron in real and momentum space at three different time points after the creation of an electron-hole pair.
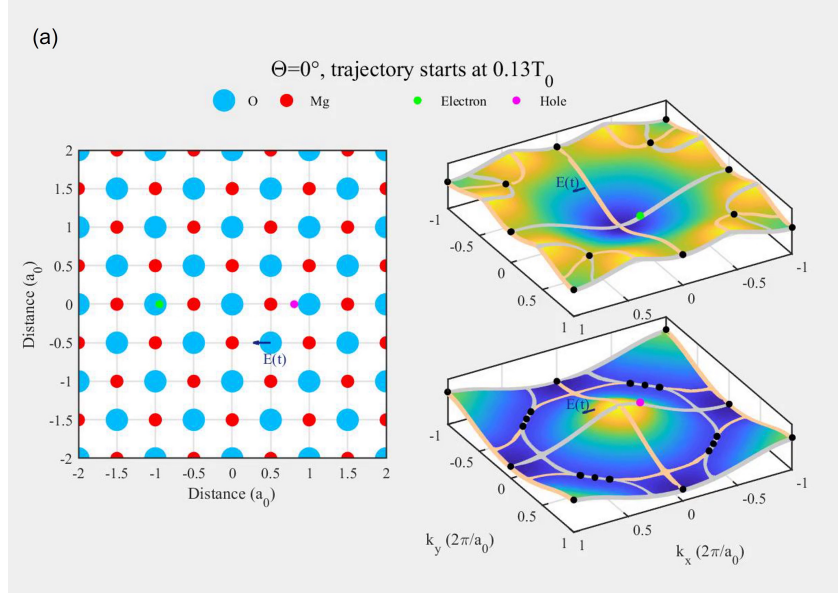
Figure 4.4: The electron-hole pair is created at the Γ-point. The electron and its parent hole are accelerated within a small region of the Brillouin zone. Due to a sign change of the electric field the direction of carrier motion in momentum space is reversed. Taken from [154].
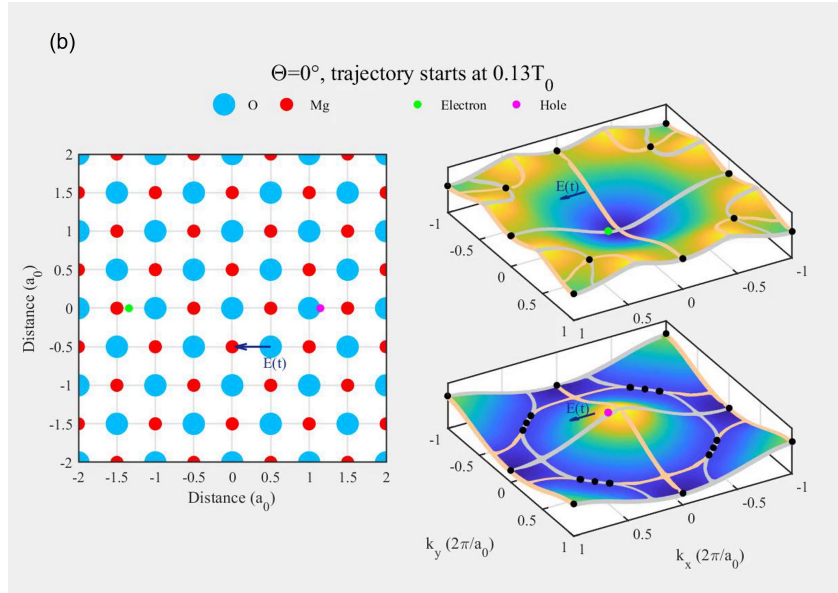
Figure 4.5: When the electron and the hole passes the Γ-point their direction in real space is immediately reversed. Taken from [154].
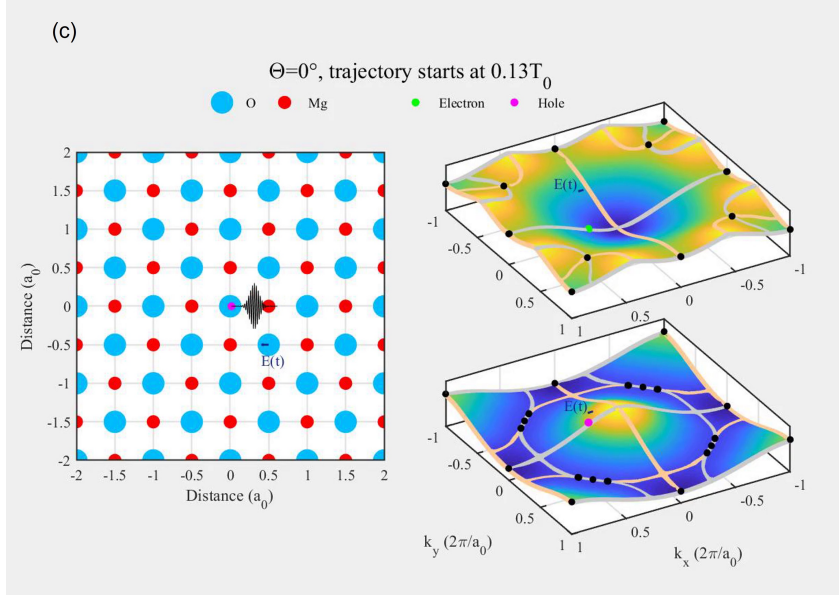
Figure 4.6: The re-encounter between the electron and its corresponding hole occurs when they meet each other in real space. Taken from [154].

Although several atomic sites appear no scattering processes occur for emission "1". Both the electron and its associated hole are driven back when the laser field changes its sign, see Fig. 4.4. Due to this fact the electron and the hole passes the critical point at Γ providing a reversal of the propagation direction in real space, see Fig. 4.5. Consequently, a re-encounter between the two particles appears before the electric field changes its sign again (see. Fig. 4.6). This entire process describes exactly the case in atomic HHG. For the considered excitation conditions one can indicate that the electron-hole pair is only propagating within a small region around the Γ-point. This provides a small wave number of the electron which is the main reason that scattering processes with neighboring atoms are absent [172]. The above described process is predominately responsible for the atomic-like behavior of HHG in ZnO [49]. Here, we find that it also exists in solid MgO and explains the very weak orientation dependence of the low energy part of HHG, see Figs. 4.3(a)-(c).

## 4.3 Collision-assisted electron-hole recombination

When the electron-hole pair is generated before the field maximum and the electric field is strong enough such that the electron can be driven far away from the Γ-point, the wave number of the electron may get large enough that scattering with other atomic sites becomes relevant [172]. The possible scattering mechanisms are schematically shown in Fig. 4.7.
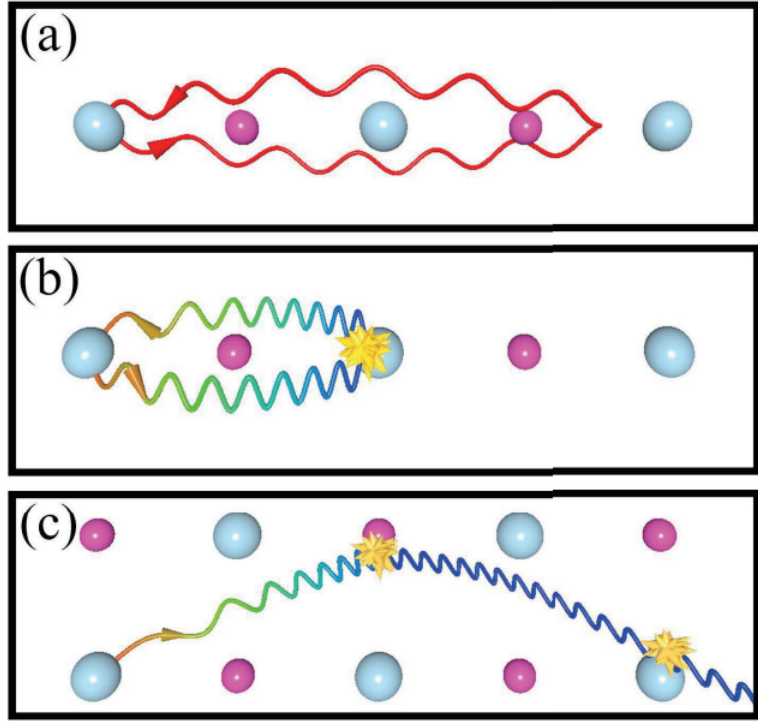
Figure 4.7: In (a) the usual recombination process known from atomic HHG is shown. It describes a reversal of the propagation direction due to a sign change of the laser pulse. In (b) backward scattering processes with other atoms due to a larger wave number is shown. In (c) forward scattering processes for oblique angle are shown. The atoms are displayed as blue spheres for oxygen and magenta spheres for magnesium atoms, respectively. The different wave numbers are indicated with different colors increasing from red to blue. Taken from [54].

The propagation of electrons and holes depends on the band structure which includes the periodic potential and thus contains the information of electron/hole collisions with neighboring atoms. For the considered energy dispersion some critical points where $\nabla_{\mathbf{k}} \varepsilon_{c,v}(\mathbf{k}) = 0$ (indicated by the black dots) and critical lines (indicated by grey/yellow solid lines) where the gradient along only one direction vanishes, i.e, $\nabla_{k_x} \varepsilon_{c,v}(\mathbf{k}) = 0$ or $\nabla_{k_y} \varepsilon_{c,v}(\mathbf{k}) = 0$, exist, as shown in Fig. 4.8(a) for the lowest conduction band. We observe that the collision and scattering information of electrons with other atomic sites can be directly extracted from the dynamics in momentum space, particularly when the electrons or holes traverse these critical points and lines.
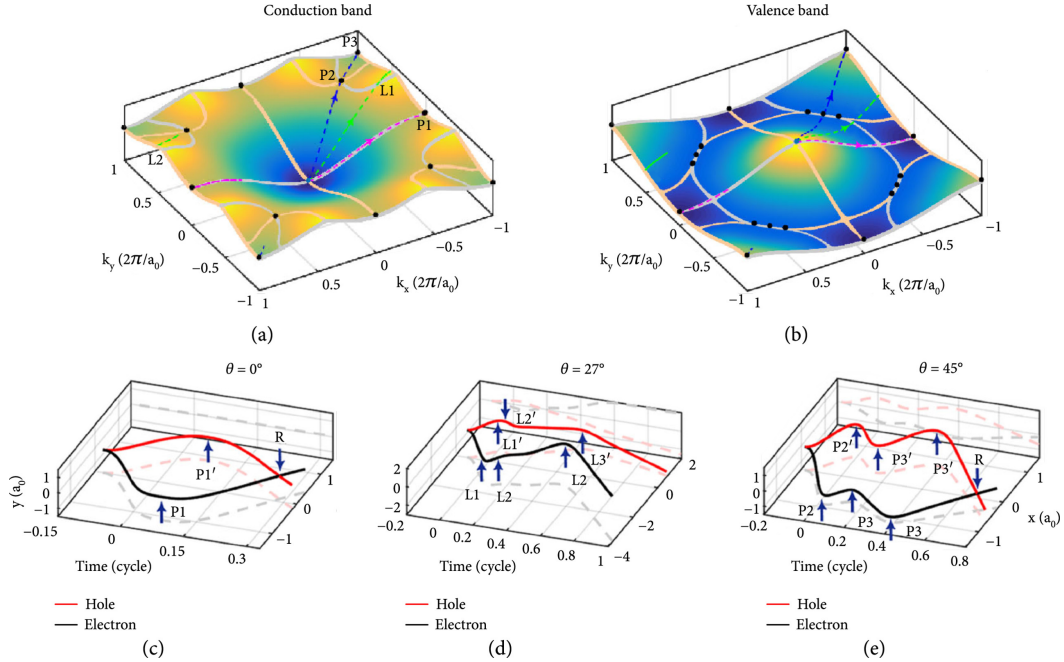
Figure 4.8: Mapping between the real space trajectories and the movement of the electrons/holes in momentum space. In (a) and (b) the considered valence band and conduction band of MgO are shown, respectively. Here, the critical points are indicated as black dots and the critical lines as yellow/grey solid lines. In (c)–(e) we consider the case when ionization appears before the field crest at $t = -0,13T_0$ for $\Theta = 0°$, $\Theta = 27°$ and $\Theta = 45°$. The related propagation distances are shown as deep pink ($\Theta = 0°$), green ($\Theta = 27°$), and blue ($\Theta = 45°$) dashed arrow lines in (a) and (b). Taken from [154].

In Fig. 4.8(c) the time-dependent position of an electron-hole pair born at $t_0 = -0,13T_0$ for $\Theta = 0°$ is shown. Here, the direction reversal of the electron-hole pair occurs at $t = 0,08T_0$ whereas the sign change of the electric field occurs at $t = 0,25T_0$. The direction reversal takes place when in momentum space the electron reaches the critical point "P1" at the boundary of the Brillouin zone. Then it jumps to the point "P1" on the opposite side, see Fig. 4.8(a). Therefore, the Bragg scattering is responsible for the recombination of the electron and its associated hole (indicated by the arrow denoted with "R" in Fig. 4.8(c)). We denote this HHG emission mechanism as "collision-assisted electron-hole recombination".

Unlike for $\Theta = 0°$ orientation, there are two critical points in the conduction band along the $\Theta = 45°$ orientation which are denoted as "$P2'$" and "$P3'$" in Fig. 4.8(a). The electron-hole pair is created before the maximum field crest of the electric field. Therefor, the electron would experience several head-on collisions with the nearest (located at $-0,5a_0$ along x direction) and second-nearest O atoms (located at $-a_0$ along x direction) before it re-encounters with its associated hole, see Fig. 4.8(e). Each head-on collision in real space corresponds to the passage of the electron through one of the critical points in momentum space. This can be observed by referring to the blue dashed line in Fig. 4.8(a) and the instances indicated by the blue arrows in Fig. 4.8(e). Due to multiple scatterings, the time

delay between the ionization and recombination is larger than that for $\Theta = 0°$ orientation. Moreover, the emission mainly occurs at the high energy part located between these two critical points (describing the ionization and emission curves from "1" in Fig. 4.3(f)). Within the classical simulation dephasing is not included, whereas rapid dephasing is present in quantum simulation. Hence, very long returning trajectories of the classical calculations do not contribute to HHG since the electron would be attenuated before re-encounter, which explains the weaker HHG signal along $\Theta = 45°$ orientation than that along $\Theta = 0°$ in the quantum calculation, see Figs. 4.3(a) and 4.3(c). In the valence band, there are also two critical points, as shown in Fig. 4.8(b). Therefore, multiple scattering events also occur for the hole. The electron and its associated hole meet near the atomic site where they were initially created, as depicted by the point "R" in Fig. 4.8(e).

4.4 Control of high harmonic generation by two-color excitation

The connection of different ionization times with different recombination mechanisms contributing to HHG greatly facilitates the all-optical control of the collision dynamics. In Fig. 4.9 the time-frequency analysis of HHG driven by two-color electric fields with different relative phases is shown. The two-color laser field consists of two parallel-polarized fields, namely the fundamental field and its second harmonic field. The duration of the second harmonic field is also equal to half the optical cycle T_0 of the harmonic field. The relative phase between these two components is defined as the carrier-envelope phase of the second harmonic field. The two-color field used in the calculations presented in Fig. 4.9 can be expressed as follows:

$$E(t) = [E_1 \cos(\omega_1 t) + E_2 \cos(\omega_2 t + \varphi)] f(t) \tag{4.5}$$

Here, E_1 and E_2 are the electric field amplitudes and φ is the relative phase of the two-color fields. The single-color field corresponds to the case when $E_2 = 0$ and was applied in Fig. 4.3(a). The envelope $f(t)$ is describe by a Gaussian function (2.20) with a FWHM equal to half the optical cycle. For the two-color field we use a rather weak amplitude $E_2 = 0, 25 E_1$. By choosing particular relative phases we can control the waveform of the electric field and selectively enhance the field amplitude before or after the peak of single color field, see Figs. 4.9(c) and (d). Consequently, the two emission channels can be selectively enhanced, see Figs. 4.9(a) and (b). Thus, one can clearly control whether or not the electron collides with other atomic sites in the periodic potential within sub-cycle timescales which provides a novel path for designing extreme ultrafast photoelectric devices.
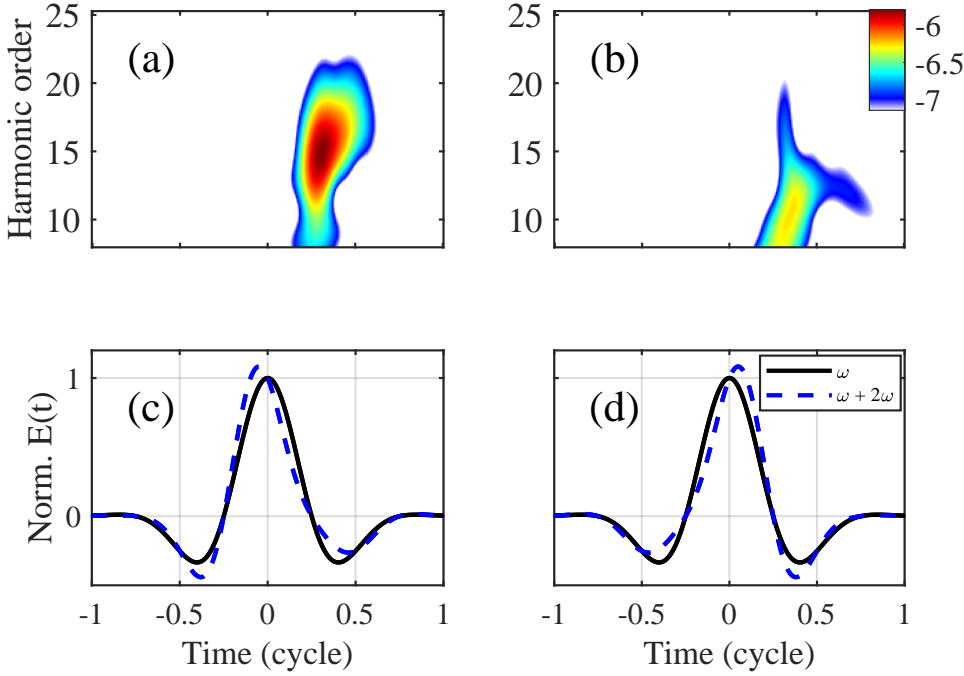
Figure 4.9: The time-energy distribution of HHG (a)-(b) and the corresponding driving electric field (c)-(d) for two-color fields with $\varphi = 0, 5\pi$ and with $\varphi = -0, 5\pi$ that are polarized in the $\Theta = 45°$ direction (dashed line). The waveform of the single-color field is also shown by the solid line in (c) and (d) for comparison. Taken from [54].

4.5 Conclusions

In this chapter, we present a comprehensive approach to understand the interband HHG in solid-state systems. The approach establishes a connection between the scattering processes occurring in real space and the band structure of the system. Specifically, when an electric field induces the creation of liberated electrons and they move within a small fraction of the Brillouin zone near the Γ-point, no scattering with neighboring atoms occur. In such cases, the behavior is similar to atomic HHG, where the direction of particles changes when the electric field changes its sign, resulting in a weak anisotropy of the interband HHG.

However, when the electron and its associated hole can reach larger k-points in momentum space, their wavelengths correspond to the order of the lattice constant. This provides the possibility of collisions with neighboring atoms of the considered crystal in real space. The proposed approach establishes how these collision processes can be indicated in the corresponding band structures. Head-on collisions occur on van-Hove singularities in momentum space $\nabla_{\mathbf{k}}(\varepsilon_{c,v}(\mathbf{k})) = 0$, which are responsible for possible backward scattering mechanisms that reverse the direction of the particles during their propagation. Conse-

quently, the recombination between an electron with its associated hole is provided without a sign change from the laser field. This mechanism is a new physical interpretation that explains the difference between solid HHG and atomic HHG. Besides critical points, side collisions occur when the particles move through critical lines where only the derivative along one direction $\nabla_{k_x}\varepsilon(\mathbf{k}) = 0$ or $\nabla_{k_y}\varepsilon(\mathbf{k}) = 0$ is zero.

Overall, the presented theoretical model and the resulting findings provide a new insight into HHG in solid-state systems, which have been previously investigated in experiments and by other theoretical approaches [49, 147, 170, 173].

High harmonic generation with excitons

5

So far, we have focused on nonlinear processes without considering many-body interactions. In this chapter, we solve the SBE within a one-dimensional (1D) two-band tight-binding model. However, we extend the SBE by considering purely excitonic effects [54]. The Coulomb interaction will be treated in the TDHF approximation, as derived in chapter 2.2. By doing so, we demonstrate that the intensity of the higher harmonics originating from the interband current can be significantly enhanced by a specific choice of excitation pulses. Our theoretical results, presented in this chapter, were published in [54]. These theoretical findings highlights the importance of excitonic effects of HHG and their potential for enhancing the efficiency of nonlinear optical processes in semiconductors.

5.1 Enhancement of HHG by excitonic resonances

The many-body Coulomb interaction including excitonic effects is treated in the TDHF approximation. Considering eq. (2.12) the SBE in one dimension read [2, 85, 174]

$$
\begin{aligned}
\frac{d}{dt} p_k &= -\frac{i}{\hbar} \tilde{\varepsilon}_k^{cv} + i \left(1 - 2n_k\right) \Omega_R + \frac{e}{\hbar} E(t) \nabla_k p_k - \frac{p_k}{T_2}, \\
\frac{d}{dt} n_k &= -2\mathrm{Im}\left[\Omega_R p_k^*\right] + \frac{e}{\hbar} E(t) \nabla_k n_k,
\end{aligned}
\tag{5.1}
$$

with the generalized Rabi frequency

$$
\Omega_{R,k} = \frac{1}{\hbar} \left[E(t)\mu_k + \sum_{q \neq k} V_{k-q} p_q \right]
\tag{5.2}
$$

and the renormalized transition energy $\tilde{\varepsilon}_k^{cv}$

$$
\tilde{\varepsilon}_k^{cv} = \varepsilon_k^{cv} - 2 \sum_{q \neq k} V_{k-q} n_q,
\tag{5.3}
$$

whereas the transition energy ε_k^{cv} considering a tight-binding model reads

$$\varepsilon_k^{cv} = \hbar\omega_{\text{gap}} + \frac{\Delta}{2}\left(1 - \cos(ka)\right), \tag{5.4}$$

with $\hbar\omega_{\text{gap}}$ as the band gap energy. The total bandwidth of the energy dispersion is given by Δ. In first-order $k \cdot p$ theory the dipole matrix elements in momentum space read [85]

$$\mu_k = \mu_0 \frac{\omega_{\text{gap}}}{\varepsilon_k^{cv}}. \tag{5.5}$$

Here, our 1D model is applied to a quantum wire configuration with length scale R which defines the strength of the parabolic confinement. Thus, the Coulomb matrix elements V_q are given by [175]

$$V_q = \frac{\pi}{L}\sqrt{\frac{1}{2|q|R}}e^{-|q|\frac{4}{\pi}R}. \tag{5.6}$$

For the numerical solutions of (5.1) we consider Gaussian shaped electric fields $E(t) = E_0 e^{-\frac{2ln(2)t^2}{\tau^2}} \cos(\omega_L t)$ with $\tau = 10\frac{2\pi}{\omega_L}$ as the pulse duration including 10 laser cycles and ω_L as the laser frequency. We use material parameters which are close to GaAs [83, 85], i.e., $\hbar\omega_{\text{gap}} = 1.43$ eV, $\Delta = 1$ eV, $a = 0.565$ nm, $\mu_0 = 0.3$ nm, and the dephasing time $T_2 = 50$ fs.

In Fig. 5.1(a) we show the comparison of the linear absorption spectrum considering the cases without Coulomb interaction and including excitons. Without the consideration of excitonic effects an absorption peak firstly arises as expected around the band gap energy at 1.43 eV. Due to the dephasing this van Hove peak is broadened. The linear absorption ends (not shown here) with a second van Hove peak around 2.43 eV. In contrast to free carriers, a strong 1s exciton absorption peak appears at approximately 1.15 eV when including the Coulomb interaction. Moreover, more exciton transition peaks are obtained below the band gap whereas the absorption above it is much reduced. The strength of the Coulomb interaction is chosen in such a way that the resulting binding energy of the 1s exciton corresponds to 280 meV. Such a large binding energy energy exceeds clearly what can be observed in GaAs-based bulk semiconductors. However, such energies are realized in two-dimensional materials like transition metal dichalcogenides (TMDC). Only recently the theoretical analysis of the Coulomb enhancement of HHG in such materials has been provided [55]. The Coulomb enhancement of the HHG is shown in Fig. 5.1(b) and (c). Firstly, we choose a central laser frequency of about 385 meV which corresponds to a third of the 1s exciton resonance. In this case the third order harmonic is mainly enhanced by several orders. Similarly, for $\omega_L = 165$ meV a strong enhancement is determined for the
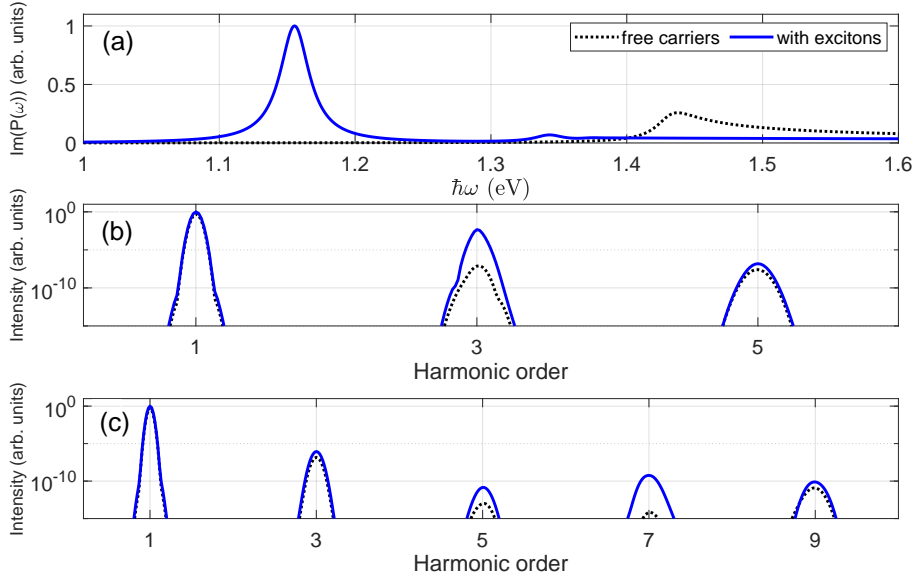
Figure 5.1: In (a) the linear absorption spectrum without (dotted black) and with excitonic transition peaks (solid blue) is shown. The obtained binding energy from the 1s exciton is about 280 meV. In (b)-(c) we show the Coulomb enhancement of HHG considering laser frequencies corresponding to ω_L = 385 meV (b) and ω_L = 165 meV (c), respectively. The maximal electric field strength is 1 MV/cm. Taken from [54].

seventh harmonic as can be seen in Fig. 5.1(c). In principle, we can summarize that the enhancement of certain harmonics can be controlled by choosing the laser frequency of the incident fields to an odd multi-photon energy corresponding to the 1s exciton resonance. This kind of enhancement can be physically understood by taking into account that the excitonic transition peaks provide more interband excitation pathways for HHG. These kind of polarization couplings have been also investigated in [176] whereas additional transitions between valence bands also lead to enhancements of HHG.

5.2 Conclusions

Over the past decade, there have been significant theoretical investigations into the influence of many-body Coulomb interactions. In these investigations, researchers have primarily applied optical fields with high intensities, which provide Rabi frequencies that exceed the binding energy of typical III-V semiconductors [78]. However, such semiconductor nanostructures have only binding energies around a few meV, i.e., due to screening. Furthermore, complete ionization of the exciton induced by such strong pulses has no significant influence on the nonlinear response originating from Coulomb interactions.

In contrast, TDMCs exhibit strong excitonic resonances with binding energies corresponding to several hundreds of meV [55, 177, 178]. In this chapter, we have demonstrated the importance of excitonic effects when the Rabi frequency is in the order or below the binding energy of excitons by considering weak nonresonant laser pulses.

Within our 1D tight-binding model, we were able to provide a direct connection between the excitonic resonances and the applied laser pulses. By selecting suitable laser frequencies depending on the binding energy of the considered material system, precisely selected harmonics can be enhanced.

These theoretical findings, presented in the reference [54], were likely the reason for further theoretical investigations in this research area [55]. It is important to continue studying the influence of many-body Coulomb interaction on the nonlinear response of various material systems under different excitation conditions to advance our understanding of this phenomenon.

Analysis of many-body Coulomb correlations in the excitonic nonlinear optical response

<div style="text-align:right">**6**</div>

The optical response of near-bandgap semiconductors is influenced by the interaction between light and the resonant or near-resonant material polarization. This interaction leads to the excitation of carriers, such as electron-hole pairs, and the emergence of transient coherent nonlinearities. To understand these effects at a microscopic level, it is necessary to analyze the relevant quasiparticles and their interactions. In this chapter, we specifically focus on the interactions between carriers, namely the many-body Coulomb correlations, and how they influence the optical nonlinearities of semiconductor nanostructures. Many experimental observations and comparisons with theoretical investigations on the nonlinear response of excitons (X) in spatially-homogeneous type-I QW nanostructures have been performed in the past [57, 58, 60–63, 73, 179–184]. As mentioned in chapter 2.2 a hierarchy problem appears when deriving the equations of motion for the microscopic polarization p when the many-body Coulomb interaction is taken into account. Here, p indicates the single-exciton amplitude as shown schematically in Fig. 6.1.
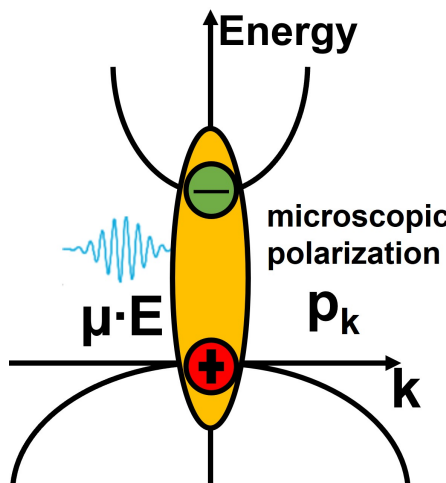

Figure 6.1: Schematic of the interband coherence between holes and electrons induced by a laser field.

An exact theoretical treatment of this many-body problem is only achievable for very small systems with only a few sites [185–187]. In our case it is necessary to derive an approximate closed set of equations. One possibility is the TDHF approximation. Here, a factorization as described in chapter 2.2 of all a four-point operators into products of two-point operators is performed [2, 109] which provides a theoretical description of the interband coherences and the populations. The TDHF approximation is already able to describe some many-body features, i.e., finite FWM signals for negative delay times [16, 17, 73, 182, 183, 188] which are absent if Pauli-Blocking is the only considered nonlinearity. Over time, due to better experimental techniques the sample quality of semiconductor nanostructures has been improved. At the same time, theoretical descriptions of many-body Coulomb correlation effects on a microscopic level have also evolved. In ultrafast spectroscopy experiments performed with certain polarization directions and for low intensities it was demonstrated that higher-order correlations such as excitation-induced dephasing [58, 113, 189–191] and the existence of bound biexciton resonances [33, 57, 63, 116–118, 192–203] have a major impact on the nonlinear optical response.

In our theoretical approach we restrict the appearing higher-order correlation functions up to a certain order in the optical field. Regarding FWM and PP experiments it is at least necessary to analyze the nonlinear optical response up to the third order in the electric field ($\chi^{(3)}$). In the coherent $\chi^{(3)}$-limit it is possible to derive dynamic equations for the single-exciton amplitude p and the two-exciton amplitude B which fully describe the interactions of the photoexcited electron-hole pairs [61, 62, 179]. Due to the fact that numerical evaluations of considering many-body correlations are quite demanding we use an one-dimensional (1D) model which in many cases provides qualitatively similar results in the vicinity of the exciton resonance as two-dimensional models systems, e.g., QWs [57, 186]. As mentioned before our theoretical approach was widely used in the past to describe spatially-direct type-I QW structures as shown in Fig. 6.2 (left). We extend our theoretical treatment in order describe so-called charge transfer excitons (CTX). The CTX may appear in spatially-indirect type-II QW structures which have been investigated recently, see. Fig. 6.2 (right), experimentally [204–206].

Type-I quantum well structure   Type-II quantum well structure
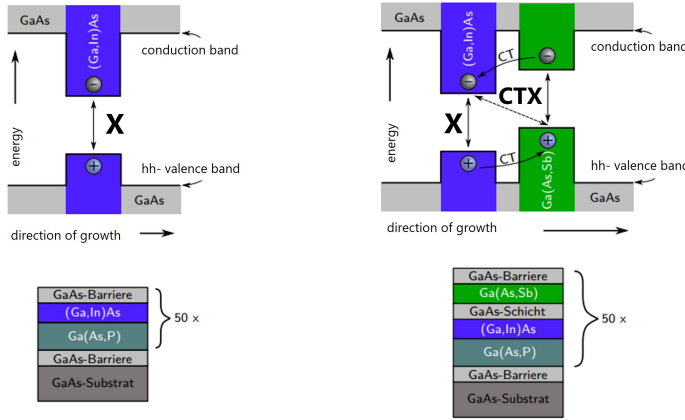
Figure 6.2: Comparison between a spatially-direct type-I QW and a spatially-indirect type-II QW structure. The reference sample (left) consists of 50 individual (Ga,In)As quantum wells surrounded by GaAs barriers. It provides a spatially direct transition (solid arrow) within the (Ga,In)As quantum wells. The type-II heterostructure (right) consists of 50 consecutive quantum well units. These are composed from two different quantum wells, which are spatially separated from each other by thin GaAs layers from each other. Due to this fact and the attraction between spatially separated electrons and holes a so-called CTX exist describing the lowest interband transition in such type-II heterostructures. Taken from [206]

6.1 Experimental setup to study the excitonic nonlinear response of type-I/II quantum wells

In the following the experimental setup of a PP experiment performed on spatially-direct type-I and especially on spatially-indirect type-II QW structures is introduced. The excitonic nonlinear response is measured for co-circularly and for counter-circularly polarized excitation conditions.

The type-I QW structure which is shown in Fig. 6.2 (left) consists of multiple QWs with 50 separate $Ga_{0.942}In_{0.058}As$ layers. Every single 7.7 nm thick quantum layer is surrounded by GaAs barrier layers. During the epitaxial waxing and because of different lattice constants of the individual materials epitaxial strain occurs. Consequently, energy shifts of the valence and conduction bands induced by lattice mismatches exist. This influence on the band structure of electrons and holes is directly reflected in effective masses [207] and also affect the exciton binding energy [208]. The degeneracy of light holes (lh) and heavy holes (hh) at the Γ-point is absent [209] providing two separate 1s lh- and hh-exciton resonances, i.e., in the linear absorption spectrum. For our theoretical investigations we only consider hh-excitons since the laser pulses are tuned to the hh-excitons or slightly below in the experiments and the absorption at the lh-exciton resonance is reduced due to

smaller oscillator strength. Furthermore, oppositely strained Ga(As,P)-barriers between the quantum layers are used in order to reduce strain-induced defects in the QW structure.

The spatially-indirect type-II QW sample illustrated in Fig. 6.2 (right) is also based of 50 multiple thin QWs of 7.7 nm thick $Ga_{0.942}In_{0.058}As$ and 7.5 nm $GaAs_{0.93}Sb_{0.07}$ layers. Between them a 1 nm wide GaAs interlayer is located providing spatial separation. Similarly as for the type-I sample the multiple QWs are surrounded by GaAs and Ga(As,P) layers in order to provide strain compensation [210]. The consequence of such a QW structure is, that the maximum of the valence band and the minimum of the conduction band are located on spatially separated QWs. Due to the attraction between the spatially separated electrons and holes a CTX exists. So, the energetically lowest transition is spatially indirect. A minimal overlap of the corresponding wave functions of the electrons corresponding to (GaIn)As and the spatially separated holes from Ga(As,Sb) is still provided [211]. The reason for this is, that the CTX is characterized by a spatially extended wave function that spans both QWs. The comparison of the nonlinear response between the spatially-direct type-I and spatially-indirect type-II excitons is the main subject of this chapter.
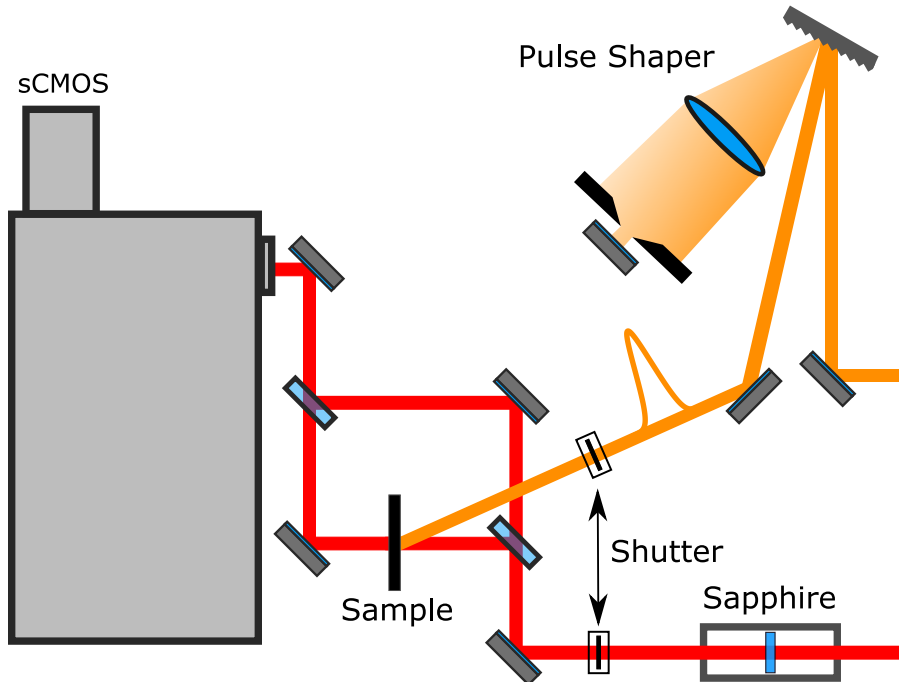
Figure 6.3: Experimental setup to study the pump-induced differential absorption change considering a PP setup. Taken from [212]

A regenerative amplifier system operating at a repetition rate of 5 kHz generates ultrashort pulses with a duration of 50 fs centered around 800 nm. These pulses have a pulse energy of 1.6 mJ. Roughly 30 percent of the amplifier output is utilized to generate a broad spectrum of light known as a white-light supercontinuum. This process occurs in a 6 mm thick

sapphire crystal. The remaining 70 percent of the amplifier output is directed towards an optical parametric amplifier (OPA).

The primary output of the OPA produces short pulses with a tunable central wavelength. These pulses are then shaped by a pulse shaper, see. Fig. 6.3, resulting in a spectral FWHM of approximately 2.71 meV and a duration of 2 ps. The excitation beam is focused onto the sample, forming a spot size of 300 μm. The sample is cooled to liquid helium temperatures using a cryostat with a cold-finger mechanism.

Within the white-light beam path, a wedge beamsplitter is employed to split the light into two separate beams. One beam, focused to 200 μm, interacts with the sample to probe any absorption changes induced by the excitation. The other beam serves as a reference pulse. After passing through the sample, both the white-light supercontinuum and the reference pulse undergo spectral analysis. This analysis is performed using an imaging spectrometer equipped with a 600 lines/mm grating and a scientific complementary metal-oxide semiconductor (sCMOS) camera.

The sCMOS camera consists of 2160 individual lines that can be read out independently or combined into a region of interest (ROI). By directing the white-light pulse transmitted through the sample and the reference pulse onto different regions of the camera, their spectra can be simultaneously and independently captured. This enables a comparison between the two pulses, leading to the calculation of a transfer function T_f. The transfer function converts the spectrum of the reference pulse T_{ref} into the spectrum of the pulse transmitted through the unexcited sample.

Through this setup, we can obtain both the transmission through the excited sample T_P and the transmission through the unexcited sample T_0 simultaneously. In order to calculate the differential absorption at each time step, we first measure the photoluminescence background T_{pl} and the scattered light background T_{bg} in both paths at the beginning of the measurement. Then, using the following equation, one experimentally obtains the differential absorption $\Delta\alpha L$:

$$\Delta\alpha L = -ln\left((T_{\mathrm{P}} - T_{\mathrm{Pl}})/(T_{\mathrm{f}}(T_{\mathrm{ref}} - T_{\mathrm{Bg}}))\right) \qquad (6.1)$$

Moreover, we use this approach to obtain the linear absorption of the sample. To achieve this, we exclude the sample from the beam path and compute the transfer function that converts the reference signal into the spectrum of the pulse transmitted through the sample holder. Subsequently, we reintroduce the sample into the beam path, enabling us to measure the transmission through the unexcited sample and determine its linear absorption properties.

The OPOP experiment show clearly new signatures in the vicinity of the 1s exciton resonance of spatially-indirect type-II QW structure in contrast to the well-investigated type-I excitons. In Fig. 6.4 we see the differential absorption spectrum for an OPOP performed

with co- and counter-circularly polarized laser fields on the type-II QW structure from Fig. 6.2.
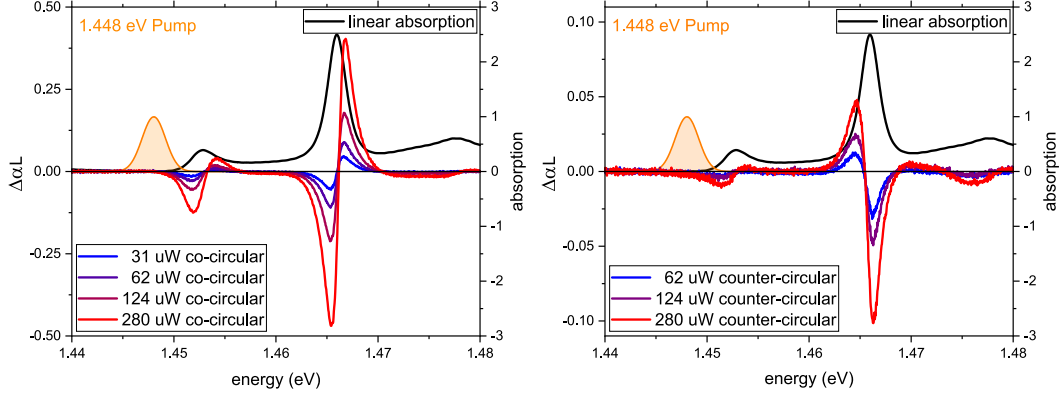
Figure 6.4: Differential absorption signal ($\Delta\alpha L$) for a series of pump pulse intensities in co-circular polarization geometry (left) and counter-circular polarization geometry (right). The black line represents the linear absorption of the sample, and the orange shaded area indicates the pump pulse, which is tuned energetically below the CTX resonance. At the CTX resonance at 1.452 eV, both polarization configurations exhibit a blue shift. Conversely, for the regular exciton of the (Ga,In)As QWs (1.467 eV), co-circular polarization demonstrates a blue shift, while counter-circular polarization displays a red shift. These measurements were performed in the group of Sangam Chatterjee (University of Giessen).

For co- and counter-circular excitation conditions and pumping below the CTX resonance, the characteristic optical Stark effects are observed. Specifically, a blue shift (on the left in Fig. 6.4) and red shift (on the right in Fig. 6.4) in the differential absorption near the X resonance at 1.467 eV is observed [57]. A closer look at the CTX resonance at about 1.452 eV of the type-II heterostructure yields a somewhat different picture. In contrast to the type-I 1s exciton appearing at 1.467 eV the CTX shows mainly a blue shift signature for co-circular polarization and a much weaker signature for counter-circular polarization corresponding to an unexpected blue shift instead of a red shift such as at the X resonance. In order to understand the origin of the blue shift at the CTX for counter-circular excitation condition, we introduce in the following our theoretical approach to describe the excitonic nonlinear response including many-body Coulomb correlations.

6.2 Theoretical model and approach

In the following we introduce the coherent $\chi^{(3)}$-limit to derive a closed set of equations describing the appearing electron-hole pair coherences and biexciton many-body correlations. Thereupon, we present the 1D tight-binding model. In our numerical evaluation we firstly start by showing a comparison between type-I QW excitons and type-II QW excitons. The major differences in their nonlinear response by analyzing the differential

absorption spectrum within a pump probe configuration is demonstrated. Moreover, we also compare our theoretical findings with the measurements presented in Fig. 6.4 which have been performed on the type-II QW structure, see Fig. 6.2 (right).

6.2.1 The SBE in the coherent $\chi^{(3)}$-limit

Similarly as in chapter 2.1 we start with the following Hamiltonian describing the nonlinear dynamics in photoexcited semiconductors [2, 56]:

$$\hat{H} = \hat{H}_0 + \hat{H}_{L-M} + \hat{H}_C$$

(6.2)

Here, the single-particle energies are included via $\hat{H}_0$. In second quantization working in the electron-hole picture the single particle Hamiltonian in real space reads [56]

$$\hat{H}_0 = \sum_{ijc} T^c_{ij} \hat{c}_i^{c\dagger} \hat{c}_j^c + \sum_{ijc} T^v_{ij} \hat{d}_i^{v\dagger} \hat{d}_j^v.$$

(6.3)

The creation of an electron (hole) at site i in band c (v) is given by $\hat{c}_i^{c\dagger}$ ($\hat{d}_i^{v\dagger}$). And $\hat{c}_i^c$ ($\hat{d}_i^v$) destroys an electron (hole) at site i in band c (v). The electronic coupling is used in the nearest-neighbor approximation which is included in the matrices $T^{c,v}_{i,j}$. The diagonal terms of the matrices T contain the electronic site energies and the couplings between the sites are given by the off-diagonal matrix elements. The Hamiltonian describing the light-matter interaction is described by [56]

$$\hat{H}_{L-M} = -\mathbf{E}(t) \cdot \hat{\mathbf{P}},$$
$$\text{with} \quad \hat{\mathbf{P}} = \sum_{ijvc} \left(\boldsymbol{\mu}_{ij}^{vc} \hat{d}_i^v \hat{c}_j^c + \left(\boldsymbol{\mu}_{ij}^{vc} \right)^* \hat{c}_j^{c\dagger} \hat{d}_i^{v\dagger} \right).$$

(6.4)

The polarization direction plays a crucial role when analyzing PP or FWM signals. Therefore, it is necessary to consider the vector character of the dipole matrix element $\boldsymbol{\mu}$, the electric field $\mathbf{E}$, and the total optical polarization $\mathbf{P}$ which is defined by the summation of all microscopic polarization $\boldsymbol{\mu}_{ij}^{vc} \hat{d}_i^v \hat{c}_j^c$. The Hamiltonian describing the many-body Coulomb interaction reads [56]

$$\hat{H}_C = \frac{1}{2} \sum_{ij} \sum_{vv'} \left(\hat{c}_i^{v\dagger} \hat{c}_i^v - \hat{d}_i^{v\dagger} \hat{d}_i^v \right) V_{ij}^{vv'} \left(\hat{c}_j^{v'\dagger} \hat{c}_j^{v'} - \hat{d}_j^{v'\dagger} \hat{d}_j^{v'} \right).$$

(6.5)

Here, the superscripts v and v' label the relevant valence and conduction bands. The many-body Coulomb interactions are approximated by a monopole-monopole interaction [213]. H_C includes the repulsion between electrons and between holes, respectively, as well as the attraction between electrons and holes, which gives rise to the formation of bound electron-hole complexes, for instance excitons and biexcitons.

The equation of motion for the single exciton amplitude containing all contributions of $\hat{H} = \hat{H}_0 + \hat{H}_{lm} + \hat{H}_C$ is described by $\frac{d}{dt} p_{12}^{v_1 c_2} = \frac{i}{\hbar} \langle [\hat{H}, \hat{d}_1^{v_1} \hat{c}_2^{c_2}] \rangle$[1] and reads [56, 60, 62]

$$
\begin{aligned}
-i\hbar \frac{d}{dt} p_{12}^{v_1 c_2} = &- \sum_{jc} T_{2j}^c p_{1j}^{v_1 c} - \sum_{iv} T_{i1}^v p_{i2}^{v c_2} + V_{12}^{v_1 c_2} p_{12}^{v_1 c_2} \\
&+ \mathbf{E}(t) \cdot \left[\left(\boldsymbol{\mu}_{12}^{v_1 c_2} \right)^* - \sum_{jc} \left(\boldsymbol{\mu}_{1j}^{v_1 c} \right)^* n_{j2}^{c c_2} - \sum_{iv} \left(\boldsymbol{\mu}_{i2}^{v c_2} \right)^* n_{i1}^{v v_1} \right] \\
&+ \sum_{a v_a} V_{a1}^{v_a v_1} \langle \hat{d}_a^{v_a} \hat{d}_1^{v_1} \hat{d}_a^{v_a \dagger} \hat{c}_2^{c_2} \rangle - \sum_{a v_a} V_{2a}^{c_2 v_a} \langle \hat{d}_1^{v_1} \hat{d}_a^{v_a} \hat{c}_2^{c_2} \hat{d}_a^{v_a \dagger} \rangle \\
&+ \sum_{a c_a} V_{a1}^{c_a v_1} \langle \hat{c}_a^{c_a \dagger} \hat{d}_1^{v_1} \hat{c}_a^{c_a} \hat{c}_2^{c_2} \rangle - \sum_{a c_a} V_{2a}^{c_2 c_a} \langle \hat{d}_1^{v_1} \hat{c}_a^{c_a \dagger} \hat{c}_2^{c_2} \hat{c}_a^{c_a} \rangle.
\end{aligned}
\tag{6.6}
$$

In eq. (6.6) we introduced the electron and hole coherences as $n_{jj'}^{cc'} = \langle \hat{c}_j^{c \dagger} \hat{c}_{j'}^{c'} \rangle$ and $n_{ii'}^{vv'} = \langle \hat{d}_i^{v \dagger} \hat{d}_{i'}^{v'} \rangle$. Moreover, the first step of the hierarchy problem due to four-point operators appearing in eq. (6.6) arises. Since we consider only weak excitation a perturbative analysis with respect to electric fields can be performed. Furthermore, no interactions with other quasiparticles are included. Under these considerations the coherent $\chi^{(3)}$-limit can be considered. In this sense, the intraband coherences can be described only via the polarization p [60–62]

$$
n_{12}^{c_1 c_2} = \sum_{a v_a} p_{a2}^{v_a c_2} \left(p_{a1}^{v_a c_1} \right)^* \quad \text{and} \quad n_{12}^{v_1 v_2} = \sum_{a c_a} \left(p_{1a}^{v_1 c_a} \right)^* p_{2a}^{v_2 c_a}.
\tag{6.7}
$$

The factorization in eq. (6.7) results from the dynamics-controlled truncation (DCT). This approach can also be applied to the four-point operators appearing in eq. (6.6) which leads to [60–62]

$$
\langle \hat{d}_a^{v_a \dagger} \hat{d}_1^{v_1} \hat{d}_a^{v_a} \hat{c}_2^{c_2} \rangle = \sum_{b c_b} \langle \hat{d}_1^{v_1} \hat{c}_b^{c_b} \hat{d}_a^{v_a} \hat{c}_2^{c_2} \rangle \langle \hat{c}_b^{c_b \dagger} \hat{d}_a^{v_a \dagger} \rangle
\tag{6.8}
$$

Only two physical quantities, $p = \langle dc \rangle$ and $B = \langle dcdc \rangle$, remain to describe the optical response in the coherent $\chi^{(3)}$-limit. They are schematically illustrated in Fig. 6.5.

---

[1] Here, the site indices are denoted by 1 and 2, while v_1 and c_2 describe the respective bands.
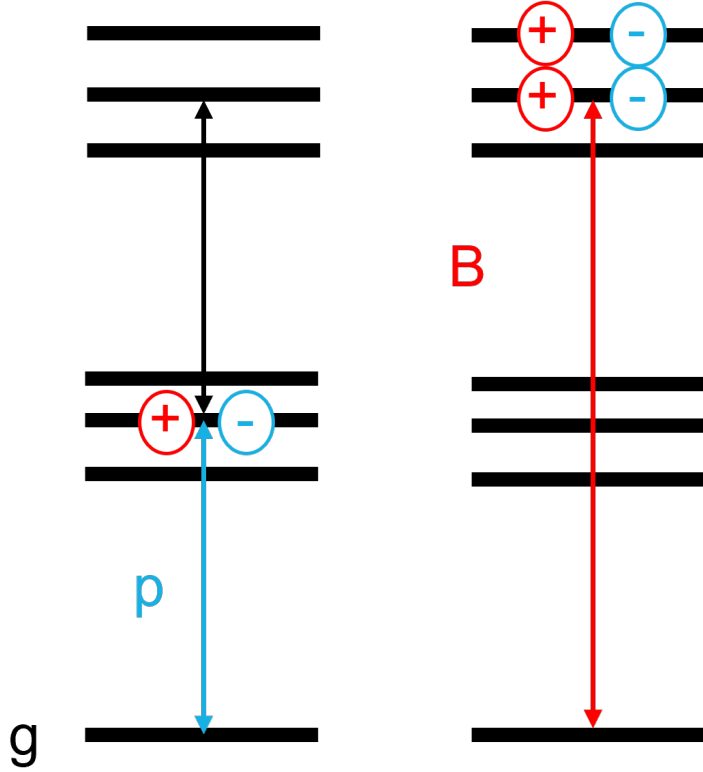
Figure 6.5: Schematical drawing of the main quantities $p = \langle dc \rangle$ and $B = \langle dcdc \rangle$ appearing in the coherent $\chi^{(3)}$-limit.

The single-exciton amplitude $p_{12}^{v_1 c_2}$ describes one electron-hole pair coherences, whereas the two-exciton coherence is expressed by $B_{1324}^{v_1 c v c_2} = \langle \hat{d}_1^{v_1} \hat{c}_3^{c} \hat{d}_2^{v} \hat{c}_4^{c_2} \rangle$. Furthermore, we define the following:

$$\overline{B}_{1324}^{v_1 c v c_2} = B_{1324}^{v_1 c v c_2} + p_{14}^{v_1 c_2} p_{23}^{vc} - p_{13}^{v_1 c} p_{24}^{vc_2} \tag{6.9}$$

Using the definition (6.9), it becomes possible to analyze pure correlation effects that go beyond the scope of the TDHF approximation [214]. Overall, we obtain a closed set of equations describing the dynamics of the coherence between the ground and the single-

exciton state p_{12}^{vc} or a two-exciton state $\overline{B}_{ba12}^{v'c'vc}$ [56, 60, 62]:

$$
\begin{aligned}
- i\hbar \frac{d}{dt} p_{12}^{vc} &= - \sum_{j} T_{2j}^{c} p_{1j}^{vc} - \sum_{i} T_{i1}^{v} p_{i2}^{vc} + V_{12}^{vc} p_{12}^{vc} \\
&+ \mathbf{E}(t) \cdot \left[\left(\mu_{12}^{vc} \right)^{*} - \sum_{abv'c'} \left(\left(\mu_{1b}^{vc'} \right)^{*} \left(p_{ab}^{v'c'} \right)^{*} p_{a2}^{v'c} + \left(\mu_{b2}^{v'c} \right)^{*} \left(p_{ba}^{v'c'} \right)^{*} p_{1a}^{vc'} \right) \right] \\
&+ \sum_{abv'c'} \left(V_{a2}^{c'c} - V_{a1}^{c'v} - V_{b2}^{v'c} + V_{b1}^{v'v} \right) \\
&\times \left[(p_{ba}^{v'c'})^{*} p_{b2}^{v'c} p_{1a}^{vc'} - (p_{ba}^{v'c'})^{*} p_{ba}^{v'c} p_{12}^{vc} - (p_{ba}^{v'c'})^{*} \overline{B}_{ba12}^{v'c'vc} \right]
\end{aligned}
\tag{6.10}
$$

The time derivative of the single-exciton amplitude (6.10) contains the on site energies, electronic couplings, and the electron-hole attraction V_{12}^{vc} within the first line. Furthermore, three nonlinearities including the linear absorption are provided. The PB term $(\mathbf{E}(t) \cdot \boldsymbol{\mu} p^{*} p)$ is also known from the OBE [2, 127, 215]. The linear source term is given by $\mathbf{E}(t) \cdot \boldsymbol{\mu}$. Due to the Coulomb interaction two inhomogeneities known as the first order Coulomb interaction $CI_{1st} \propto p^{*} pp$ and the correlation term $CI_{corr} \propto Vp^{*}B$ [63, 181] exist. The latter describes the contribution originating from two-exciton coherences. So, it is possible to analyze the contributions that arise from the three nonlinear inhomogeneities separately. Without the correlation term, these equations are equivalent considering the TDHF approximation. The equation of motion for the two-exciton coherence $\overline{B}_{ba12}^{v'c'vc}$ reads [56, 60, 62]

$$
\begin{aligned}
- i\hbar \frac{d}{dt} \overline{B}_{ba12}^{v'c'vc} &= - \sum_{i} \left(T_{2i}^{c'} \overline{B}_{ba1i}^{v'c'vc} + T_{i1}^{v'} \overline{B}_{bai2}^{v'c'vc} + T_{ai}^{c'} \overline{B}_{bi12}^{v'c'vc} + T_{ib}^{v'} \overline{B}_{ia12}^{v'c'vc} \right) \\
&+ \left(V_{ba}^{v'c'} + V_{b2}^{v'c} + V_{1a}^{vc'} + V_{12}^{vc} - V_{b1}^{v'v} - V_{a2}^{c'c} \right) \overline{B}_{ba12}^{v'c'vc} \\
&- \left(V_{ba}^{v'c'} + V_{12}^{vc} - V_{b1}^{v'v} - V_{a2}^{c'c} \right) p_{1a}^{vc'} p_{b2}^{v'c} \\
&+ \left(V_{1a}^{vc'} + V_{b2}^{v'c} - V_{b1}^{v'v} - V_{a2}^{c'c} \right) p_{ba}^{v'c'} p_{12}^{vc} .
\end{aligned}
\tag{6.11}
$$

Again, the first line of eq. (6.11) contains the electronic energies and couplings. Furthermore, four attraction and two repulsion interaction terms between the two electrons and holes exist. The two-exciton amplitude $\overline{B}_{ba12}^{v'c'vc}$ includes exciton to bound biexciton as well as to unbound continuum states transitions. The nonlinearities that are contained in $\overline{B}_{ba12}^{v'c'vc}$ are contributions which depend on the many-body interaction (Vpp). Similarly as in momentum space (see eq. (2.18)) the nonlinear response is fully described by eqs. (6.10)-

(6.11) and is given by the total polarization $\mathbf{P}$:

$$\mathbf{P} = \sum_{ijvc} \mu_{ij}^{vc} p_{ij}^{vc} \qquad (6.12)$$

6.2.2 One-dimensional tight-binding model

Due to the fact that the numerical evaluation considering higher-order Coulomb correlation terms is quite demanding, the theoretical findings in the following are obtained by an 1D model. Such a model is still able to provide results which are in good agreement with several experimental observations in QW systems[57–59, 63]. The electronic coupling is used in the tight-binding approximation and is included via the matrices $T_{ij}^{v,c}$. The site on energies of electrons and holes are given by the diagonal terms in the matrices $T_{ii}^{v,c} = \varepsilon_i^{v,c}$. The electron couplings in the nearest neighbor approximation $T_{ij}^{v,c} = J_{v,c}$ with |i-j|=1 are described by the off-diagonal matrix elements of T. Furthermore, we consider periodic boundary conditions in such a way that site $N+i$ is equivalent to i. This provides a coupling $J_{v,c}$ between the now nearest neighbors N and 1 because site $N + 1$ is identical to site 1. Neglecting any kind of disorder effects, the energy of a band does not depend on the sites. Thus, we can shift them in such a way that the 1s hh-exciton resonance appears at zero energy. The Coulomb matrix elements are given by following equation

$$V_{ij}^{vv'} = U_0 \frac{d}{d|i - j| + a_0^{vv'}}, \qquad (6.13)$$

where the strength of interaction is given by U_0. For $V_{ij}^{vv'} \propto -|i - j|^{-1}$ the attractive electron-hole Coulomb interaction leads in one dimension to a diverging ground-state energy. We add a regularization parameter $a_0^{vv'}$ in the denominator which is on the order of the effective site distance constant d [56]. Here, we have slightly extended the 1D model to describe spatially-indirect QW systems. The Coulomb matrix elements $V_{ij}^{vv'}$ that describe the attraction between an electron and a hole located in the same QW (both in (Ga,In)As) are larger than when the hole is located in the spatially separated QW (electron in (Ga,In)As and hole in Ga(As,Sb)). This is schematically shown in Fig. 6.6. To describe this accordingly, we can adjust the spatial variation $\frac{d}{a_0^{vv'}}$ of the electron-hole attraction. For homogeneous spatially-direct QW structures, it is not necessary to consider that the regularization parameter $a_0^{vv'}$ depends on the band indices because the attraction and repulsion between the particles are similar. The differential absorption spectrum $\delta\alpha(\omega)$ is determined by the differential polarization $\delta\mathbf{P}$ and can be calculated by using eq. (2.24).
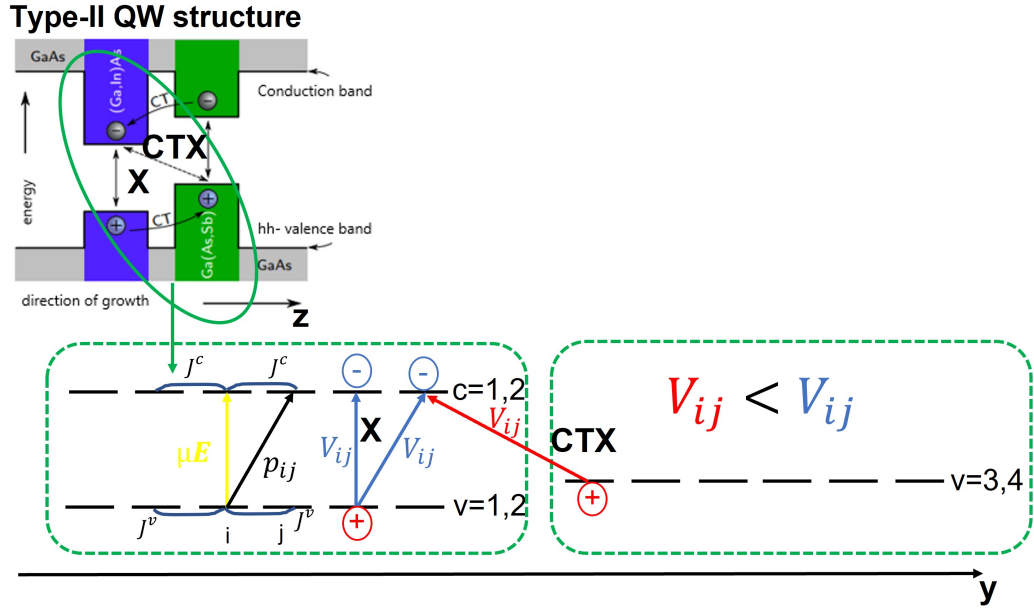
Figure 6.6: Here, we present an overview of our description of the type-II heterostructure. Above the type-II QW structure is shown (taken from [206]). Additionally, we provide an illustration of the 1D tight-binding model that describes this system. The model focuses on the hh valence bands of two QWs, specifically (GaIn)As and Ga(As,Sb). In the 1D model, the single-exciton amplitude is given by p_{ij}, the Coulomb interaction between particles at sites i and j within the same QW is denoted by a solid blue line. The Coulomb interaction between QWs that are spatially separated is depicted in red. The direction of the sites within the 1D model reflects the in-plane orientation (y) of the QWs.

The dipole matrix elements are given by μ_{ij}^{vc} with the band indices v and c. For type-I QW systems we consider two valence ($v_{1,2}$) (heavy-hole) and conduction bands ($c_{1,2}$) which are described by the degenerate states $|\pm 3/2\text{hh}\rangle$ and $|\pm 1/2\text{e}\rangle$, respectively. The optical transitions are described by the well-known selection rules for zinc blende materials and describe circularly-polarized transitions. For the case of type-II QW structures we include two additional valence bands ($v_{3,4}$) which represent the spatially-separated states in the other QW of the type-II system with the same dipole selection rules as shown in Fig. 6.7.
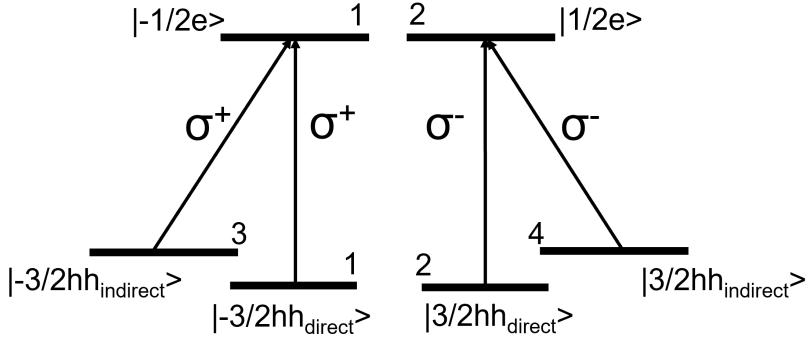
Figure 6.7: Illustration of the optical interband transitions considering a type-II QW system. The selection rules correpond to zinc blende materials, i.e., GaAs based semiconductor nanostructures.

The dipole matrix elements within the one-dimensional model read

$$
\mu_{ij}^{11} = \delta_{ij} \frac{\mu_{\text{Type–I}}}{\sqrt{2}} \begin{pmatrix} 1 \\ i \end{pmatrix} \quad, \mu_{ij}^{22} = \delta_{ij} \frac{\mu_{\text{Type–I}}}{\sqrt{2}} \begin{pmatrix} 1 \\ -i \end{pmatrix} \quad, \mu_{ij}^{12} = \mu_{ij}^{21} = 0 \tag{6.14}
$$

$$
\mu_{ij}^{31} = \delta_{ij} \frac{\mu_{\text{Type–II}}}{\sqrt{2}} \begin{pmatrix} 1 \\ i \end{pmatrix} \quad, \mu_{ij}^{42} = \delta_{ij} \frac{\mu_{\text{Type–II}}}{\sqrt{2}} \begin{pmatrix} 1 \\ -i \end{pmatrix} \quad, \mu_{ij}^{32} = \mu_{ij}^{41} = 0 \tag{6.15}
$$

Here, $\mu_{\text{Type–I,Type–II}}$ denotes the strength of the interband transition. We always consider the case $\mu_{\text{Type–I}} \geq \mu_{\text{Type–II}}$. Due to the tight-binding description optical excitations are only possible at same sites of electron-hole complexes. In this thesis, we always consider as many sites as it requires to obtain converged results for the signatures of the excitonic optical response. We use phenomenological dephasing times $\frac{1}{\gamma_p}$ and $\gamma_{\overline{B}} = 2\gamma_p$.

Since we only take hh excitations into account, the linear response is fully described by p^{11} and p^{22} for spatially-direct type-I QWs. Additionally, the coherences p^{31} and p^{42} contribute if a spatially-indirect QW structure is considered. Two-exciton coherences only appear in second order in respect to the electric fields. Here, either bound or unbound two-exciton states can be induced by a proper choice of the polarization direction of the incident laser fields. For co-circular excitation conditions ($\sigma^+\sigma^+$) only unbound continuum states are excited. Bound biexcitons will contribute for instance in the case of counter-circularly polarized laser fields ($\sigma^+\sigma^-$) within a PP setup. Due to the antisymmmetry of the two-exciton amplitude $\overline{B}_{ba12}^{v'c'vc}$ it is sufficient to calculate only $\overline{B}_{ba12}^{1122}$ since we can use $\overline{B}_{ba12}^{2211} = -\overline{B}_{12ba}^{1122}$. Similarly, it is possible to excite a so called charge transfer biexciton (CTB) if a type-II QW structure is described. Because of the selection rules, the total nonlinear response in third order within the coherent $\chi^{(3)}$-limit only depends on p^{11} (X), p^{22} (X), p^{31}(CTX) and p^{42}(CTX).

6.2.3 Numerical results for type-I and type-II excitons
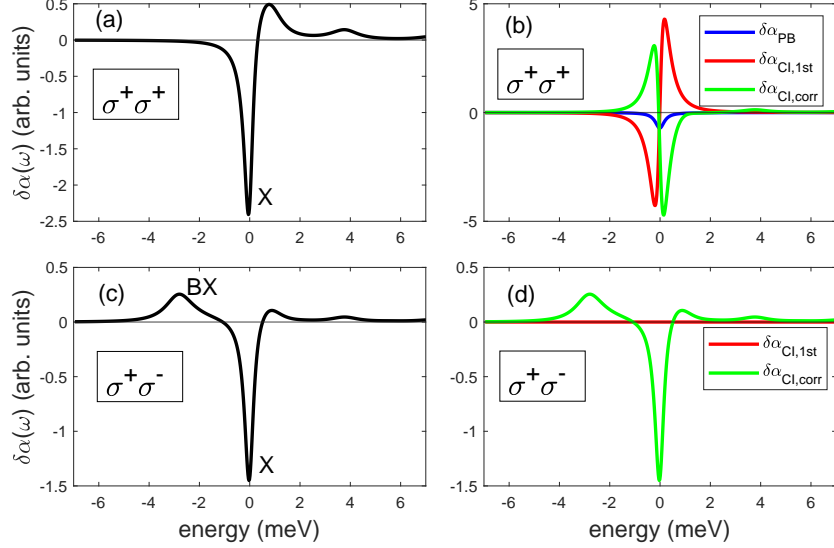
Figure 6.8: The model parameters are presented in Table A.1 (HH-I). The spatially-direct exciton (X) is excited resonantly considering a time delay $\tau = 2$ ps. In (a) and (c) we show the total pump-induced differential absorption $\delta\alpha(\omega)$ for co-circular ($\sigma^+\sigma^+$) as well as for counter-circular ($\sigma^+\sigma^-$) excitation conditions, respectively. The different nonlinearities $\delta\alpha_{PB}$, $\delta\alpha_{CI_{1st}}$, and $\delta\alpha_{CI_{corr}}$ which contribute to the signals in (a) and (c) are demonstrated in (b) and (d), respectively. Taken from [216]

Firstly, we show the excitonic nonlinear response for a spatially-homogeneous type-I QW structure. In Fig. 6.8(a) the pump-induced differential absorption $\delta\alpha(\omega)$ for co-circularly polarized pump and probe pulses is shown. The optical-pump pulse is tuned to the X resonance. The response in the vicinity of the direct X mainly corresponds to pump-induced bleaching. Fig. 6.8(b) displays the individual contributions originating from Pauli blocking (PB), first-order Coulomb interaction (CI_{1st}), and higher-order correlation effects (CI_{corr}).

Comparing to the Coulomb-induced contributions, PB is relatively weak and exhibits pure bleaching at the exciton resonance. The CI_{1st} contribution is larger and shows a dispersive lineshape, corresponding to a blue shift, which is the dominant feature within the TDHF approximation. On the other hand, the CI_{corr} contribution provides a red shift. As a result, there are strong cancellations between the two Coulomb contributions. Additionally, the CI_{corr} term exhibits weak induced absorption peaks above the exciton that describe transitions from the exciton to unbound two-exciton resonances.

When counter-circularly polarized excitation conditions are applied to type-I QW systems,

the only contribution to the differential absorption spectrum originates from CI_corr. The reason for this is that PB does not couple the two spin subspaces due to the selection rules. In contrast, the CI_1st contribution can play a role under specific conditions that depend on the system itself. Upon closer examination of the CI_1st contribution reveals that the term $\propto p_{ba}^{v'c'*} p_{ba}^{v'c'} p_{12}^{vc}$ leads to a coupling between the coherences of the spin subspaces. But this contribution is only finite for spatially-inhomogeneous systems. This is not the case for a spatially-direct type-I QW structure. When we only consider the individual coherences for $\sigma^+\sigma^-$ excitation conditions, the corresponding microscopic polarization that determines the excitonic nonlinear response reads

$$\partial_t p_{12}^{vc} \propto \sum_{abv'c'} \left(V_{a2}^{c'c} - V_{a1}^{c'v} - V_{b2}^{v'c} + V_{b1}^{v'v} \right) (p_{ba}^{v'c'})^* \left(p_{ba}^{v'c'} p_{12}^{vc} \right). \tag{6.16}$$

For homogeneous systems the entire term in eq. (6.16) vanishes. This can be easily understood by the fact that the relation $p_{ba}^{vc} = p_{ab}^{vc}$ is fulfilled in a homogeneous system. The product between the coherences in eq. (6.16) is a symmetric function $g(a,b) = g(b,a) = (p_{ba}^{v'c'})^* p_{ba}^{v'c'} p_{12}^{vc} = (p_{ab}^{v'c'})^* p_{ab}^{v'c'} p_{12}^{vc}$ with respect to interchanging a and b. However, the prefactor $f(a,b) = \left(V_{a2}^{c'c} - V_{a1}^{c'v} - V_{b2}^{v'c} + V_{b1}^{v'v} \right)$ changes its sign when a and b are interchanged. Consequently, the sum over the sites a and b appearing in eq. (6.16) vanishes and a CI_1st contribution does not exist in a homogeneous system. This is demonstrated in Fig. 6.8(d).

Besides the induced absorption peaks above the exciton resonance the higher-order Coulomb interaction term CI_corr also shows induced absorption due to a bound biexciton (BX) below the X which is clearly seen in Fig. 6.8(c). The corresponding binding energy corresponds to an energy of about 2.6 meV.
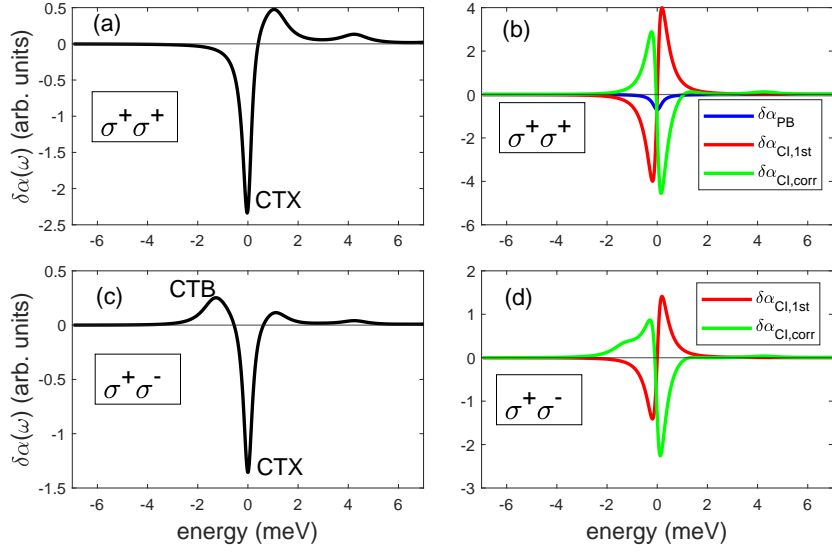
Figure 6.9: The model parameters are presented in Table A.1 (HH-II). The spatially-indirect CTX is excited resonantly considering a time delay $\tau = 2$ ps. In (a) and (c) we show the total pump-induced differential absorption $\delta\alpha(\omega)$ for co-circular ($\sigma^+\sigma^+$) as well as for counter-circular ($\sigma^+\sigma^-$) excitation conditions, respectively. The different nonlinearities $\delta\alpha_{\mathrm{PB}}$, $\delta\alpha_{\mathrm{CI_{1st}}}$, and $\delta\alpha_{\mathrm{CI_{corr}}}$ which contribute to the signals in (a) and (c) are demonstrated in (b) and (d), respectively. Taken from [216]

For a direct comparison with a spatially-indirect QW structure we show in Fig. 6.9 the nonlinear response when a CTX is excited under same conditions. The CTX has a lower binding energy due to a weaker attraction between electrons and holes located at spatially separated QWs. This results in a reduced binding energy which is about 2 meV smaller than that of the direct exciton in the homogeneous system. When comparing the Figs. 6.9(a) and 6.8(a) for co-circular polarized excitation conditions with each other, the signatures appearing in the vicinity of the direct X and the CTX originating from the nonlinearities are mainly the same leading in both cases to a similar behavior of the total differential absorption spectrum $\delta\alpha(\omega)$.

However, the pump-induced differential absorption shows some differences when we look more closely to the case of counter-circularly polarized laser pulses. In contrast to the spatially-direct type-I QW structure the appearance of the induced absorption due to a bound charge transfer biexciton (CTB) below the CTX is much closer to the CTX resonance. This significant reduction of the binding energy to about 1.9 meV depends sensitively on the Coulomb interactions occurring between the particles in the same QW (we denote them as interwell Coulomb interaction) or located in spatially separated QWs (we denote them as intrawell Coulomb interaction) as is the case for spatially-indirect type-II QW structures. Regarding the two-exciton coherences, see. eq. (6.11), two intrawell Coulomb

interactions (repulsion between two holes and two electrons, respectively) arise which are stronger than the four interwell interactions between electrons and holes (attraction) at spatially separated QWs and are the main reason for the reduced binding energy.

Regarding the nonlinearities which contribute to the total differential absorption spectrum we see in Fig. 6.9(d) a strong contribution arises from the CI_{1st} term which is absent in homogeneous systems and is provided in inhomogeneous systems (for instance disordered systems [32, 217]). In disordered systems, the interband coherence does not only depend on the relative spatial coordinate anymore because the band gap energy at different sites is not equal. In type-II QW structures, however, the interband coherence still only depend on the relative spatial coordinate. Instead, the inhomogeneity arises due to different Coulomb interactions. We have to distinguish between interwell and intrawell Coulomb interactions. Similarly as in the case of the type-I QW structure we can indicate the origin of CI_{1st} by considering the main contribution of the corresponding coherence by looking closely to the CI_{1st} term. Here, the corresponding hole and electron correspond to spatially separated QWs with $v = 4$ and $c = 2$, respectively. Due to the fact that the repulsion and attraction between the considered particles is not the same, the prefactor $f(a, b)$ does not change its sign anymore by swapping its arguments a and b leading to a finite CI_{1st} contribution. In total, we still obtain a pump-induced bleaching signature in the vicinity of the CTX due to the cancellation with the CI_{corr} term, see Fig. 6.9(c).

Concerning the OPOP experiment introduced in chapter 6.1 we can also analyze the general behavior of the excitonic nonlinear response when we excite below the CTX resonance considering different optical detunings Δ. Since there is a finite first order Coulomb interaction for counter-circularly polarized laser pulses, we can also analyze the pump induced absorption change in dependence on the spatial inhomogeneity at the same time.
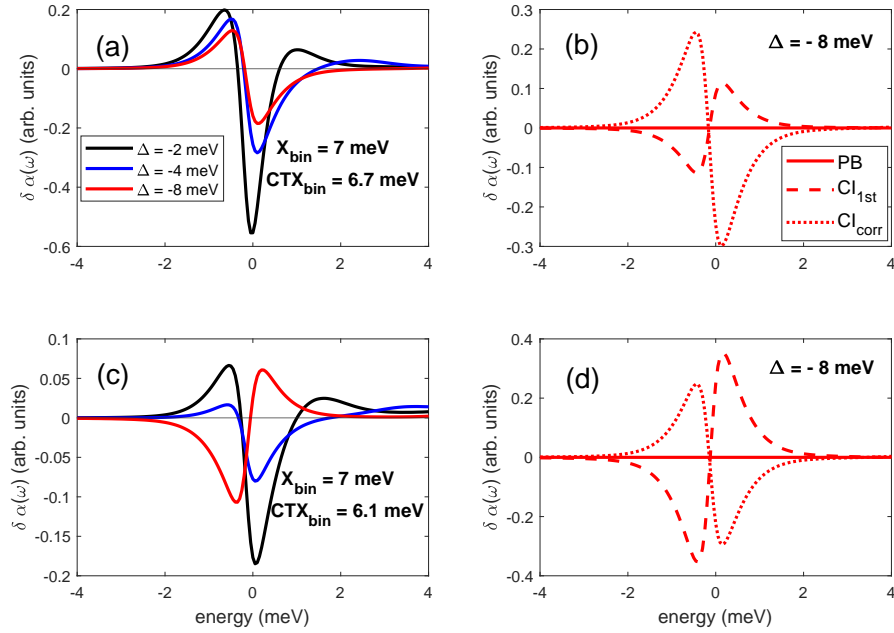
Figure 6.10: The model parameters are presented in Table A.1 (HH-III and HH-IV providing the two different binding energies of $CTX_{bin} = 6.7$ meV and $CTX_{bin} = 6.1$ meV, respectively). The spatially-indirect charge transfer exciton (CTX) is excited off-resonantly considering zero time delay and different optical detunings Δ. In (a) and (c) we show the total pump-induced differential absorption $\delta\alpha(\omega)$ for counter-circular ($\sigma^+\sigma^-$) excitation conditions considering two different binding energies of the CTX corresponding to $CTX_{bin} = 6.7$ meV and $CTX_{bin} = 6.1$ meV, respectively. In both cases the binding energy of the X remains the same $X_{bin} = 7$ meV (intrawell interaction remains the same). The different nonlinearities $\delta\alpha_{PB}$, $\delta\alpha_{CI_{1st}}$, and $\delta\alpha_{CI_{corr}}$ which contribute to the signals from (a) and (c) for an optical detuning $\Delta = -8$ meV are displayed in (b) and (d), respectively.

Firstly, we see in all the cases in Fig. 6.10(a) that a red shift is originating from the CI_{corr} term which is dominating, see Fig. 6.10(b). The spatial inhomogeneity is weak in this case. If the attraction between electron and holes (interwell Coulomb interaction) located at different sites is further decreased, we can obtain unexpected signatures at the CTX. An optical detuning $\Delta = -8$ meV leads to a blue shift originating from CI_{1st}. Applying an optical detuning of $\Delta = -4$ meV, we mostly obtain a bleaching signature, although we still excite below the CTX resonance. This arise due to cancellation of the CI_{1st} and the Coulomb correlation CI_{corr} contribution. This is an unexpected result which so far not have been investigated and observed. For even smaller detuning resonant contributions as the excitation of a bound CTB is provided and is slightly visible. If the intrawell interaction is much stronger than the interwell interaction a blue shift is mostly provided because the CI_{1st} term is dominating. This kind of behavior for nonresonant excitations becomes

important if we investigate the optical Stark shifts which are measured and shown in chapter 6.1.

6.3 Comparison with optical-pump optical-probe experiment

Here, we theoretically investigate OPOP experiments considering our theoretical model presented in section 6.2.2. Likewise to an ensemble of quantum dots a QW structure exhibit inhomogeneous broadening due to variations in their thickness and alloy composition across the well structure. These variations result in a distribution of energy levels within the ensemble of quantum wells that is related to a distribution function $g(\tilde{E})$ that indicate the respective weight of the corresponding transition frequency $\tilde{E}$. The inhomogeneous broadening typically dominates over the homogeneous linewidth. This is also the case for the considered QW structures illustrated in Fig. 6.2. In the case of spatially-indirect type-II QW structures, the direct X and the CTX are broadened to different extents. In order to consider this, we apply correlated inhomogeneous broadening of the two valence bands for the type-II QW system in our 1D tight-binding model. Therefore, we solve the single exciton amplitude p_{12}^{vc} and the two-exciton coherence $B_{ba12}^{v'c'vc}$ for many different transition frequencies $\tilde{E}$. This is shown schematically below by considering only the tight-binding part of eqs. (6.10) and (6.11).

$$-i\hbar \frac{d}{dt} p_{12}^{vc}(\tilde{E}) = -\left(\underbrace{\sum_j T_{2j}^c p_{1j}^{vc} + \sum_i T_{i1}^v p_{i2}^{vc}}_{\propto \tilde{E} = \varepsilon^v + E_{\text{Offset}}^v + \varepsilon^c} \right) \tag{6.17}$$

$$-i\hbar \frac{d}{dt} \overline{B}_{ba12}^{v'c'vc}(\tilde{E}) = -\sum_i \left(\underbrace{T_{2i}^c \overline{B}_{ba1i}^{v'c'vc} + T_{i1}^v \overline{B}_{bai2}^{v'c'vc} + T_{ai}^{c'} \overline{B}_{bi12}^{v'c'vc} + T_{ib}^{v'} \overline{B}_{ia12}^{v'c'vc}}_{\propto \tilde{E} = \varepsilon^v + E_{\text{Offset}}^v + \varepsilon^{v'} + E_{\text{Offset}}^{v'} + \varepsilon^c + \varepsilon^{c'}} \right) \tag{6.18}$$

In our theoretical model we consider overall four valence bands where $v = 1, 2$ indicate the QW (Ga,In)As and $v = 3, 4$ correspond to $Ga(As, Sb)$, see Fig. 6.2. The energy shift E_{Offset}^v depends on the considered valence band providing the possibility to apply different inhomogeneous broadenings for the direct X and the CTX, i.e., $E_{\text{Offset}}^{3,4} = \alpha E_{\text{Offset}}^{1,2}$. A positive value $\alpha > 0$ describes the case of correlated inhomogeneous broadening and provide a larger broadened linewidth for the CTX resonance which is the case in the considered type-II QW structure. The inhomogeneous macroscopic polarization is defined by the following

relation considering the distribution function $g(\tilde{E})$ of different transition frequencies.

$$\mathbf{P} = \sum_{ijvc} \int d\tilde{E} \boldsymbol{\mu}_{ij}^{vc} p_{ij}^{vc}(\tilde{E}) g(\tilde{E}) \text{ with } g(\tilde{E}) = \frac{1}{\sigma\sqrt{2\pi}} e^{-\left(\frac{\tilde{E}}{\sqrt{2}\sigma}\right)^2} \qquad (6.19)$$

The width of the inhomogeneous broadening is determined by σ. From the experimental measurements it is known that the inhomogeneous broadening of the direct X is about 1.5 meV whereas for the type-II exciton resonance it is of about 3 meV. Therefore, we use $\alpha = 1.6$ which provides a qualitative good agreement between experiment and theory especially for pump-induced differential absorption spectra shown in Fig. 6.12 and Fig. 6.13. The chosen parameters to reproduce the experimental results can be found in the appendix A.2. Firstly, we compare the linear absorption spectrum between experiment and theory which is shown in Fig. 6.11. Therefore, it is only necessary to solve eq. (6.10) in first order. We always consider a probe pulse with a pulse duration of 10 fs. For the comparison, we shift the 1s type-I exciton resonance to zero on the energy scale. The site energies of the valence bands $v = 3, 4$ are adjusted in such way that the energetic position corresponds to the one measured in the experiment. The Coulomb interaction between particles from the same QW is stronger than between spatially separated particles leading to a larger exciton binding energy for the X ($X_{bin} = 7$meV) than for the CTX ($CTX_{bin} = 4.6$ meV). Such binding energies were also observed in measurements for these kind of QW structures.
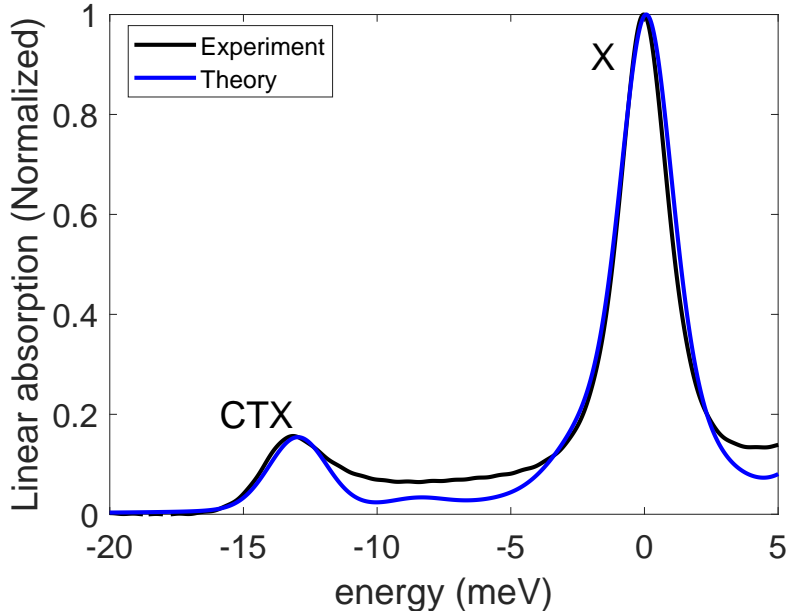
Figure 6.11: Linear absorption spectrum measured for the spatially-indirect type-II QW structure shown in Fig. 6.2 and theoretically calculated by solving the eq. (6.10) in first order. The model parameters are presented in Table A.1 (HH-V).

Besides the absence of the CTX resonance the linear absorption spectrum for the spatially-direct type-I QW structure (not shown here) would look in principle similar to the case of the type-II heterostructure. The behavior of the nonlinear response of spatially-direct excitons can thus be investigated directly by considering type-II QW systems only. The main difference between spatially-direct excitons for type-II QW structure is the much more rapid dephasing [218]. In Figs. 6.12 and 6.13 a comparison between experimental and theoretical results of the pump-induced differential absorption change is shown. The measurements were performed with co-circularly and counter-circularly polarized laser fields, while pumping 5 meV (18 meV) below the CTX (X) in a type-II heterostructure. Using the approach mentioned above to include inhomogeneous broadening ($\alpha = 1.6$ and the FWHM of the $g(\tilde{E})$ corresponds to 1.5 meV) the theoretical spectra qualitatively fit well the measurements.
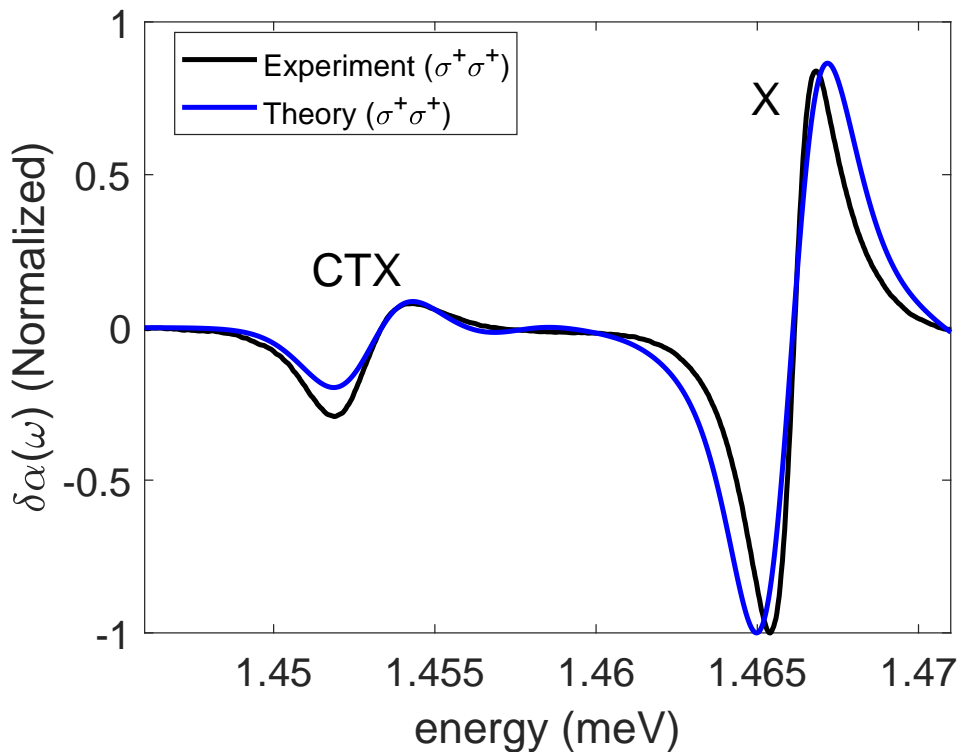
Figure 6.12: Measured and numerically calculated pump-induced differential absorption change $\delta\alpha$ for off-resonant excitation 5 meV below the spatially-indirect 1s heavy-hole CTX for co-circular excitation conditions. The model parameters are presented in Table A.1 (HH-V). The measurements were performed in the group of Sangam Chatterjee (University of Giessen).

The comparison between the measurement and theoretical result shows a good agreement. The obtained pump induced absorption change shows the expected optical Stark shifts on

the X resonance corresponding to a blue shift. Even the signatures appearing at the CTX shows a good agreement and thus can describe the new signatures observed at the CTX. For co-circularly polarized pulses the measured differential absorption appearing at the CTX show a slightly asymmetric blue shift. It corresponds a little more to pump-induced bleaching. Besides this fact the excitonic nonlinear response at the CTX is quite similar to the that of X. More significant differences occur for the case of counter-circular polarization conditions.
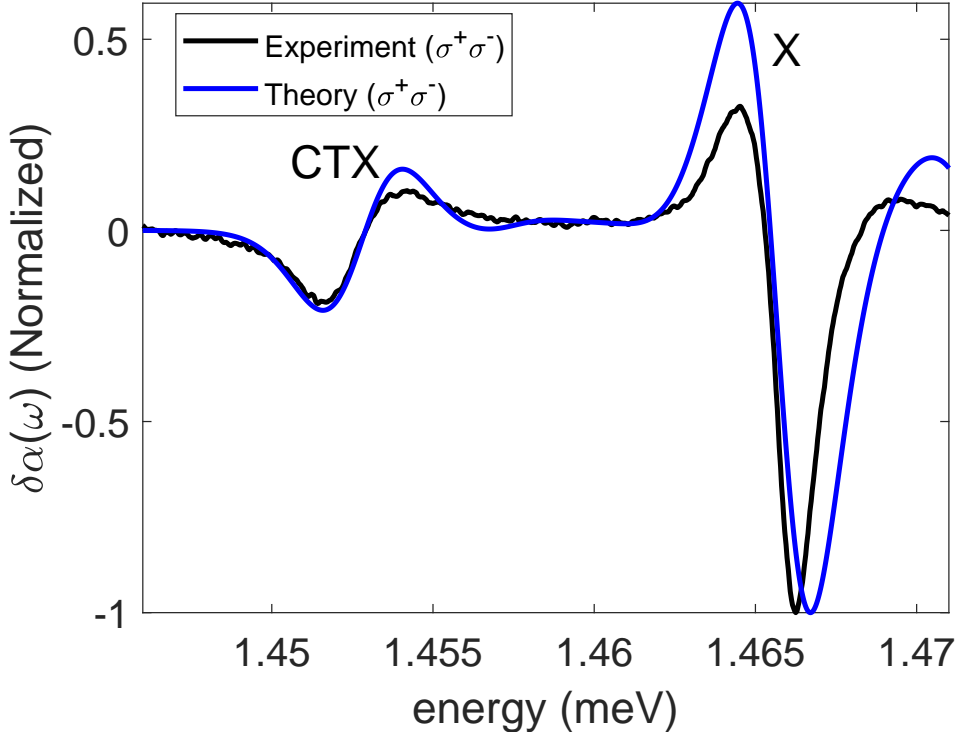
Figure 6.13: Measured and numerically calculated pump-induced differential absorption change $\delta\alpha$ for off-resonant excitation 5 meV below the spatially-indirect 1s heavy-hole CTX for counter-circular excitation conditions. The model parameters are presented in Table A.1 (HH-V). The measurements were performed in the group of Sangam Chatterjee (University of Giessen).

For counter-circularly excitation conditions, a red shift due to the presence of bound biexcitons occurs at the X. However, due to the first order Coulomb interaction, which is absent in type-I heterostructures, as mentioned and demonstrated in chapter 6.1.3, a blue shift is obtained at the CTX originating from CI_{1st} describing qualitatively well the unexpected signature at the CTX from the OPOP experiment.

In addition, our theoretical framework goes beyond the analysis of spectral characteristics and encompasses dynamic predictions within the coherent $\chi^{(3)}$-limit. Fig. 6.14 compares

the temporal behavior of observed optical Stark shifts between experiment and theory. Interestingly, our theory not only precisely captures the spectral properties when the pump and probe pulses perfectly overlap in time but also accurately describes the temporal evolution of the optical Stark shifts. Specifically, for pulses with co-circular polarization, see. Figs. 6.14(a) and (b), there is a good agreement between the experimental and theoretical dynamics of the optical Stark shift for both charge transfer excitons and direct excitons. Similarly, for pulses with counter-circular polarization, see. Fig. 6.14(c) and (d), we obtain a good agreement, especially in the dynamics of the CTX. However, in the case of direct excitons, this polarization configuration exhibits a delayed appearance of the red shift in the experimental results compared to the blue shift observed in the CTX resonance. It is important to note that this delayed occurrence of the red shift is not reflected in our theoretical predictions. When operating within the coherent $\chi^{(3)}$-limit in a PP setup, the excitonic nonlinear response at large delay times (τ) between the pump and probe pulses can not accordingly described. In particular, when investigating pump-induced differential absorption changes, positive delay times correspond to the probe pulse arriving after the pump pulse has already excited the system. At these positive delay times, the optical response is primarily governed by the excited states and population dynamics induced by the pump pulse. However, in the coherent $\chi^{(3)}$-limit, the description of pump-induced differential absorption changes becomes inadequate because the nonlinear response relies on the phase relationship between the pump and probe pulses. As the delay between the pulses increases, the coherence between the pump-induced excited states and the probe pulse diminishes. Consequently, the interaction between the pump-induced population changes and the probe pulse becomes intricate and incoherent. This loss of coherence hinders the accurate description of pump-induced differential absorption changes for positive delay times within the framework of the coherent $\chi^{(3)}$-limit model.
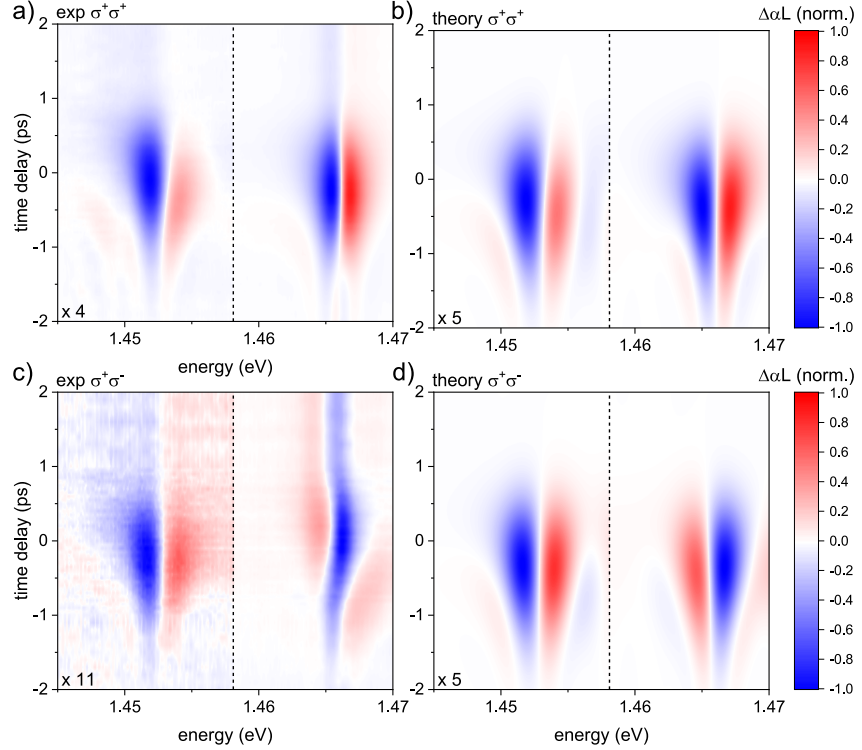
Figure 6.14: The differential absorption $\Delta\alpha$ spectrum in dependence of the time delay τ is shown. In (a) and (c) the measurement for co- and counter-circularly polarized laser pulses is displayed, respectively. The corresponding theoretical findings are shown in (b) and (d), respectively. The energy areas of the CTX (lower energies) and X (higher energies) are divided into two areas, indicated by a black line at 1.4581 eV for clarity. The model parameters are presented in Table A.1 (HH-V). Taken from [212].

6.4 Conclusions

In this chapter, we theoretically treat the Coulomb interaction beyond the TDHF approximation. We take into account many-body correlation effects, including the consideration of two-exciton coherences, to gain a more comprehensive understanding of the excitonic nonlinear optical response of spatially-direct type-I and spatially-indirect type-II excitons. In contrast to the previous chapters, we consider laser pulses that are either resonant or only slightly detuned from the excitonic resonances. Consequently, contributions originating from intraband excitations are negligible and are not taken into account, in contrast to the dominant high-order correlation effects.

We provide a theoretical analysis to reveal the new characteristic signatures appearing in an OPOP experiment for excitations below the CTX resonance, which only exists in type-II QW structures. We demonstrate the significant differences that occurs in the computed differential absorption spectrum depending on the polarization of the incident

laser pulses. Our results show that the nonlinear optical response for counter-circular excitation conditions exhibits additional contributions already on the Hartree-Fock level which can be well understood by our theoretical approach. The CI_{1st} interaction term, which introduces a coupling between the two spin subspaces, and only exists for spatially-inhomogeneous systems, is responsible for this feature. This finite contribution can be easily identified analytically by considering the corresponding equation of motion.

Summary $\quad\quad\quad\quad\quad\quad\quad\quad$ 7

In this thesis, we provide and establish microscopic descriptions to theoretically investigate the light-matter interaction in photoexcited semiconductors. In the first part of this work we focus on the nonlinear response when strong nonresonant laser pulses are used to excite the system. The second part of this thesis is dedicated to the influence of excitonic and many-body Coulomb correlation effects to the optical response of semiconductor nanostructures.

In our first theoretical investigation when we consider a four-wave mixing experiment performed with strongly nonresonant laser pulses. The interband current dominates the nonlinear response when solid-state systems are optically excited nearly resonant to the band gap energy of the material system. By comparing our theoretical findings between a simple two-level model and a two-band model, we clearly show that the interplay between interband and intraband excitations plays a crucial role in transient four-wave mixing when semiconductors are optically excited nonresonantly by electric fields with low frequencies. Our microscopic approach to include nonresonant excitations is based on the semiconductor Bloch equations. The intraband excitation is responsible for an acceleration of electrons and holes within their respective bands. The consideration of the latter creates additional excitation pathways leading to both destructive and constructive interferences between different contributions to the nonlinear response. Depending sensitively on the laser frequencies the four-wave mixing intensity spectrum exhibits a spectral broadening and additional complex signatures. Overall, our theoretical findings agree qualitatively well with the significant broadening observed in measured four-wave-mixing spectra of bulk semiconductors.

In our next topic, we focus on the collision dynamics between electrons and holes and their influence to the anisotropy of interband high-harmonic generation which for instance appears in many recently investigated solid-state systems like MgO. We are able to provide an unified real- and momentum-space picture which reveals the microscopic processes behind the scattering processes of electrons and holes with other atoms in solids. We demonstrate how the sub-cycle real space collision dynamics can be read out from the dynamics in momentum space and the band structure of the considered material system. Within our developed collision model, we provide a relation between the various scattering processes to van Hove singularities appearing at critical lines in the energy dispersion. Depending crucially on the polarization direction of the incident pulses forward or backward scattering processes give rise to an enhancing or a diminishing of the high harmonic emission. In addition, we demonstrate how the dynamics in solid high harmonic generation can be adjusted by accurately designed two-color pulses. Overall, our approach explains and provides theoretical predictions for several experiments like the anisotropic high

harmonic generation in MgO and the atomic-like recombination process in solid-state systems within a transparent picture.

In the context of high harmonic generation, we extend the semiconductor Bloch equation by including excitonic effects within a two-band model. In this case, the Coulomb interaction is treated in the time-dependent Hartree-Fock approximation. From previous theoretical investigations it is known that excitonic effects play only a minor role when extremely intense optical pulses are applied in the range of the band gap energy. As in the chapters before we again consider here laser pulses which are nonresonant with respect to the band gap energy. We explicitly apply incident electric fields in such way that an odd multiple of the laser frequencies correspond to the 1s exciton resonance energy. Consequently, we demonstrate that for such excitation conditions the high harmonic emission intensity is strongly enhanced in comparison to the case of non-interacting particles.

In the end of this thesis we treat the Coulomb interaction beyond the time-dependent Hartree-Fock approximation. In other words, we include many-body correlation effects, i.e., we consider two-exciton coherences. In contrast to the previous chapters, we apply laser pulses which are resonant or only slightly detuned with respect to the excitonic resonances. In this case, contributions originating from intraband excitations are negligible and do not need to be considered. We explicitly investigate the nonlinear optical response of spatially-direct type-I and spatially-indirect type-II quantum well excitons. We provide a theoretical study for an optical-pump optical-probe setup and demonstrate major differences occurring in the computed pump-induced differential absorption spectrum between such semiconductor nanostructures in dependence on the polarization directions of the incident laser fields. The numerical simulations clearly show that in type-II structures the nonlinear optical response for counter-circular excitation conditions is finite already on the Hartree-Fock level. The reason for this is the first-order Coulomb interaction term, which introduces a coupling between the two spin subspaces exits only for spatially-inhomogeneous systems. This finite contribution can be easily understood analytically considering the respective equations of motion. Measurements of optical-pump optical-probe spectra show characteristic signatures for excitations below the charge transfer exciton resonance in a type-II quantum well structure which are in agreement with our theory. In summary, our study demonstrates the crucial influence of many-body Coulomb correlations in the excitonic nonlinear response of semiconductor nanostructures and we highlight crucial differences between type-I and type-II systems.

The present work demonstrates promising results and provides impetus for further physical investigations in the aforementioned areas. The theoretical findings provided in this thesis shine light on various aspects of the light-matter interaction in photoexcited solid-state systems. Building upon the results described here, future studies in the following areas hold great potential for expanding our knowledge further. The insights gained from these future researches have the potential to pave the way for practical applications. For example, the development of compact solid-state light sources, based on the principles investigated here may be possible. Additionally, a deeper understanding of band structure imaging can

open new avenues for material characterization techniques, enabling advancements in areas such as materials science, device engineering, and nanotechnology.

Appendix

<div style="text-align: right">

A

</div>

A.1 Perturbative expansion with directional information

In this section, we present the process of extracting directional information for the relevant quantities for the PP setup. To illustrate this, we utilize the SBE. In the case of weak excitation intensities, the observables denoted as O can be expanded with respect to the power l in the electric field. When j pulses are applied, the decomposition takes the following structure:

$$O = \sum_{l=0}^{\infty} O^{(l)}, \quad \text{with} \quad O^{(l)} = \prod_{i=1}^{j} E_i^{l_i} \quad \text{and} \quad \sum_{i=1}^{j} l_i = l \tag{A.1}$$

An optical pulse propagating into the direction $\mathbf{k}_i$ can be described by

$$E_i = \tilde{E}_i e^{-i\mathbf{k}_i \cdot \mathbf{r}} + \tilde{E}_i^* e^{i\mathbf{k}_i \cdot \mathbf{r}}. \tag{A.2}$$

In this thesis we consider up to two laser pulses. Inserting eq. (A.2) into eq. (A.1) we get the following expansion:

$$O = \sum_{l=0}^{\infty} \sum_{|n|+|m| \le l} O^{(l)(n|m)}, \quad \text{where} \quad O^{(l)(n|m)} \propto e^{i(n\mathbf{k}_1 + m\mathbf{k}_2) \cdot \mathbf{r}} \tag{A.3}$$

In principle, we can decompose the quantities in terms of their $\mathbf{k}$-vectors and solve them in separate equations. When applying this expansion, one can select the desired order and direction of interest, and then formulate all the necessary equations to compute the dynamics.

A.1.1 Analysis of PP in third order

In chapter 6 for the case of PP experiments the nonlinear signal up to third order $\chi^{(3)}$ depends sensitively on the polarization directions of the applied laser pulses. The pump-induced absorption is measured into the direction of the probe pulse $\mathbf{k}_2$. We consider two incident pulses ($\mathbf{k}_1$ and $\mathbf{k}_2$) and use the rotating-wave approximation. Each pulse induces an interband coherence in the first order due to the linear source term $\mathbf{E}_i(t) \cdot \boldsymbol{\mu}^*$. The linear

equations of motion are

$$-i\hbar\frac{d}{dt}p_{12}^{vc(1)(1|0)} = -\sum_j T_{2j}^c p_{1j}^{vc(1)(1|0)} - \sum_i T_{i1}^v p_{i2}^{vc(1)(1|0)} + V_{12}^{vc} p_{12}^{vc(1)(1|0)} + \mathbf{E}_1(t) \cdot \left(\boldsymbol{\mu}_{12}^{vc}\right)^*,$$

$$-i\hbar\frac{d}{dt}p_{12}^{vc(1)(0|1)} = -\sum_j T_{2j}^c p_{1j}^{vc(1)(0|1)} - \sum_i T_{i1}^v p_{i2}^{vc(1)(0|1)} + V_{12}^{vc} p_{12}^{vc(1)(0|1)} + \mathbf{E}_2(t) \cdot \left(\boldsymbol{\mu}_{12}^{vc}\right)^*.$$

$$(A.4)$$

The only relevant quantity in second order is the two-exciton coherence B. Due to the fact that the PP signal within a third-order treatment is obtained into the direction $(0|1)$ it is only necessary to calculate the biexciton amplitude $\overline{B}^{(2)(1|1)}$:

$$-i\hbar\frac{d}{dt}\overline{B}_{ba12}^{v'c'vc(2)(1|1)} = -\sum_i \left(T_{2i}^{c'}\overline{B}_{ba1i}^{v'c'vc(2)(1|1)} + T_{i1}^{v'}\overline{B}_{bai2}^{v'c'vc(2)(1|1)} \right. \qquad (A.5)$$

$$+ T_{ai}^{c'}\overline{B}_{bi12}^{v'c'vc(2)(1|1)} + T_{ib}^{v'}\overline{B}_{ia12}^{v'c'vc(2)(1|1)} \Big)$$

$$+ \left(V_{ba}^{v'c'} + V_{b2}^{v'c} + V_{1a}^{vc'} + V_{12}^{vc} - V_{b1}^{v'v} - V_{a2}^{c'c}\right)\overline{B}_{ba12}^{v'c'vc(2)(1|1)}$$

$$- \left(V_{ba}^{v'c'} + V_{12}^{vc} - V_{b1}^{v'v} - V_{a2}^{c'c}\right)\left(p_{1a}^{vc'(1)(1|0)} p_{b2}^{v'c(1)(0|1)} + p_{1a}^{vc'(1)(0|1)} p_{b2}^{v'c(1)(1|0)}\right)$$

$$+ \left(V_{1a}^{vc'} + V_{b2}^{v'c} - V_{b1}^{v'v} - V_{a2}^{c'c}\right)\left(p_{ba}^{v'c'(1)(1|0)} p_{12}^{vc(1)(0|1)} + p_{ba}^{v'c'(1)(0|1)} p_{12}^{vc(1)(1|0)}\right)$$

The differential single exciton amplitude ($\propto |E_2|^2 E_1$) in third-order into the direction $\mathbf{k}_2$ is provided by considering all lower-order source contributions.

$$-i\hbar\frac{d}{dt}\delta p_{12}^{vc(3)(0|1)} = -\sum_j T_{2j}^c \delta p_{1j}^{vc(3)(0|1)} - \sum_i T_{i1}^v \delta p_{i2}^{vc(3)(0|1)} + V_{12}^{vc}\delta p_{12}^{vc(3)(0|1)}$$

$$+ \mathbf{E}_1(t) \cdot \left[-\sum_{abv'c'}\left(\left(\boldsymbol{\mu}_{1b}^{vc'}\right)^*\left(p_{ab}^{v'c'(1)(1|0)}\right)^* p_{a2}^{v'c_2(1)(0|1)} + \left(\boldsymbol{\mu}_{b2}^{v'c}\right)^*\left(p_{ba}^{v'c'(1)(1|0)}\right)^* p_{1a}^{vc'(1)(0|1)}\right)\right]$$

$$+ \mathbf{E}_2(t) \cdot \left[-\sum_{abv'c'}\left(\left(\boldsymbol{\mu}_{1b}^{vc'}\right)^*\left(p_{ab}^{v'c'(1)(1|0)}\right)^* p_{a2}^{v'c(1)(1|0)} + \left(\boldsymbol{\mu}_{b2}^{v'c}\right)^*\left(p_{ba}^{v'c'(1)(1|0)}\right)^* p_{1a}^{vc'(1)(1|0)}\right)\right]$$

$$+ \sum_{abv'c'}\left(V_{a2}^{c'c} - V_{a1}^{c'v} - V_{b2}^{v'c} + V_{b1}^{v'v}\right) \times$$

$$\left[(p_{ba}^{v'c'(1)(1|0)})^*\left(p_{b2}^{v'c(1)(1|0)} p_{1a}^{vc'(1)(0|1)} + p_{b2}^{v'c(1)(0|1)} p_{1a}^{vc'(1)(1|0)}\right)\right.$$

$$- (p_{ba}^{v'c'(1)(1|0)})^*\left(p_{ba}^{v'c'(1)(1|0)} p_{12}^{vc(1)(0|1)} + p_{ba}^{v'c'(1)(0|1)} p_{12}^{vc(1)(1|0)}\right)$$

$$- (p_{ba}^{v'c'(1)(1|0)})^*\overline{B}_{ba12}^{v'c'vc(2)(1|1)}\Big]$$

$$(A.6)$$

The closed set of equations (A.1)-(A.3) are numerically solved in order to calculate the pump-induced absorption which is determined by the differential polarization $\delta p_{12}^{vc(3)(0|1)}$. The latter contains three nonlinearities including Pauli blocking (PB), the first (CI_{1st}) and higher-order (CI_{corr}) Coulomb interaction terms. They can separately be analyzed by the equations:

$$-i\hbar\frac{d}{dt}\delta p_{12,PB}^{vc(3)(0|1)} = -\sum_j T_{2j}^c\delta p_{1j,PB}^{vc(3)(0|1)} - \sum_i T_{i1}^v\delta p_{i2,PB}^{vc(3)(0|1)} + V_{12}^{vc}\delta p_{12,PB}^{vc(3)(0|1)} \tag{A.7}$$

$$+ \mathbf{E}_1(t)\cdot\left[-\sum_{abv'c'}\left(\left(\boldsymbol{\mu}_{1b}^{vc'}\right)^*\left(p_{ab}^{v'c'(1)(1|0)}\right)^*p_{a2}^{v'c_2(1)(0|1)} + \left(\boldsymbol{\mu}_{b2}^{v'c}\right)^*\left(p_{ba}^{v'c'(1)(1|0)}\right)^*p_{1a}^{vc'(1)(0|1)}\right)\right]$$

$$+ \mathbf{E}_2(t)\left[-\sum_{abv'c'}\left(\left(\boldsymbol{\mu}_{1b}^{vc'}\right)^*\left(p_{ab}^{v'c'(1)(1|0)}\right)^*p_{a2}^{v'c(1)(1|0)} + \left(\boldsymbol{\mu}_{b2}^{v'c}\right)^*\left(p_{ba}^{v'c'(1)(1|0)}\right)^*p_{1a}^{vc'(1)(1|0)}\right)\right]$$

$$-i\hbar\frac{d}{dt}\delta p_{12,CI_{1st}}^{vc(3)(0|1)} = -\sum_j T_{2j}^c\delta p_{1j,CI_{1st}}^{vc(3)(0|1)} - \sum_i T_{i1}^v\delta p_{i2,CI_{1st}}^{vc(3)(0|1)} + V_{12}^{vc}\delta p_{12,CI_{1st}}^{vc(3)(0|1)} \tag{A.8}$$

$$+ \sum_{abv'c'}\left(V_{a2}^{c'c} - V_{a1}^{c'v} - V_{b2}^{v'c} + V_{b1}^{v'v}\right)\times$$

$$\left[(p_{ba}^{v'c'(1)(1|0)})^*\left(p_{b2}^{v'c(1)(1|0)}p_{1a}^{vc'(1)(0|1)} + p_{b2}^{v'c(1)(0|1)}p_{1a}^{vc'(1)(1|0)}\right)\right.$$

$$\left.- (p_{ba}^{v'c'(1)(1|0)})^*\left(p_{ba}^{v'c'(1)(1|0)}p_{12}^{vc(1)(0|1)} + p_{ba}^{v'c'(1)(0|1)}p_{12}^{vc(1)(1|0)}\right)\right]$$

$$-i\hbar\frac{d}{dt}\delta p_{12,CI_{corr}}^{vc(3)(0|1)} = -\sum_j T_{2j}^c\delta p_{1j,CI_{corr}}^{vc(3)(0|1)} - \sum_i T_{i1}^v\delta p_{i2,CI_{corr}}^{vc(3)(0|1)} + V_{12}^{vc}\delta p_{12,CI_{corr}}^{vc(3)(0|1)} \tag{A.9}$$

$$+ \sum_{abv'c'}\left(V_{a2}^{c'c} - V_{a1}^{c'v} - V_{b2}^{v'c} + V_{b1}^{v'v}\right)\left[-(p_{ba}^{v'c'(1)(1|0)})^*\overline{B}_{ba12}^{v'c'vc(2)(1|1)}\right]$$

A.2 Model parameters for the numerical solutions of the SBE in the coherent $\chi^{(3)}$−limit

Parameter	HH-I	HH-II	HH-III	HH-IV	HH-V
N_{Sites}	10	10	16	16	16
$\mu_{\text{Type−I}}$	1	1	1	1	1
$\mu_{\text{Type−II}}$	-	0.5	0.5	0.5	0.4
J^e	15 meV	15 meV	14 meV	14 meV	14 meV
J^{hh}	1.5 meV	1.5 meV	0.7 meV	0.7 meV	0.7 meV
U_0	15 meV	15 meV	8.3 meV	8.3 meV	8.3 meV
a_0^X/d	0.5	0.5	0.5	0.5	0.5
a_0^{CTX}/d	-	0.56	0.52	0.56	0.72
T_p^X	3 ps	3 ps	3 ps	3 ps	0.8 ps
T_p^{CTX}	-	3 ps	3 ps	3 ps	4 ps

Table A.1: The parameters of the one-dimensional tight binding model are shown which are used to calculate the differential polarization $\delta p^{(3)(0|1)}$ in chapter 6. The electronic couplings are given by J^v and J^c for the heavy-holes and the electrons, respectively. The relative strength of the optical dipole matrix element is described by $\mu_{\text{Type−I/Type−II}}$. The number of sites is given by N_{Sites}. The strength of the Coulomb interaction is indicated by U_0, where the spatial regularization is given by a_0^{vc}/d. The dephasing times of the excitons X and CTX is given by T_p^X and T_p^{CTX}, respectively. Here, the dephasing of the biexciton T_B is given by $T_B = \frac{T_p}{2}$.

Bibliography B

[1] H. Wong and H. Iwai, The road to miniaturization, Phys. World **18**, 40 (2005).

[2] H. Haug and S. W. Koch, *Quantum Theory of the Optical and Electronic Properties of Semiconductors*, 5th ed. (World Scientific, Singapore, 2009).

[3] F. Bloch, Über die Quantenmechanik der Elektronen in Kristallgittern, Z. Phys. **52**, 555 (1929).

[4] C. Zener, A Theory of the Electrical Breakdown of Solid Dielectics, Proc. Roy. Soc. A **145**, 523 (1934).

[5] P. A. Franken, A. E. Hill, C. W. Peters, and G. Weinreich, Generation of optical harmonics, Phys. Rev. Lett. **7**, 118 (1961).

[6] R. W. Boyd, *Nonlinear Optics*, 3rd ed. (Academic Press, San Diego, 2008).

[7] A. H. Zewail, Laser femtochemistry, Science **242**, 1645 (1988).

[8] D. S. Chemla and J. Shah, Many-body and correlation effects in semiconductors, Nature **411**, 549 (2001).

[9] S. Neppl, R. Ernstorfer, A. L. Cavalieri, C. Lemell, G. Wachter, E. Magerl, E. M. Bothschafter, M. Jobst, M. Hofstetter, U. Kleineberg, J. V. Barth, D. Menzel, J. Burgdörfer, P. Feulner, F. Krausz, and R. Kienberger, Direct observation of electron propagation and dielectric screening on the atomic length scale, Nature **517**, 342 (2015).

[10] L. Gremillet, F. Amiranoff, S. D. Baton, J.-C. Gauthier, M. Koenig, E. Martinolli, F. Pisani, G. Bonnaud, C. Lebourg, C. Rousseaux, C. Toupin, A. Antonicci, D. Batani, A. Bernardinello, T. Hall, D. Scott, P. Norreys, H. Bandulet, and H. Pépin, Time-resolved observation of ultrahigh intensity laser-produced electron jets propagating through transparent solid targets, Phys. Rev. Lett. **83**, 5015 (1999).

[11] W. Sha, T. B. Norris, W. J. Schaff, and K. E. Meyer, Time-resolved ballistic acceleration of electrons in a GaAs quantum-well structure, Phys. Rev. Lett. **67**, 2553 (1991).

[12] E. A. Shaner and S. A. Lyon, Picosecond time-resolved two-dimensional ballistic electron transport, Phys. Rev. Lett. **93**, 037402 (2004).

[13] L. Schultheis, M. D. Sturge, and J. Hegarty, Photon echoes from two-dimensional excitons in GaAs-AlGaAs quantum wells, Appl. Phys. Lett. **47**, 995 (1985).

[14] L. Schultheis, J. Kuhl, A. Honold, and C. W. Tu, Ultrafast phase relaxation of excitons via exciton-exciton and exciton-electron collisions, Phys. Rev. Lett. **57**, 1635 (1986).

[15] E. O. Göbel, K. Leo, T. C. Damen, J. Shah, S. Schmitt-Rink, W. Schäfer, J. F. Müller, and K. Köhler, Quantum beats of excitons in quantum wells, Phys. Rev. Lett. **64**, 1801 (1990).

[16] M. Wegener, D. S. Chemla, S. Schmitt-Rink, and W. Schäfer, Line shape of time-resolved four-wave mixing, Phys. Rev. A **42**, 5675 (1990).

[17] M. Lindberg, R. Binder, and S. W. Koch, Theory of the semiconductor photon echo, Phys. Rev. A **45**, 1865 (1992).

[18] M. Koch, J. Feldmann, G. von Plessen, E. O. Göbel, P. Thomas, and K. Köhler, Quantum beats versus polarization interference: An experimental distinction, Phys. Rev. Lett. **69**, 3631 (1992).

[19] K. Leo, J. Shah, T. Damen, A. Schulze, T. Meier, S. Schmitt-Rink, P. Thomas, E. Gobel, S. Chuang, M. Luo, W. Schafer, K. Kohler, and P. Ganser, Dissipative dynamics of an electronic wavepacket in a semiconductor double well potential, IEEE J. of Quantum Electron **28**, 2498 (1992).

[20] K.-H. Pantke, P. Schillak, B. S. Razbirin, V. G. Lyssenko, and J. M. Hvam, Nonlinear quantum beats of propagating polaritons, Phys. Rev. Lett. **70**, 327 (1993).

[21] R. Hellmann, M. Koch, J. Feldmann, S. T. Cundiff, E. O. Göbel, D. R. Yakovlev, A. Waag, and G. Landwehr, Homogeneous linewidth of excitons in semimagnetic CdTe/Cd$_{1-x}$Mn$_x$Te multiple quantum wells, Phys. Rev. B **48**, 2847 (1993).

[22] A. Lohner, K. Rick, P. Leisching, A. Leitenstorfer, T. Elsaesser, T. Kuhn, F. Rossi, and W. Stolz, Coherent optical polarization of bulk GaAs studied by femtosecond photon-echo spectroscopy, Phys. Rev. Lett. **71**, 77 (1993).

[23] D. S. Kim, J. Shah, T. C. Damen, L. N. Pfeiffer, and W. Schäfer, Femtosecond time-resolved four-wave mixing from biexcitons in GaAs quantum wells: dominance of the interaction-induced signal, Phys. Rev. B **50**, 5775 (1994).

[24] F. Jahnke, M. Koch, T. Meier, J. Feldmann, W. Schäfer, P. Thomas, S. W. Koch, E. Göbel, and H. Nickel, Simultaneous influence of disorder and Coulomb interaction on photon echoes in semiconductors, Phys. Rev. B **50**, 8114 (1994).

[25] S. T. Cundiff, M. Koch, W. H. Knox, J. Shah, and W. Stolz, Optical coherence in semiconductors: Strong emission mediated by nondegenerate interactions, Phys. Rev. Lett. **77**, 1107 (1996).

[26] M. Koch, J. Shah, and T. Meier, Coupled absorber-cavity system: Observation of a characteristic nonlinear response, Phys. Rev. B **57**, R2049 (1998).

[27] R. A. Kaindl, S. Lutgen, M. Woerner, T. Elsaesser, B. Nottelmann, V. M. Axt, T. Kuhn, A. Hase, and H. Künzel, Ultrafast dephasing of coherent intersubband polarizations in a quasi-two-dimensional electron plasma, Phys. Rev. Lett. **80**, 3575 (1998).

[28] P. Borri, W. Langbein, J. Mørk, J. M. Hvam, F. Heinrichsdorff, M.-H. Mao, and D. Bimberg, Dephasing in InAs/GaAs quantum dots, Phys. Rev. B **60**, 7784 (1999).

[29] M. Buck, L. Wischmeier, S. Schumacher, G. Czycholl, F. Jahnke, T. Voss, I. Rückmann, and J. Gutowski, Light-polarization and intensity dependence of higher-order nonlinearities in excitonic FWM signals, Eur. Phys. J. B **42**, 175 (2004).

[30] M. Stein, C. Lammers, P.-H. Richter, C. Fuchs, W. Stolz, M. Koch, O. Vänskä, M. J. Weseloh, M. Kira, and S. W. Koch, Dynamics of charge-transfer excitons in type-ii semiconductor heterostructures, Phys. Rev. B **97**, 125306 (2018).

[31] T. Yajima and Y. Taira, Spatial Optical Parametric Coupling of Picosecond Light Pulses and Transverse Relaxation Effect in Resonant Media, J. Phys. Soc. Jpn. **47**, 1620 (1979).

[32] S. Weiser, T. Meier, J. Möbius, A. Euteneuer, E. J. Mayer, W. Stolz, M. Hofmann, W. W. Rühle, P. Thomas, and S. W. Koch, Disorder-induced dephasing in semiconductors, Phys. Rev. B **61**, 13088 (2000).

[33] P. Kner, W. Schäfer, R. Lövenich, and D. S. Chemla, Coherence of four-particle correlations in semiconductors, Phys. Rev. Lett. **81**, 5386 (1998).

[34] K. J. Schafer and K. C. Kulander, High harmonic generation from ultrafast pump lasers, Phys. Rev. Lett. **78**, 638 (1997).

[35] P. B. Corkum and F. Krausz, Attosecond science, Nat. Phys. **3**, 381 (2007).

[36] A. McPherson, G. Gibson, H. Jara, U. Johann, T. S. Luk, I. A. McIntyre, K. Boyer, and C. K. Rhodes, Studies of multiphoton production of vacuum-ultraviolet radiation in the rare gases, J. Opt. Soc. Am. B **4**, 595 (1987).

[37] M. Ferray, A. L'Huillier, X. F. Li, L. A. Lompre, G. Mainfray, and C. Manus, Multiple-harmonic conversion of 1064 nm radiation in rare gases, J. Phys. B **21**, L31 (1988).

[38] X. F. Li, A. L'Huillier, M. Ferray, L. A. Lompré, and G. Mainfray, Multiple-harmonic generation in rare gases at high laser intensity, Phys. Rev. A **39**, 5751 (1989).

[39] N. Sarukura, K. Hata, T. Adachi, R. Nodomi, M. Watanabe, and S. Watanabe, Coherent soft-x-ray generation by the harmonics of an ultrahigh-power KrF laser, Phys. Rev. A **43**, 1669 (1991).

[40] J. K. Crane, M. D. Perry, S. Herman, and R. W. Falcone, High-field harmonic generation in helium, Opt. Lett. **17**, 1256 (1992).

[41] K. Miyazaki and H. Sakai, High-order harmonic generation in rare gases with intense subpicosecond dye laser pulses, J. Phys. B **25**, L83 (1992).

[42] C. M. Heyl, J. Güdde, A. L'Huillier, and U. Höfer, High-order harmonic generation with μj laser pulses at high repetition rates, J. Phys. B **45**, 074020 (2012).

[43] J. J. Macklin, J. D. Kmetec, and C. L. Gordon, High-order harmonic generation using intense femtosecond pulses, Phys. Rev. Lett. **70**, 766 (1993).

[44] A. L'Huillier and P. Balcou, High-order harmonic generation in rare gases with a 1-ps 1053-nm laser, Phys. Rev. Lett. **70**, 774 (1993).

[45] Z. Chang, A. Rundquist, H. Wang, M. M. Murnane, and H. C. Kapteyn, Generation of coherent soft X rays at 2.7 nm using high harmonics, Phys. Rev. Lett. **79**, 2967 (1997).

[46] M. Schnürer, C. Spielmann, P. Wobrauschek, C. Streli, N. H. Burnett, C. Kan, K. Ferencz, R. Koppitsch, Z. Cheng, T. Brabec, and F. Krausz, Coherent 0.5-keV x-ray emission from helium driven by a sub-10-fs laser, Phys. Rev. Lett. **80**, 3236 (1998).

[47] S. Ghimire, A. D. DiChiara, E. Sistrunk, P. Agostini, L. F. DiMauro, and D. A. Reis, Observation of high-order harmonic generation in a bulk crystal, Nat. Phys. **7**, 138 (2011).

[48] S. Ghimire, G. Ndabashimiye, A. D. DiChiara, E. Sistrunk, M. I. Stockman, P. Agostini, L. F. DiMauro, and D. A. Reis, Strong-field and attosecond physics in solids, J. Phys. B **47**, 204030 (2014).

[49] G. Vampa, T. J. Hammond, N. Thiré, B. E. Schmidt, F. Légaré, C. R. McDonald, T. Brabec, and P. B. Corkum, Linking high harmonics from gases and solids, Nature **522**, 462 (2015).

[50] T. T. Luu, M. Garg, S. Y. Kruchinin, A. Moulet, M. T. Hassan, and E. Goulielmakis, Extreme ultraviolet high-harmonic spectroscopy of solids, Nature **521**, 498 (2015).

[51] G. Ndabashimiye, S. Ghimire, M. Wu, D. A. Browne, K. J. Schafer, M. B. Gaarde, and D. A. Reis, Solid-state harmonics beyond the atomic limit, Nature **534**, 520 (2016).

[52] X. Song, S. Yang, R. Zuo, T. Meier, and W. Yang, Enhanced high-order harmonic generation in semiconductors by excitation with multicolor pulses, Phys. Rev. A **101**, 033410 (2020).

[53] X. Song, R. Zuo, S. Yang, P. Li, T. Meier, and W. Yang, Attosecond temporal confinement of interband excitation by intraband motion, Opt. Express **27**, 2225 (2019).

[54] A. Trautmann, R. Zuo, G. Wang, W.-R. Hannes, S. Yang, L. H. Thong, C. Ngo, J. T. Steiner, M. Ciappina, M. Reichelt, H. T. Duc, X. Song, W. Yang, and T. Meier, Microscopic simulations of high harmonic generation from semiconductors, Proc. SPIE **11999**, 1199909 (2022).

[55] J. Hader, J. Neuhaus, J. V. Moloney, and S. W. Koch, Coulomb enhancement of high harmonic generation in monolayer transition metal dichalcogenides, Opt. Lett. **48**, 2094 (2023).

[56] T. Meier, P. Thomas, and S. W. Koch, *Coherent Semiconductor Optics: From Basic Concepts to Nanostructure Applications* (Springer, New York, 2007).

[57] C. Sieh, T. Meier, F. Jahnke, A. Knorr, S. W. Koch, P. Brick, M. Hübner, C. Ell, J. Prineas, G. Khitrova, and H. M. Gibbs, Coulomb memory signatures in the excitonic optical Stark effect, Phys. Rev. Lett. **82**, 3112 (1999).

[58] H. Wang, K. Ferrio, D. G. Steel, Y. Z. Hu, R. Binder, and S. W. Koch, Transient nonlinear optical response from excitation induced dephasing in GaAs, Phys. Rev. Lett. **71**, 1261 (1993).

[59] C. Gros and R. Valentí, Cluster expansion for the self-energy: A simple many-body method for interpreting the photoemission spectra of correlated Fermi systems, Phys. Rev. B **48**, 418 (1993).

[60] V. M. Axt and A. Stahl, A dynamics-controlled truncation scheme for the hierarchy of density matrices in semiconductor optics, Z. Phys. **93**, 195 (1994).

[61] V. M. Axt and A. Stahl, The role of the biexciton in a dynamic density matrix theory of the semiconductor band edge, Z. Phys. **93**, 205 (1994).

[62] M. Lindberg, Y. Z. Hu, R. Binder, and S. W. Koch, $\chi^{(3)}$ Formalism in optically excited semiconductors and its applications in four-wave-mixing spectroscopy, Phys. Rev. B **50**, 18060 (1994).

[63] W. Schäfer, D. S. Kim, J. Shah, T. C. Damen, J. E. Cunningham, K. W. Goossen, L. N. Pfeiffer, and K. Köhler, Femtosecond coherent fields induced by many-particle correlations in transient four-wave mixing, Phys. Rev. B **53**, 16429 (1996).

[64] L. Schultheis, A. Honold, J. Kuhl, K. Köhler, and C. W. Tu, Optical dephasing of homogeneously broadened two-dimensional exciton transitions in GaAs quantum wells, Phys. Rev. B **34**, 9027 (1986).

[65] E. O. Göbel, K. Leo, T. C. Damen, J. Shah, S. Schmitt-Rink, W. Schäfer, J. F. Müller, and K. Köhler, Quantum beats of excitons in quantum wells, Phys. Rev. Lett. **64**, 1801 (1990).

[66] D.-S. Kim, J. Shah, J. E. Cunningham, T. C. Damen, W. Schäfer, M. Hartmann, and S. Schmitt-Rink, Giant excitonic resonance in time-resolved four-wave mixing in quantum wells, Phys. Rev. Lett. **68**, 1006 (1992).

[67] S. Schmitt-Rink and D. S. Chemla, Collective excitations and the dynamical Stark effect in a coherently driven exciton system, Phys. Rev. Lett. **57**, 2752 (1986).

[68] D. Fröhlich, A. Nöthe, and K. Reimann, Observation of the resonant Optical Stark effect in a semiconductor, Phys. Rev. Lett. **55**, 1335 (1985).

[69] A. Mysyrowicz, D. Hulin, A. Antonetti, A. Migus, W. T. Masselink, and H. Morko ç, "dressed excitons" in a multiple-quantum-well structure: Evidence for an Optical Stark effect with femtosecond response time, Phys. Rev. Lett. **56**, 2748 (1986).

[70] A. V. Lehmen, D. S. Chemla, J. E. Zucker, and J. P. Heritage, Optical Stark effect on excitons in GaAs quantum wells, Opt. Lett. **11**, 609 (1986).

[71] B. Fluegel, N. Peyghambarian, G. Olbright, M. Lindberg, S. W. Koch, M. Joffre, D. Hulin, A. Migus, and A. Antonetti, Femtosecond studies of coherent transients in semiconductors, Phys. Rev. Lett. **59**, 2588 (1987).

[72] G. Noll, U. Siegner, S. G. Shevel, and E. O. Göbel, Picosecond stimulated photon echo due to intrinsic excitations in semiconductor mixed crystals, Phys. Rev. Lett. **64**, 792 (1990).

[73] K. Leo, M. Wegener, J. Shah, D. S. Chemla, E. O. Göbel, T. C. Damen, S. Schmitt-Rink, and W. Schäfer, Effects of coherent polarization interactions on time-resolved degenerate four-wave mixing, Phys. Rev. Lett. **65**, 1340 (1990).

[74] M. D. Webb, S. T. Cundiff, and D. G. Steel, Stimulated-picosecond-photon-echo studies of localized exciton relaxation and dephasing in GaAs/Al$_x$Ga$_{1-x}$As multiple quantum wells, Phys. Rev. B **43**, 12658 (1991).

[75] S. T. Cundiff, H. Wang, and D. G. Steel, Polarization-dependent picosecond excitonic nonlinearities and the complexities of disorder, Phys. Rev. B **46**, 7248 (1992).

[76] M. Kira and S. W. Koch, Many-body correlations and excitonic effects in semiconductor spectroscopy, Prog. Quantum. Electron. **30**, 155 (2006).

[77] M. Kira and S. W. Koch, *Semiconductor quantum optics* (Cambridge University Press, Cambridge, 2012).

[78] D. Golde, Microscopic investigations of the terahertz and the extreme nonlinear optical response of semiconductors, Philipps-Universität Marburg, PhD Dissertation (2010).

[79] U. Huttner, Theoretical analysis of ultrafast strong terahertz-field effects in semiconductors, Philipps-Universität Marburg, PhD Dissertation (2016).

[80] H. T. Duc, C. Ngo, and T. Meier, Ballistic photocurrents in semiconductor quantum wells caused by the excitation of asymmetric excitons, Phys. Rev. B **100**, 045308 (2019).

[81] O. Schubert, M. Hohenleutner, F. Langer, B. Urbanek, C. Lange, U. Huttner, D. Golde, T. Meier, M. Kira, S. W. Koch, and R. Huber, Sub-cycle control of terahertz high-harmonic generation by dynamical Bloch oscillations, Nat. Photonics **8**, 119 (2014).

[82] C. Kittel, *Quantum Theory of Solids* (Wiley, New York, 1963).

[83] D. Golde, T. Meier, and S. W. Koch, High harmonics generated in semiconductor nanostructures by the coupled dynamics of optical inter- and intraband excitations, Phys. Rev. B **77**, 075330 (2008).

[84] D. Golde, M. Kira, T. Meier, and S. W. Koch, Microscopic theory of the extremely nonlinear terahertz response of semiconductors, Phys. Status Solidi B **248**, 863 (2011).

[85] D. Golde, T. Meier, and S. W. Koch, Microscopic analysis of extreme nonlinear optics in semiconductor nanostructures, J. Opt. Soc. Am. B **23**, 2559 (2006).

[86] D. Golde, T. Meier, and S. W. Koch, "Modeling of the extreme nonlinear optical response of semiconductor nanostructures", in Ultrafast phenomena xv, edited by P. Corkum, D. M. Jonas, R. J. D. Miller, and A. M. Weiner (2007), p. 689.

[87] D. Golde, T. Meier, and S. W. Koch, Microscopic analysis of high-harmonic generation in semiconductor nanostructures, Phys. Status Solidi C **6**, 420 (2009).

[88] D. Golde, M. Kira, and S. W. Koch, Terahertz response of a two-dimensional electron gas, Proc. SPIE **6892**, 68921F (2008).

[89] S. Chatterjee, T. Grunwald, D. Köhler, K. Pierz, D. Golde, M. Kira, and S. W. Koch, Thz measurements of the optical response in a two-dimensional electron gas, Phys. Status Solidi C **6**, 453 (2009).

[90] D. Golde, M. Wagner, D. Stehr, H. Schneider, M. Helm, A. M. Andrews, T. Roch, G. Strasser, M. Kira, and S. W. Koch, Fano signatures in the intersubband terahertz response of optically excited semiconductor quantum wells, Phys. Rev. Lett. **102**, 127403 (2009).

[91] M. Wagner, D. Golde, D. Stehr, H. Schneider, M. Helm, A. Andrews, T. Roch, G. Strasser, M. Kira, and S. W. Koch, Fano profile in the intersubband terahertz response of photoexcited GaAs/AlGaAs quantum wells, J. Phys. Conf. Ser. **193**, 012073 (2009).

[92] D. Golde, M. Kira, and S. W. Koch, Ultrafast terahertz response of optically excited semiconductor heterostructures, Proc. SPIE **7600**, 76000F (2010).

[93] F. Schwabl, *Quantenmechanik (QM I): Eine Einführung*, 7th ed. (Springer, Berlin, 2007).

[94] H. W. Wyld and B. D. Fried, Quantum mechanical kinetic equations, Ann. Phys. **23**, 374 (1963).

[95] J. Fricke, Transport equations including many-particle correlations for an arbitrary quantum system: A general formalism, Ann. Phys. **252**, 479 (1996).

[96] M. Kira, F. Jahnke, and S. W. Koch, Microscopic theory of excitonic signatures in semiconductor photoluminescence, Phys. Rev. Lett. **81**, 3263 (1998).

[97] M. Kira, W. Hoyer, T. Stroucken, and S. W. Koch, Exciton formation in semiconductors and the influence of a photonic environment, Phys. Rev. Lett. **87**, 176401 (2001).

[98] G. D. Purvis and R. J. Bartlett, A full coupled-cluster singles and doubles model: The inclusion of disconnected triples, J. Chem. Phys. **76**, 1910 (1982).

[99] W. Hoyer, M. Kira, and S. W. Koch, Influence of coulomb and phonon interaction on the exciton formation dynamics in semiconductor heterostructures, Phys. Rev. B **67**, 155113 (2003).

[100] M. Kira, W. Hoyer, and S. W. Koch, Terahertz signatures of the exciton formation dynamics in non-resonantly excited semiconductors, Solid State Commun. **129**, 733 (2004).

[101] M. Kira and S. W. Koch, Exciton-population inversion and terahertz gain in semiconductors excited to resonance, Phys. Rev. Lett. **93**, 076402 (2004).

[102] M. Kira and S. W. Koch, Quantum-optical spectroscopy of semiconductors, Phys. Rev. A **73**, 013813 (2006).

[103] M. Kira and S. W. Koch, Cluster-expansion representation in quantum optics, Phys. Rev. A **78**, 022102 (2008).

[104] M. Hohenleutner, F. Langer, O. Schubert, M. Knorr, U. Huttner, S. W. Koch, M. Kira, and R. Huber, Real-time observation of interfering crystal electrons in high-harmonic generation, Nature **523**, 572 (2015).

[105] A. Brown, W. J. Meath, and P. Tran, Rotating-wave approximation for the interaction of a pulsed laser with a two-level system possessing permanent dipole moments, Phys. Rev. A **63**, 013403 (2000).

[106] M. J. Lighthill and H. S. Holdgrün, *Einführung in die Theorie der Fourieranalysis und der verallgemeinerten Funktionen* (Bibliogr. Inst., Mannheim, 1966).

[107] S. T. Cundiff, Coherent spectroscopy of semiconductors, Opt. Express **16**, 4639 (2008).

[108] B. L. Wilmer, F. Passmann, M. Gehl, G. Khitrova, and A. D. Bristow, Multidimensional coherent spectroscopy of a semiconductor microcavity, Phys. Rev. B **91**, 201304 (2015).

[109] M. Lindberg and S. W. Koch, Effective Bloch equations for semiconductors, Phys. Rev. B **38**, 3342 (1988).

[110] B. F. Feuerbacher, J. Kuhl, and K. Ploog, Biexcitonic contribution to the degenerate-four-wave-mixing signal from a GaAs/Al$_x$Ga$_{1-x}$As quantum well, Phys. Rev. B **43**, 2439 (1991).

[111] S. Bar-Ad and I. Bar-Joseph, Exciton spin dynamics in GaAs heterostructures, Phys. Rev. Lett. **68**, 349 (1992).

[112] D. J. Lovering, R. T. Phillips, G. J. Denton, and G. W. Smith, Resonant generation of biexcitons in a GaAs quantum well, Phys. Rev. Lett. **68**, 1880 (1992).

[113] K. Bott, O. Heller, D. Bennhardt, S. T. Cundiff, P. Thomas, E. J. Mayer, G. O. Smith, R. Eccleston, J. Kuhl, and K. Ploog, Influence of exciton-exciton interactions on the coherent optical response in GaAs quantum wells, Phys. Rev. B **48**, 17418 (1993).

[114] J.-Y. Bigot, A. Daunois, J. Oberlé, and J.-C. Merle, Femtosecond dephasing in CdS$_x$Se$_{1-x}$ mixed crystals: The role of localized biexcitons, Phys. Rev. Lett. **71**, 1820 (1993).

[115] K.-H. Pantke, D. Oberhauser, V. G. Lyssenko, J. M. Hvam, and G. Weimann, Coherent generation and interference of excitons and biexcitons in GaAs/Al$_x$Ga$_{1-x}$As quantum wells, Phys. Rev. B **47**, 2413 (1993).

[116] E. Mayer, G. Smith, V. Heuckeroth, J. Kuhl, K. Bott, A. Schulze, T. Meier, D. Bennhardt, S. W. Koch, P. Thomas, R. Hey, and K. Ploog, Evidence of biexcitonic contributions to four-wave mixing in GaAs quantum wells, Phys. Rev. B **50**, 14730 (1994).

[117] E. J. Mayer, G. O. Smith, V. Heuckeroth, J. Kuhl, K. Bott, A. Schulze, T. Meier, S. W. Koch, P. Thomas, R. Hey, and K. Ploog, Polarization dependence of beating phenomena at the energetically lowest exciton transition in GaAs quantum wells, Phys. Rev. B **51**, 10909 (1995).

[118] T. F. Albrecht, K. Bott, T. Meier, A. Schulze, M. Koch, S. T. Cundiff, J. Feldmann, W. Stolz, P. Thomas, S. W. Koch, and E. O. Göbel, Disorder mediated biexcitonic beats in semiconductor quantum wells, Phys. Rev. B **54**, 4436 (1996).

[119] W. Langbein, T. Meier, S. W. Koch, and J. M. Hvam, Spectral signatures of $\chi^{(5)}$ processes in four-wave mixing of homogeneously broadened excitons, J. Opt. Soc. Am. B **18**, 1318 (2001).

[120] C. N. Borca, T. Zhang, X. Li, and S. T. Cundiff, Optical two-dimensional Fourier transform spectroscopy of semiconductors, Chem. Phys. Lett. **416**, 311 (2005).

[121] T. Zhang, I. Kuznetsova, T. Meier, X. Li, R. P. Mirin, P. Thomas, and S. T. Cundiff, Polarization-dependent optical 2d Fourier transform spectroscopy of semiconductors, Proc. Natl. Acad. Sci. **104**, 14227 (2007).

[122] D. B. Turner and K. A. Nelson, Coherent measurements of high-order electronic correlations in quantum wells, Nature **466**, 1089 (2010).

[123] J. Reif, R. P. Schmid, and T. Schneider, Femtosecond third-harmonic generation: Self-phase matching through a transient. Kerr grating and the way to ultrafast computing, Appl. Phys. B **74**, 745 (2002).

[124] K. Dota, J. A. Dharmadhikari, D. Mathur, and A. K. Dharmadhikari, Third-order nonlinear optical response in transparent solids using ultrashort laser pulses, Appl. Phys. B **107**, 703 (2012).

[125] J. A. Dharmadhikari, K. Dota, D. Mathur, and A. K. Dharmadhikari, Spectral broadening in lithium niobate in a self-diffraction geometry using ultrashort pulses, Appl. Phys. B **122**, 140 (2016).

[126] W.-R. Hannes, A. Trautmann, M. Stein, F. Schäfer, M. Koch, and T. Meier, Strongly nonresonant four-wave mixing in semiconductors, Phys. Rev. B **101**, 075203 (2020).

[127] L. Allen and J. H. Eberly, *Optical Resonance and Two-Level Atoms* (Wiley, New York, 1975).

[128] W.-R. Hannes and T. Meier, Higher-order contributions and nonperturbative effects in the nondegenerate nonlinear optical absorption of semiconductors using a two-band model, Phys. Rev. B **99**, 125301 (2019).

[129] H. T. Duc, T. Meier, and S. W. Koch, Microscopic analysis of the coherent optical generation and the decay of charge and spin currents in semiconductor heterostructures, Phys. Rev. Lett. **95**, 086606 (2005).

[130] H. T. Duc, Q. T. Vu, T. Meier, H. Haug, and S. W. Koch, Temporal decay of coherently optically injected charge and spin currents due to carrier–lo-phonon and carrier-carrier scattering, Phys. Rev. B **74**, 165328 (2006).

[131] F. Krausz and M. Ivanov, Attosecond physics, Rev. Mod. Phys. **81**, 163 (2009).

[132] B. Shan, S. Ghimire, and Z. Chang, Effect of orbital symmetry on high-order harmonic generation from molecules, Phys. Rev. A **69**, 021404 (2004).

[133] C. Vozzi, F. Calegari, E. Benedetti, J.-P. Caumes, G. Sansone, S. Stagira, M. Nisoli, R. Torres, E. Heesel, N. Kajumba, J. P. Marangos, C. Altucci, and R. Velotta, Controlling two-center interference in molecular high harmonic generation, Phys. Rev. Lett. **95**, 153902 (2005).

[134] P. B. Corkum, Plasma perspective on strong field multiphoton ionization, Phys. Rev. Lett. **71**, 1994 (1993).

[135] J. Itatani, J. Levesque, D. Zeidler, H. Niikura, H. Pépin, J. C. Kieffer, P. B. Corkum, and D. M. Villeneuve, Tomographic imaging of molecular orbitals, Nature **432**, 867 (2004).

[136] R. Torres, N. Kajumba, J. G. Underwood, J. S. Robinson, S. Baker, J. W. G. Tisch, R. de Nalda, W. A. Bryan, R. Velotta, C. Altucci, I. C. E. Turcu, and J. P. Marangos, Probing orbital structure of polyatomic molecules by high-order harmonic generation, Phys. Rev. Lett. **98**, 203007 (2007).

[137] W. Li, X. Zhou, R. Lock, S. Patchkovskii, A. Stolow, H. C. Kapteyn, and M. M. Murnane, Time-resolved dynamics in N_2O_4 probed using high harmonic generation, Science **322**, 1207 (2008).

[138] C. Vozzi, M. Negro, F. Calegari, G. Sansone, M. Nisoli, S. De Silvestri, and S. Stagira, Generalized molecular orbital tomography, Nat. Phys. **7**, 822 (2011).

[139] D. Shafir, H. Soifer, B. D. Bruner, M. Dagan, Y. Mairesse, S. Patchkovskii, M. Y. Ivanov, O. Smirnova, and N. Dudovich, Resolving the time when an electron exits a tunnelling barrier, Nature **485**, 343 (2012).

[140] H. G. Kurz, M. Kretschmar, T. Binhammer, T. Nagy, D. Ristau, M. Lein, U. Morgner, and M. Kova, Revealing the microscopic real-space excursion of a laser-driven electron, Phys. Rev. X **6**, 031029 (2016).

[141] S. Ghimire, A. D. DiChiara, E. Sistrunk, G. Ndabashimiye, U. B. Szafruga, A. Mohammad, P. Agostini, L. F. DiMauro, and D. A. Reis, Generation and propagation of high-order harmonics in crystals, Phys. Rev. A **85**, 043836 (2012).

[142] S. Gholam-Mirzaei, J. E. Beetar, and M. Chini, High harmonic generation in ZnO with a high-power mid-IR OPA, Appl. Phys. Lett. **110**, 061101 (2017).

[143] Z. Wang, H. Park, Y. H. Lai, J. Xu, C. I. Blaga, F. Yang, P. Agostini, and L. F. DiMauro, The roles of photo-carrier doping and driving wavelength in high harmonic generation from a semiconductor, Nat. Commun. **8**, 1686 (2017).

[144] S. Jiang, S. Gholam-Mirzaei, E. Crites, J. E. Beetar, M. Singh, R. Lu, M. Chini, and C. D. Lin, Crystal symmetry and polarization of high-order harmonics in ZnO, J. Phys. B **52** (2019).

[145] O. D. Mücke, Isolated high-order harmonics pulse from two-color-driven Bloch oscillations in bulk semiconductors, Phys. Rev. B **84**, 081202 (2011).

[146] T. T. Luu and H. J. Wörner, High-order harmonic generation in solids: A unifying approach, Phys. Rev. B **94**, 115164 (2016).

[147] Y. S. You, D. A. Reis, and S. Ghimire, Anisotropic high-harmonic generation in bulk crystals, Nat. Phys. **13**, 345 (2017).

[148] Y. S. You, Y. Yin, Y. Wu, A. Chew, X. Ren, F. Zhuang, S. Gholam-Mirzaei, M. Chini, Z. Chang, and S. Ghimire, High-harmonic generation in amorphous solids, Nat. Commun. **8**, 724 (2017).

[149] F. Langer, M. Hohenleutner, U. Huttner, S. W. Koch, M. Kira, and R. Huber, Symmetry-controlled temporal structure of high-harmonic carrier fields from a bulk crystal, Nat. Photonics **11**, 227 (2017).

[150] B. Zaks, R. B. Liu, and M. S. Sherwin, Experimental observation of electron–hole recollisions, Nature **483**, 580 (2012).

[151] G. Vampa, C. R. McDonald, G. Orlando, D. D. Klug, P. B. Corkum, and T. Brabec, Theoretical analysis of high-harmonic generation in solids, Phys. Rev. Lett. **113**, 073901 (2014).

[152] G. Vampa, C. R. McDonald, G. Orlando, P. B. Corkum, and T. Brabec, Semiclassical analysis of high harmonic generation in bulk crystals, Phys. Rev. B **91**, 064302 (2015).

[153] F. Langer, M. Hohenleutner, C. P. Schmid, C. Poellmann, P. Nagler, T. Korn, C. Schüller, M. S. Sherwin, U. Huttner, J. T. Steiner, S. W. Koch, M. Kira, and R. Huber, Lightwave-driven quasiparticle collisions on a subcycle timescale, Nature **533**, 225 (2016).

[154] R. Zuo, A. Trautmann, G. Wang, W.-R. Hannes, S. Yang, X. Song, T. Meier, M. Ciappina, H. T. Duc, and W. Yang, Neighboring atom collisions in solid-state high harmonic generation, Ultrafast Science **2021**, 9861923 (2021).

[155] M. Lewenstein, P. Balcou, M. Y. Ivanov, A. L'Huillier, and P. B. Corkum, Theory of high-harmonic generation by low-frequency laser fields, Phys. Rev. A **49**, 2117 (1994).

[156] L. V. Keldysh, Ionization in the field of a strong electromagnetic wave, Sov. Phys. JETP **20**, 1307 (1965).

[157] C. R. McDonald, G. Vampa, P. B. Corkum, and T. Brabec, Interband Bloch oscillation mechanism for high-harmonic generation in semiconductor crystals, Phys. Rev. A **92**, 033845 (2015).

[158] G. Vampa and T. Brabec, Merge of high harmonic generation from gases and solids and its implications for attosecond science, J. Phys. B **50**, 083001 (2017).

[159] E. Kane, Zener tunneling in semiconductors, J. Phys. Chem. Solids **12**, 181 (1960).

[160] W. Kuehn, P. Gaal, K. Reimann, M. Woerner, T. Elsaesser, and R. Hey, Terahertz-induced interband tunneling of electrons in GaAs, Phys. Rev. B **82**, 075204 (2010).

[161] R. Zuo, X. Song, S. Ben, T. Meier, and W. Yang, Revealing the nonadiabatic tunneling dynamics in solid-state high harmonic generation, Phys. Rev. Res. **5**, L022040 (2023).

[162] X. Chai, X. Ropagnol, S. M. Raeis-Zadeh, M. Reid, S. Safavi-Naeini, and T. Ozaki, Subcycle terahertz nonlinear optics, Phys. Rev. Lett. **121**, 143901 (2018).

[163] M. T. Hassan, T. T. Luu, A. Moulet, O. Raskazovskaya, P. Zhokhov, M. Garg, N. Karpowicz, A. M. Zheltikov, V. Pervak, F. Krausz, and E. Goulielmakis, Optical attosecond pulses and tracking the nonlinear response of bound electrons, Nature **530**, 66 (2016).

[164] H. Liang, P. Krogen, Z. Wang, H. Park, T. Kroh, K. Zawilski, P. Schunemann, J. Moses, L. F. DiMauro, F. X. Kärtner, and K.-H. Hong, High-energy mid-infrared sub-cycle pulse synthesis from a parametric amplifier, Nat. Commun. **8**, 141 (2017).

[165] *Software package elk ver. 6.8.4*, `https://elk.sourceforge.io/`.

[166] L. Yue and M. B. Gaarde, Structure gauges and laser gauges for the semiconductor Bloch equations in high-order harmonic generation in solids, Phys. Rev. A **101**, 053411 (2020).

[167] D. Vanderbilt, *Berry phases in electronic structure theory: electric polarization, orbital magnetization and topological insulators* (Cambridge University Press, Cambridge, 2018).

[168] S. Jiang, H. Wei, J. Chen, C. Yu, R. Lu, and C. D. Lin, Effect of transition dipole phase on high-order-harmonic generation in solid materials, Phys. Rev. A **96**, 053850 (2017).

[169] W. C. Lang and K. Forinash, Time-frequency analysis with the continuous wavelet transform, Am. J. Phys. **66**, 794 (1998).

[170] A. J. Uzan, G. Orenstein, Á. Jiménez-Galán, C. McDonald, R. E. F. Silva, B. D. Bruner, N. D. Klimkin, V. Blanchet, T. Arusi-Parpar, M. Krüger, A. N. Rubtsov, O. Smirnova, M. Ivanov, B. Yan, T. Brabec, and N. Dudovich, Attosecond spectral singularities in solid-state high-harmonic generation, Nat. Photonics **14**, 183 (2020).

[171] S. Ghimire and D. A. Reis, High-harmonic generation from solids, Nat. Phys. **15**, 10 (2019).

[172] A. Beiser, *Concepts of modern physics*, 6th ed. (McGrawHill, New York, 2003).

[173] E. N. Osika, A. Chacón, L. Ortmann, N. Suárez, J. A. Pérez-Hernández, B. Szafran, M. F. Ciappina, F. Sols, A. S. Landsman, and M. Lewenstein, Wannier-Bloch approach to localization in high-harmonics generation in solids, Phys. Rev. X **7**, 021017 (2017).

[174] T. Meier, G. von Plessen, P. Thomas, and S. W. Koch, Coherent electric-field effects in semiconductors, Phys. Rev. Lett. **73**, 902 (1994).

[175] W. Hoyer, Quantentheorie zu Exzitonbildung und Photolumineszenz in Halbleitern, Philipps-Universität Marburg, PhD Dissertation (2002).

[176] U. Huttner, M. Kira, and S. W. Koch, Ultrahigh off-resonant field effects in semiconductors, Laser Photonics Rev. **11** (2017).

[177] A. Chernikov, T. C. Berkelbach, H. M. Hill, A. Rigosi, Y. Li, B. Aslan, D. R. Reichman, M. S. Hybertsen, and T. F. Heinz, Exciton binding energy and nonhydrogenic rydberg series in monolayer WS_2, Phys. Rev. Lett. **113**, 076802 (2014).

[178] K. He, N. Kumar, L. Zhao, Z. Wang, K. F. Mak, H. Zhao, and J. Shan, Tightly bound excitons in monolayer WSe_2, Phys Rev Lett **113**, 026803 (2014).

[179] T. Östreich, K. Schönhammer, and L. J. Sham, Exciton-exciton correlation in the nonlinear optical regime, Phys. Rev. Lett. **74**, 4698 (1995).

[180] F. Jahnke, M. Kira, S. W. Koch, G. Khitrova, E. K. Lindmark, T. R. Nelson Jr., D. V. Wick, J. D. Berger, O. Lyngnes, H. M. Gibbs, and K. Tai, Excitonic nonlinearities of semiconductor microcavities in the nonperturbative regime, Phys. Rev. Lett. **77**, 5257 (1996).

[181] C. Sieh, T. Meier, A. Knorr, F. Jahnke, P. Thomas, and S. W. Koch, Influence of carrier correlations on the excitonic optical response including disorder and microcavity effects, Eur. Phys. J. B **11**, 407 (1999).

[182] S. Weiss, M.-A. Mycek, J.-Y. Bigot, S. Schmitt-Rink, and D. S. Chemla, Collective effects in excitonic free induction decay: Do semiconductors and atoms emit coherent light in different ways?, Phys. Rev. Lett. **69**, 2685 (1992).

[183] W. Schäfer, F. Jahnke, and S. Schmitt-Rink, Many-particle effects on transient four-wave-mixing signals in semiconductors, Phys. Rev. B **47**, 1217 (1993).

[184] D. S. Kim, J. Shah, J. E. Cunningham, T. C. Damen, W. Schäfer, M. Hartmann, and S. Schmitt-Rink, Giant excitonic resonance in time-resolved four-wave mixing in quantum wells, Phys. Rev. Lett. **68**, 1006 (1992).

[185] Z. G. Soos, S. Ramasesha, D. S. Galvão, and S. Etemad, Excitation and relaxation energies of trans-stilbene: Confined singlet, triplet, and charged bipolarons, Phys. Rev. B **47**, 1742 (1993).

[186] F. Guo, M. Chandross, and S. Mazumdar, Stable biexcitons in conjugated polymers, Phys. Rev. Lett. **74**, 2086 (1995).

[187] S. Sauter-Fischer, E. Runge, and R. Zimmermann, Partial dephasing in interacting many-particle systems and current echo, Phys. Rev. B **57**, 4299 (1998).

[188] D. S. Kim, J. Shah, T. C. Damen, W. Schäfer, F. Jahnke, S. Schmitt-Rink, and K. Köhler, Unusually slow temporal evolution of femtosecond four-wave-mixing signals in intrinsic GaAs quantum wells: direct evidence for the dominance of interaction effects, Phys. Rev. Lett. **69**, 2725 (1992).

[189] H. Wang, K. B. Ferrio, D. G. Steel, P. R. Berman, Y. Z. Hu, R. Binder, and S. W. Koch, Transient four-wave-mixing line shapes: Effects of excitation-induced dephasing, Phys. Rev. A **49**, R1551 (1994).

[190] Y. Z. Hu, R. Binder, S. W. Koch, S. T. Cundiff, H. Wang, and D. G. Steel, Excitation and polarization effects in semiconductor four-wave-mixing spectroscopy, Phys. Rev. B **49**, 14382 (1994).

[191] T. Rappen, U. Peter, G. Mohs, W. Schäfer, and M. Wegener, Coherent dynamics of continuum and bound states in germanium, Semicond. Sci. Technol. **9**, 422 (1994).

[192] B. F. Feuerbacher, J. Kuhl, and K. Ploog, Biexcitonic contribution to the degenerate-four-wave-mixing signal from a GaAs/Al$_x$Ga$_{1-x}$As quantum well, Phys. Rev. B **43**, 2439 (1991).

[193] S. Bar-Ad and I. Bar-Joseph, Exciton spin dynamics in GaAs heterostructures, Phys. Rev. Lett. **68**, 349 (1992).

[194] D. J. Lovering, R. T. Phillips, G. J. Denton, and G. W. Smith, Resonant generation of biexcitons in a GaAs quantum well, Phys. Rev. Lett. **68**, 1880 (1992).

[195] J.-Y. Bigot, A. Daunois, J. Oberlé, and J.-C. Merle, Femtosecond dephasing in CdS$_x$Se$_{1-x}$ mixed crystals: The role of localized biexcitons, Phys. Rev. Lett. **71**, 1820 (1993).

[196] K.-H. Pantke, D. Oberhauser, V. G. Lyssenko, J. M. Hvam, and G. Weimann, Coherent generation and interference of excitons and biexcitons in GaAs/Al$_x$Ga$_{1-x}$As quantum wells, Phys. Rev. B **47**, 2413 (1993).

[197] D. Hulin and M. Joffre, Excitonic optical Stark redshift: The biexciton signature, Phys. Rev. Lett. **65**, 3425 (1990).

[198] G. O. Smith, E. J. Mayer, J. Kuhl, and K. H. Ploog, Pump-probe investigations of biexcitons in GaAs quantum wells, Solid State Commun. **92**, 325 (1994).

[199] G. Smith, E. Mayer, V. Heuckeroth, J. Kuhl, K. Bott, T. Meier, A. Schulze, D. Bennhardt, S. W. Koch, P. Thomas, R. Hey, and K. Ploog, Polarization selection rules for quantum beating between light- and heavy-hole excitons in GaAs quantum wells, Solid State Commun. **94**, 373 (1995).

[200] G. Bartels, V. M. Axt, K. Victor, A. Stahl, P. Leisching, and K. Köhler, $\chi^{(5)}$ Signature in the four-wave-mixing signal from a GaAs/Al$_{0.3}$Ga$_{0.7}$As superlattice, Phys. Rev. B **51**, 11217 (1995).

[201] K. Bott, E. J. Mayer, G. O. Smith, V. Heuckeroth, M. Hübner, J. Kuhl, T. Meier, A. Schulze, M. Lindberg, S. W. Koch, P. Thomas, R. Hey, and K. Ploog, Dephasing of interacting heavy-hole and light-hole excitons in GaAs quantum wells, J. Opt. Soc. Am. B **13**, 1026 (1996).

[202] W. Langbein, J. M. Hvam, M. Umlauff, H. Kalt, B. Jobst, and D. Hommel, Binding-energy distribution and dephasing of localized biexcitons, Phys. Rev. B **55**, R7383 (1997).

[203] P. Kner, S. Bar-Ad, M. V. Marquezini, D. S. Chemla, and W. Schäfer, Magnetically enhanced exciton-exciton correlations in semiconductors, Phys. Rev. Lett. **78**, 1319 (1997).

[204] M. Stein, C. Fuchs, W. Stolz, D. M. Mittleman, and M. Koch, Direct probe of room-temperature quantum-tunneling processes in type-II heterostructures using terahertz emission spectroscopy, Phys. Rev. Appl. **13**, 054073 (2020).

[205] M. Stein, C. Lammers, P.-H. Richter, C. Fuchs, W. Stolz, M. Koch, O. Vänskä, M. J. Weseloh, M. Kira, and S. W. Koch, Dynamics of charge-transfer excitons in type-II semiconductor heterostructures, Phys. Rev. B **97**, 125306 (2018).

[206] M. Fey, Kohärente Dynamik und Diffusionsprozesse von Charge-Transfer-Exzitonen, Universität Gießen, PhD Dissertation (2021).

[207] G. Fuchs, J. Hörer, A. Hangleiter, V. Härle, F. Scholz, R. W. Glew, and L. Goldstein, Intervalence band absorption in strained and unstrained InGaAs multiple quantum well structures, Appl. Phys. Lett. **60**, 231 (1992).

[208] K. J. Moore, G. Duggan, K. Woodbridge, and C. Roberts, Observations and calculations of the exciton binding energy in (In,Ga)As/GaAs strained-quantum-well heterostructures, Phys. Rev. B **41**, 1090 (1990).

[209] M. Schlierkamp, R. Wille, K. Greipel, U. Rössler, W. Schlapp, and G. Weimann, Quantum-well states under biaxial compression and tension, Phys. Rev. B **40**, 3077 (1989).

[210] J. Matthews and A. Blakeslee, Defects in epitaxial multilayers: Misfit dislocations, J. Cryst. Growth **27**, 118 (1974).

[211] C. Lammers, Über die Dynamik des Charge-Transfer-Exzitons, Philipps-Universität Marburg, PhD Dissertation (2017).

[212] F. Schäfer, A. Trautmann, C. Ngo, J. T. Steiner, M. Stein, C. Fuchs, K. Volz, F. Dobener, T. Meier, and S. Chatterjee, Optical Stark effect in type-II heterostructures, in preparation, (2023).

[213] W. Huhn and A. Stahl, Self-consistent field theory applied to the semiconductor band edge, Phys. Status Solidi B **124**, 167 (1984).

[214] V. M. Axt, K. Victor, and A. Stahl, Influence of a phonon bath on the hierarchy of electronic densities in an optically excited semiconductor, Phys. Rev. B **53**, 7244 (1996).

[215] J. E. Sipe and E. Ghahramani, Nonlinear optical response of semiconductors in the independent-particle approximation, Phys. Rev. B **48**, 11705 (1993).

[216] A. Trautmann, M. Stein, F. Schäfer, D. Anders, C. Ngo, J. T. Steiner, M. Reichelt, S. Chatterjee, and T. Meier, Analysis of the nonlinear optical response of excitons in type-I and type-II quantum wells including many-body correlations, Proc. SPIE **12419**, 124190A (2023).

[217] T. Meier, P. Thomas, and S. W. Koch, Linear and nonlinear optical properties of semiconductor nanorings with magnetic field and disorder - Influence on excitons and biexcitons, Eur. Phys. J. B **22**, 249 (2001).

[218] M. Fey, M. Stein, C. Fuchs, W. Stolz, K. Volz, and S. Chatterjee, Phase relaxation control in heterostructures featuring charge-transfer excitons, Phys. Rev. B **106**, 165303 (2022).

Danksagung

Im Rahmen meiner Arbeitsstätigkeit in der Arbeitsgruppe von Prof. Dr. Torsten hatte ich die Möglichkeit an vielen spannenden nationalen sowie internationalen Forschungssprojekten teilzunehmen. Durch die Teilnahme an Physikkonferenzen sowie diversen Workshops konnte ich in Austausch mit interessanten Forschern treten sowie neue Orte entdecken. Dabei bin ich nun schon insgesamt seit mehr als 8 Jahren Teil dieser Arbeitsgruppe und habe meine Abschlussarbeiten allesamt in diesem Lehrstuhl angefertigt. Seither stand Prof. Dr. Torsten Meier mir immer als Ansprechpartner zur Verfügung und unterstützte mich bei der Bearbeitung diverser physikalischer Problemstellungen. Trotz der Umstellung auf Home-Office bedingt durch die Corona Pandemie wurde stets ein ausgiebiger Austausch von ihm gewährleistet und ermöglicht. Insbesondere die Möglichkeit zur Anfertigung dieser Forschungsarbeit im Rahmen meiner Doktorandenstelle sowie dem Vertrauen und der mehrjährigen Unterstützung möchte ich mich an dieser Stelle ganz herzlich bedanken.

Zu Beginn meiner Tätigkeit als Doktorand wurde ich außerdem von Dr. Wolf-Rüdiger Hannes betreut. Mit ihm konnte ich mich stets austauschen, wenn es Unklarheiten beim Verständnis aber auch der Programmierung komplizierter physikalischer Problemstellungen ging. Auch ihm gilt mein Dank für diese Unterstützung. Des Weiteren bedanke ich mich bei Ruixin Zuo für die gemeinsamen Kooperationsprojekte. Außerdem bedanke ich bei meinen langjährigen Mitarbeiter Dr. Hendrik Rose und Dr. Matthias Reichelt, die mit ihren Ideen und Ratschlägen meine Forschungsarbeiten bereichert haben.

Zum Schluss bedanke ich mich bei meinen Eltern, die mich fortwährend motiviert und stets Zuspruch gegeben haben.